# Adaptation of the South-Eastern drainage system under a changing climate

## Seawater intrusion risk

Amin Gholami, Adrian Werner, Cristina Solórzano-Rivas, Amir Jazayeri,
Eshan Kamali Maskooni and Hongxiang Fan

Goyder Institute for Water Research
Technical Report Series No. 25/5.3

www.goyderinstitute.org

**Goyder Institute for Water Research Technical Report Series ISSN: 1839-2725**

The Goyder Institute for Water Research is a research alliance between the South Australian Government through the Department for Environment and Water, CSIRO, Flinders University, the University of Adelaide and the University of South Australia. The Institute facilitates governments, industries, and leading researchers to collaboratively identify, develop and adopt innovative solutions for complex water management challenges to ensure a sustainable future.

This *Adaptation of the South-Eastern drainage system under a changing climate* project has been jointly funded by the Australian Government through the National Water Grid Fund, the Limestone Coast Landscape Board, and the South Australian Government. The project was delivered by the Goyder Institute for Water Research partners: CSIRO, the University of South Australia, Flinders University and the University of Adelaide in collaboration with the Limestone Coast Landscape Board, South Eastern Water Conservation and Drainage Board (SEWCD Board) and the Department for Environment and Water. This report was prepared by Amin Gholami, Adrian Werner, Cristina Solórzano-Rivas, Amir Jazayeri, Ehsan Kamali Maskooni and Hongxiang Fan.

Enquires should be addressed to: Goyder Institute for Water Research
The University of Adelaide (Manager)
209A, Level 2 Darling Building, North Terrace,
Adelaide, SA 5000
tel: (08) 8313 5020
e-mail: enquiries@goyderinstitute.org

**Citation**

Gholami A, Werner AD, Solórzano-Rivas C, Jazayeri A, Maskooni EK, and Fan H (2025) *Adaptation of the South-Eastern drainage system under a changing climate. Seawater intrusion risk.* Goyder Institute for Water Research Technical Report Series No. 25/5.3

© Crown in right of the State of South Australia, Department for Environment and Water, CSIRO, Flinders University, the University of Adelaide, and the University of South Australia.

**Disclaimer**

This report has been prepared by Flinders University and the Lower Limestone Coast Landscape Board and reviewed in accordance with the publication protocols of the Goyder Institute for Water Research. The report contains independent scientific/technical advice to inform government decision-making. The independent findings and recommendations of this report are subject to separate and further consideration and decision-making processes and do not necessarily represent the views of the Australian Government, South Australian Department for Environment and Water or the Limestone Coast Landscape Board. The Goyder Institute and its partner organisations do not warrant or make any representation regarding the use, or results of the use, of the information contained herein about its correctness, accuracy, reliability, currency or otherwise and expressly disclaim all liability or responsibility to any person using the information or advice. Information contained in this document is, to the knowledge of the project partners, correct at the time of writing.

# Contents

# Figures

# Tables

# First Nations Respect and Reconciliation

The Goyder Institute for Water Research and Limestone Coast Landscape Board, acknowledges the Traditional Custodians of the lands and waters of the Limestone Coast and South East region, where this project took place. Together we pay our respects to their Elders—past, present, and emerging—and recognise Aboriginal people as the First Peoples and Nations of South Australia, possessing and caring for these lands under their own laws and customs.

We respect the enduring cultural, spiritual, physical, and emotional connections that Aboriginal peoples maintain with their lands and waters. We recognise the diverse rights, interests, and obligations of First Nations and the deep cultural connections that exist between different First Nations communities. We seek to support their meaningful engagement and honour the continuation of their cultural heritage, economies, languages, and laws, which remain of ongoing importance.

We walk together with the First Nations of the South East and the Ngarrindjeri peoples through organisations such as Burrandies Aboriginal Corporation, Ngarrindjeri Aboriginal Corporation, the Ngarrindjeri Lands & Progress Aboriginal Corporation and South East Aboriginal Focus Group. For the work of generations past, and the benefit of generations future, we seek to be a voice for reconciliation in all that we do.

# Project Summary

The Limestone Coast of South Australia is a highly modified landscape with an extensive cross-catchment drainage system converting what was once a wetland dominated landscape into one dominated by agricultural production. The region now has a diverse agricultural sector and extensive forestry plantations which are highly dependent on reliable rainfall and easy access to the region’s substantial groundwater resources. However, as climatic conditions become hotter and drier it’s important to understand impacts on ground and surface water resources and consequent risks to primary production and the environment to build a water secure future.

Achieving water security in the Limestone Coast region under a changing climate requires a more integrated and holistic approach to water resource management. In particular, the interactions between surface water and groundwater must be better understood, quantified, and managed to balance the seasonal demands—removing excess water from productive lands during winter while safeguarding groundwater-dependent agriculture and ecosystems during summer.

The “*Adaptation of the South-Eastern drainage system under a changing climate*” project aims to inform opportunities to improve water management in the region - including potential use of water in the drainage network - to address risks to primary industries and groundwater dependent ecosystems. Delivered through the Goyder Institute for Water Research, research teams from the CSIRO, Flinders University and the University of South Australia have completed five separate but inter-connected tasks:

1. Quantifying the value of consumptive and non-consumptive uses of water

   This task assessed the value of additional water for key primary industries in the region, while also estimating the value of water for non-consumptive uses aimed at achieving ecological outcomes. Together, these valuations provide important context to the project’s hydrological tasks, informing options to manage additional available water in the region.

2. Current and future water availability

   A water balance model for the region has been developed using the Bureau of Meteorology’s Australian Water Resources Assessment – Landscape (AWRA-L) model. It integrates national and regional datasets to capture surface runoff, recharge, and soil moisture, while accounting for seasonal dynamics and regional variability. The model enables analysis of climate change impacts on the full water balance, providing insight into future water availability, supporting both short- and long-term water management decisions.

3. Groundwater and wetland modelling

   Site-specific models representing three-dimensional aquifer-wetland interactions have been developed for two key groundwater dependent sites. The models test the feasibility of changing the water distribution in the local landscape to improve ecosystem health and mitigate impacts of groundwater extraction. Options included redirecting / holding water back in drains, altering surface water inflows and reducing the extent of the wetland basin with levees. The learnings from modelling these two disparate sites will assist decisions to manage additional available water in the region.

4. Seawater intrusion risk

   The coastal area south of Mount Gambier is an area of high value irrigated agriculture and significant karst springs where the risk of seawater intrusion is of concern for both irrigators and environmental assets. This task set out to understand the extent and hydrodynamics of seawater intrusion in the region with an airborne electromagnetic survey of the south coast area, undertaken in October 2022, and construction of cross-sectional models to simulate seawater intrusion under different scenarios at different regional locations. This work provides the evidential basis to build on previous projects where reinstating wetlands by retaining water in drains appeared to effect some control over the seawater interface.

5. Groundwater, Ecology, Surface water and Wetland Assessment Tool (GESWAT)

To enable opportunities to improve water management to be easily identified and investigated - including the potential use of water in the drainage network –a dynamic GIS tool (GESWAT) was built. GESWAT brings together outputs from the other project tasks integrating them in a tool with a range of other critical data (e.g. surface water flows, groundwater levels, and rainfall data, annual water use and allocation data, ecological information and other standard datasets). GESWAT provides the LC Landscape Board and its partner agencies a single platform with which to view, compare and interrogate the diversity of hydrological and ecological information available to inform policy and management decisions.

This report details results from Task 4 of the project.

Further results from this project are presented in the following reports:

Task 1

Cooper B, Crase L, Kandulu J, and Subroy V. (2025) *Adaptation of the South-Eastern drainage system under a changing climate - Quantifying the value of different water uses and future demands*. Goyder Institute for Water Research Technical Report Series No. 25/2.

Task 2

Gibbs MS, Montazeri M, Wang B, Crosbie R, and Yang A. (2025) *Adaptation of the South-Eastern drainage system under a changing climate - Water Availability for South East Drainage Adaptation*. Goyder Institute for Water Research Technical Report Series No. 25/3.

Task 3

Gholami A, Werner AD, Maskooni EK, Fan H, Jazayeri A, and Solórzano-Rivas C. (2025) *Adaptation of the South-Eastern drainage system under a changing climate - Groundwater and wetland modelling*. Goyder Institute for Water Research Technical Report Series No. 25/4.

Task 4

Davis A, Munday TJ, and Ibrahimi T. (2025) *Adaptation of the South-Eastern drainage system under a changing climate - Limestone Coast Airborne Electromagnetic Survey: Acquisition, Processing and Modelling*. Goyder Institute for Water Research Technical Report Series No. 25/5.1.

Davis A, Munday TJ, and Ibrahimi T. (2025) *Adaptation of the South-Eastern drainage system under a changing climate - Limestone Coast Airborne Electromagnetic Survey: Conductivity-Depth Sections*. Goyder Institute for Water Research Technical Report Series No. 25/5.2.

Gholami A, Werner AD, Solórzano-Rivas C, Jazayeri A, Maskooni EK, and Fan H. (2025) *Adaptation of the South-Eastern drainage system under a changing climate - Seawater intrusion risk.* Goyder Institute for Water Research Technical Report Series No. 25/5.3.

Task 5

Gonzalez D, Werner AD, Jazayeri A, Pritchard J, Fan H, Botting S, and Judd R. (2025) *Adaptation of the South-Eastern drainage system under a changing climate - Groundwater, Ecology, Surface water and Wetland Assessment Tool (GESWAT) Spatial Data Dictionary*. Goyder Institute for Water Research Technical Report Series No. 25/6.

# Executive Summary

This report describes the key findings and methodologies of seawater intrusion modelling undertaken as part of Task 4 (*Seawater intrusion risk*) of the Goyder project *Adaptation of the South-Eastern drainage system under a changing climat*e. The primary goals of this investigation are to: (a) apply numerical modelling to evaluate the extent of seawater in the coastal aquifers of the Limestone Coast, and (b) assess the threat of seawater intrusion under current and future groundwater stresses.

Five cross-sectional (2D) models of Limestone Coast aquifers were extracted from an existing regional-scale groundwater flow model (3D) of the Lower Limestone Coast Prescribed Wells Area that was developed in 2015 through a previous Goyder Institute collaborative project. Groundwater heads and flows from 2D models were compared with those of the *parent* 3D model. Reasonable matches were obtained, validating the method for 2D model extraction.

Modifications were needed to allow for the simulation of density-dependent groundwater flow and dispersive salt transport, which are key factors controlling the seawater extent in coastal aquifers. Mainly for this reason, the models described in this study are significantly more complex than “standard” groundwater models that are not required to distinguish waters of different densities. This includes the need to run models for considerable timescales to find stable (steady state) conditions.

The models were extended offshore because the aquifers of the Limestone Coast are known to occur within the continental shelf of the Great Australian Bight, and earlier studies have indicated that fresh groundwater may extend beneath the sea within the study area. Offshore extrapolation was achieved by incorporating data from petroleum wells to approximate offshore sediment distributions. Next, the 3-layer structure of the regional 3D model was subdivided into up to 23 layers (the number of layers varied between the cross sections) to allow for the simulation of vertical variations in flow and salinity in 2D models. Also, the horizontal dimension of cells was reduced to up to ~25% of their original size in areas likely to host the freshwater-seawater interface. This refinement was undertaken to improve the horizontal resolution of the seawater wedge, in particular the complex zone of mixing between freshwater and seawater. Subsequently, density-dependent solute transport parameters were added to the model, including porosity, solute dispersion parameters and the relationship between salt concentration and water density. After some model testing, 2D models were truncated in their horizontal extents to reduce the number of cells and to lower the time required to complete simulations. The landward truncation of 2D models ensured that the seawater wedge did not reach the landward boundary, and offshore freshwater did not reach the seaward limit of the model.

The first simulations of seawater intrusion adopted the conditions occurring around 1970 as input parameters. The models were then run for durations sufficient to reach steady-state conditions, which required some 30,000 years. The goal was to create initial conditions, in terms of the seawater distribution in the aquifer, for transient simulations. We refer to these models as "pre-development" scenarios, notwithstanding that the conditions in 1970 reflect a modified situation since European settlement. The results of pre-development simulations were treated as baseline conditions for the seawater extent, allowing us to quantify any landward movements of seawater (i.e., seawater intrusion) in Limestone Coast aquifers that occurred in transient simulations. Transient simulations adopted the period 1970–2013 (44 years; between January 1970 and December 2013), consistent with that of the regional 3D model. A third modelling scenario was also generated, whereby steady-state conditions were obtained that used average recharge and evapotranspiration for the 10-year period 2004–2013, while pumping was set as a constant value taken from the average of the last year (2013) of the transient model. This scenario was intended to evaluate the long-term seawater extent in Limestone Coast aquifers, at least under conditions that are similar to the latter stages of the 3D model simulation period. In this way, the model provided insight into the stability of the seawater wedge, specifically, whether to expect the wedge to continue to move inland or whether the seawater wedge has reached a stable condition (as of 2013), and to approximate the eventual landward position of the wedge for periods exceeding the 44-year timeframe of transient simulations. Moreover, three additional scenarios were conducted based on the third scenario: (a) a sea-level rise of 0.3 m; (b) an 18%

reduction in recharge to approximate the projected rainfall decline due to climate change by 2050; and (c) a 71% increase in pumping to represent full allocation levels anticipated by 2050.

The above methodology was undertaken at five cross-sectional locations that intersect the following geographical features: (a) MacDonnell Bay, (b) South of Lake Bonney, (c) Canunda National Park, (d) Cape Jaffa, and (e) Paranki Lagoon Conservation Park.

The results of cross section A (MacDonnell Bay) show the occurrence of seawater within the inland part of both the upper and lower aquifers, with a substantial occurrence of offshore fresh groundwater in the lower aquifer, in which the simulated interface tip extends approximately 12 km offshore. Freshwater discharge from the lower aquifer into the upper aquifer is also apparent, causing freshwater-seawater mixing in the offshore part of the upper aquifer. The results indicate minimal seawater intrusion (i.e., a landward movement of the freshwater-seawater interface toe of ~15 m) in the lower aquifer between 1970 and 2013. The stability of the seawater wedge in the deeper aquifer can be attributed to the low value of hydraulic conductivity in this layer (3 m/d). In contrast, the upper aquifer shows significant seawater intrusion during the same period, with the seawater toe advancing ~855 m further inland, reaching 4,036 m inland by 2013. This is the consequence of a head drop of approximately 1 m (at ~5 km inland) in the upper aquifer during the 44-year simulation period and the high hydraulic conductivity of this layer (115 m/d). A sea-level rise scenario that examined the new steady-state position of the seawater wedge at cross section A, with the sea level 300 mm higher, showed only moderate influence on the seawater extent in the upper aquifer, resulting in an inland toe shift of about 86 m. However, the lower aquifer appears more vulnerable to seawater intrusion under sea-level rise, with the seawater wedge toe predicted to advance some 535 m further inland, albeit this required considerable time (>100 years) for this movement to occur.

A 71% increase in pumping was assessed through an additional scenario, also run until steady-state conditions were obtained. The pumping increase caused seawater intrusion at cross-section A in the form of a 460 m landward shift in the toe in the upper aquifer, and a 1,312 m landward movement of the toe in the lower aquifer. A reduction of 18% in the recharge had the most pronounced effect (relative to sea-level rise and pumping impacts) on simulated seawater intrusion in both aquifers. It caused an inland toe shift of 752 m in the upper aquifer and a 3,591 m shift in the toe within the lower aquifer. Note that the time scales for these shifts to occur were not explored in detail because only steady-state-to-steady-state conditions were simulated. That is, the seawater intrusion described here may not eventuate within planning timeframes. Nevertheless, seawater intrusion obtained in these scenarios are an indication that seawater is likely moving landward and will shift significant distances further inland under plausible future scenarios, at least under the simulated stresses, even if the shifts in the toe described above may take centuries to achieve.

The results of cross section B (south of Lake Bonney) also indicate that fresh groundwater extends offshore within the lower aquifer, with its tip reaching over 24 km from the shoreline, thereby excluding seawater from crossing the shoreline in the lower aquifer. The seawater wedge occurs landward of the coast within the upper aquifer. Fresh groundwater leakage from the lower aquifer into the upper aquifer (through the intervening aquitard) was observed as patches of lower-salinity water, driven by complex density-dependent processes, within the offshore part of the upper aquifer. Seawater intrusion over the 44-year simulation occurred as a ~1 km advance in the toe of the wedge in the upper aquifer, whereas the seawater toe moved landward only 13 m in the lower aquifer. Sea-level rise seems to pose only a minor risk of seawater intrusion, with the toe expected to shift 164 m inland in the upper aquifer and 469 m landward in the lower aquifer (where it is predicted to be offshore at cross section B). A 71% increase in pumping caused greater seawater intrusion than that caused by sea-level rise, with the toe shifting inland by 472 m in the upper aquifer, and 911 m landward in the offshore, lower aquifer. Reduced recharge (by 18%) again seems to pose the greatest threat to freshwater in the nearshore aquifers of the Limestone Coast, with toe shifts of 1,096 m (inland) and 1,899 m (landward) in the upper and lower aquifers, respectively. Note that these toe movements are from one steady-state condition to another, and are likely to overestimate any seawater intrusion occurring over timeframes of <100 years.

Seawater penetrates onshore in both the upper and lower aquifers of cross section C (Canunda National Park). Fresh groundwater discharge seeps through the aquitard, from the lower aquifer to the upper aquifer, close to the shoreline. Minimal seawater intrusion (12 m toe shift) occurred in the lower aquifer between 1970 and 2013 due to relatively consistent hydraulic heads during the simulation period and the low value of the hydraulic conductivity of this layer (3 m/d). No offshore fresh groundwater is observed at this location in either aquifer as a result of lower heads in the vicinity of cross section C relative to the head imposed by the sea. The latter is particularly high because the aquifer is deep (enhancing seawater density effects); particularly the lower aquifer, which has a bottom elevation of ~-750 m AHD. Seawater intrusion in the upper aquifer occurred, with the toe advancing 333 m further inland during the transient simulation. Sea-level rise had little impact on the seawater extent in the lower aquifer, with the toe shifting inland by 52 m. The upper aquifer was affected more so, although to a relatively minor degree, with the toe advancing 124 m further inland. The 71% increase in pumping caused seawater intrusion (toe movements) of 74 m in the upper aquifer and 240 m in the lower aquifer. The 18% reduction in recharge caused greater inland toe shifts - 190 m in the upper aquifer and 371 m in the lower aquifer. Thus, the recharge reduction again had the greatest impact in terms of seawater intrusion.

As with cross section C, cross section D (Cape Jaffa) produced seawater wedges with onshore toes in both the upper and lower aquifers. The extent of seawater was larger in the lower aquifer. Again, no offshore fresh groundwater occurred in the model of this location, likely due to the relatively low hydraulic heads (at about 6 km inland from the coast, the head is ~4 m AHD in the lower aquifer in 2013), in contrast to cross sections A and B where the heads are higher near the coast. A comparison of pre-development and 2013 conditions reveals a stable seawater wedge in the lower aquifer, with negligible movement of the seawater toe during 1970–2013. Conversely, the toe location in the upper aquifer shifted 206 m further inland relative to its pre-development position during the 44-year transient simulation. Predictive scenarios indicate that sea-level rise is likely to cause seawater to move 391 m and 390 m inland in the upper and lower aquifers, respectively (again, this shift represents the difference between two steady-state conditions). The 71% increase in pumping produced seawater extents that were 122 m and 133 m further inland in the upper and lower aquifers, respectively. The 18% reduction in recharge produced inland movements in the toe of 362 m and 296 m in the upper and lower aquifers, respectively. Thus, at cross section D, sea-level rise is expected to cause the most extensive seawater intrusion.

Seawater penetrates only a small distance inland (124 m) from the coast in the upper aquifer of cross section E (Paranki Lagoon Conservation Park) under pre-development conditions, according to the model. Groundwater discharge to the sea pushes the freshwater-seawater interface ~7 km offshore in the lower aquifer. This arises from high groundwater heads in the vicinity of cross section E, with groundwater levels some 8 m AHD at 5 km from the coast. The seawater extent was stable during the 44-year transient simulation, with toe movements of 1 m and 11 m in the upper and lower aquifers, respectively. The corresponding toe movements due to sea-level rise of 300 mm were 5 m and 260 m (respectively), while a drop in recharge of 18% caused 4 m and 197 m (respectively) of seawater intrusion, and a change in pumping of 71% led to inland toe movements of 1 m and 16 m, respectively. Thus, cross section E appears to be under reduced threat of seawater intrusion relative to other sites.

A comparison of modelling results with recent interpretations of an airborne electromagnetic (AEM) survey, conducted by CSIRO as part of the Task 4 program, was performed for cross sections A and B, where AEM data are available. This comparison demonstrated a reasonable correlation between numerical modelling and AEM results in the upper aquifer, in terms of the occurrence of the seawater wedge. This is notwithstanding that the AEM may pick up high-conductivity features that are not related to the seawater wedge, and rather, reflect geological variability, non-marine saline groundwater, and artefacts associated with interference from surface infrastructure. Also, the penetration depth of the AEM survey restricts the interpretation of seawater occurrence in the lower aquifer.

# Acknowledgments

This report covers one of five tasks undertaken as part of the "*Adaptation of the South-Eastern drainage system under a changing climate"* project. The project has been jointly funded by the Australian Government through the National Water Grid Fund, the Limestone Coast Landscape Board, and the South Australian Government. The project was delivered by the Goyder Institute for Water Research partners: CSIRO, the University of South Australia, Flinders University and the University of Adelaide in collaboration with the Limestone Coast Landscape Board, South Eastern Water Conservation and Drainage Board (SEWCD Board) and the Department for Environment and Water.

The authors wish to express their gratitude to several individuals whose contributions have been invaluable to this project. Special thanks are extended to Sue Botting and Ryan Judd from the Limestone Coast Landscape Board for their support of this research through the provision of advice on model sites and scenarios, and feedback on report writing. We are thankful to Tim Munday, Aaron Davis, Kevin Cahill, and Tania Ibrahimi from CSIRO for the provision of AEM cross-sections and helpful discussions about the hydrogeology of the study area. We are also grateful for the project management assistance provided by Fiona Adamson.

# 1 Introduction

## 1.1 Background

Given the limited surface water resources of the Limestone Coast of South Australia, groundwater is the dominant source of freshwater (Mustafa et al., 2012). The groundwater resources of the Limestone Coast are mostly of high quality and support a wide range of primary industries, including viticulture, livestock, forestry, horticulture and seed cultivation (Gibbs et al., 2012). Groundwater is also the primary water source for town water supply and rural domestic use in the Limestone Coast (Brookes, 2010; Gibbs et al., 2012).

Coastal aquifers in the Limestone Coast are at threat of seawater intrusion (SWI), which is the landward movement of seawater in coastal aquifers caused by the lowering of groundwater levels, sea-level rise or various other causes (Werner et al., 2013). Substantial groundwater extraction occurs within the region’s coastal aquifers, which support sensitive freshwater ecosystems that may be impacted by salinity changes arising from SWI. Pumping occurs primarily from the upper aquifer, the Tertiary Limestone Aquifer (TLA). Leakage between the TLA and the underlying aquifer, the Tertiary Confined Sand Aquifer (TCSA), is known to occur in several locations within the study area (Morgan et al., 2015).

There is presently only limited understanding of the spatial extent of seawater within Limestone Coast aquifers, despite previous attempts to measure and model salinity variations within the coastal fringe of the Limestone Coast. Previous studies of SWI within the Limestone Coast include the geophysical investigation of King and Dodds (2002), who used transient electromagnetics (TEM) to try to characterize the seawater wedge along five 5 km-long transects perpendicular to the coastline. While the TEM results did not conclusively identify the freshwater-seawater boundary, they highlighted zones of high conductivity that may indicate saline groundwater. King and Dodds (2002) recommended drilling wells to validate the TEM findings, which would support further field surveys such as airborne electromagnetics (AEM) to comprehensively map the interface along the coast. Mustafa et al. (2012) developed a three-dimensional (3D) hydrostratigraphic model to assess the risk of SWI in the area. They also analysed the hydrochemistry of coastal groundwater, detecting the occurrence of seawater up to ~1.5 km inland. However, whether seawater intrusion was occurring was difficult to ascertain due to limited historical data. Nevertheless, they concluded that SWI had occurred at Eight Mile Creek, based on increasing groundwater salinity observed over time at two observation wells—one at a depth of 12 m and the other at 180 m—located 1 km inland from the coast. Consequently, they recommended ongoing monitoring to determine whether SWI would continue to occur in that location or in other areas where the presence of seawater was detected.

Recently, DEW (2023) constructed a 3D numerical groundwater flow model for the TLA within the Lower Limestone Coast Prescribed Wells Area. The study considered two modelling scenarios, assuming different extraction rates and climate conditions, with projections from 2022 to 2050. One scenario extended the conditions observed between 2012 and 2021, while the other assumed increased extraction and decreased recharge over the projected period in response to climate change. The model incorporated the influence of the freshwater-seawater interface using the simplified approach provided by the MODFLOW Seawater Intrusion Package, SWI2 (Bakker et al., 2013). SWI2 neglects vertical flow effects and assumes a sharp interface between freshwater and seawater by neglecting dispersion effects. For that reason, the authors (DEW, 2023) noted limitations in ascertaining both the SWI extent and interface location, recommending further validation with AEM results. Thus, the AEM survey of the current study (Davis et al., 2025a, 2025b) is a direct response to those recommendations. We anticipate that the simulation of SWI in the Limestone Coast incorporating dispersive transport, as undertaken in the current study, will overcome some of the limitations of the SWI2 approach used by DEW (2023), notwithstanding that the current study adopts 2D cross sections while DEW (2023) undertook a regional assessment.

Despite these earlier studies, several key management questions remain unanswered regarding the proximity of the seawater interface to critical water infrastructure and the potential for the interface to shift landward under existing groundwater levels. Additionally, the potential for SWI to occur under future conditions, including with sea-level rise and changes to recharge resulting from climate change, require further investigation.

## 1.2 Aims

The primary objective of the investigation described in this report is to develop an understanding of the risk that SWI poses to irrigated agriculture and coastal aquifers more generally in the Limestone Coast, at least at a selection of key locations. The project aims to achieve this by defining the spatial extent and movements in the seawater interface using numerical simulation. A key goal in the development of these modelling tools is the creation of a methodology for extracting SWI models from existing regional groundwater flow models, so that in the future, SWI can be assessed at a larger number of locations within the study area. For example, if the regional groundwater models are updated, the methodology developed in this study can be re-run to build a new set of cross-sectional models with far less effort than was expended in the current study.

The current modelling analysis is complementary to a concurrent airborne electromagnetic (AEM) survey, which will map the variability of the seawater extent within the south coast of the Limestone Coast. The comparison of modelling results with AEM interpretations is a significant step forward in seawater intrusion analysis in Australia that will allow the resulting models to assess the threat posed by future SWI with greater reliability. The AEM-numerical model comparison in the current study is largely qualitative and based on a snapshot in time, and as such, there are opportunities to draw further conclusions about seawater intrusion in the Limestone Coast from a more systematic comparison of the AEM results, likely requiring a wider array of numerical simulations.

Much of the advice created from this investigation is drawn from scenarios of SWI under modified hydrogeological conditions, which include relatively simplified cases of sea-level rise, pumping and recharge changes, including in response to climate change. Additional scenarios are possible to examine a wider range of situations and “what-if” questions of relevance to water management and ecosystem protection in the study area through a continuation of the current modelling investigation.

By addressing these objectives, the project aims to inform water management strategies that mitigate the risk of SWI, ensuring the long-term sustainability of coastal groundwater resources for both agricultural use and ecosystem support in the region.

# 2 Methods

## 2.1 Outline of modelling approach

This section outlines the strategy to construct and run numerical models of the seawater extent and SWI in the Limestone Coast. Table 1 describes the key steps.

**Table 1.** Overview of modelling methodology for building 2D cross-sectional SWI models.

| Step | Description |
|---|---|
| 1 | Obtain existing regional-scale groundwater flow models of the study area. Validate model input files by re-running relevant models and comparing results to those provided in accompanying reports. |
| 2 | Convert the regional-scale model input files into Python scripts (developed and executed using Python version 3.11.5). |
| 3 | Extract relevant 2D models (cross-sectional flow models) from the regional model using Python, apply an initial truncation to the landward extent to focus on the coastal zone, and extrapolate offshore. |
| 4 | Run 2D flow models in steady and transient states and compare results to the regional model. |
| 5 | Reduce the cells sizes of 2D flow models and compare results to the regional model. |
| 6 | Add solute transport and density effects using the basic transport, advection, dispersion, generalized conjugate gradient, source and sink mixing, and variable-density flow packages, and run steady-state SWI simulations. |
| 7 | Truncate models to capture onshore seawater and offshore freshwater extents, re-run models and compare to the models obtained in Step 6. |
| 8 | Run transient SWI simulations. |
| 9 | Check the results of 2D SWI models against AEM data for cross sections A and B, as well as available salinity data from coastal wells across all cross sections. |
| 10 | Run modified SWI models to assess causes of any differences between AEM results and 2D models. |
| 11 | Run SWI scenarios, including long-term steady-state, modified recharge and pumping, and sea-level rise. |
| 12 | Make interpretations, draw conclusions and complete reporting. |

## 2.2 Review of Lower Limestone Coast regional model

The current study adopts the regional-scale 3D groundwater flow model of the Lower Limestone Coast Prescribed Wells Area developed by Morgan et al. (2015), in creating 2D cross-sectional models. The model is discretized into 1 km x 1 km cells. It consists of three layers: the TLA (Tertiary Limestone Aquifer; layer 1), a Lower Tertiary Aquitard (layer 2), and the TCSA (Tertiary Confined Sand Aquifer; layer 3). Figure 1 depicts the study area and the location of modelling cross sections, while Figure 2 shows the regional model of Morgan et al. (2015). This model was imported into Python to facilitate execution using publicly available versions of MODFLOW 2005. It was then re-run to obtain model outputs relevant to the investigation of coastal aquifer hydrology in the study area. Outputs obtained from re-running the model were consistent with those shown in the accompanying report (Morgan et al., 2015).

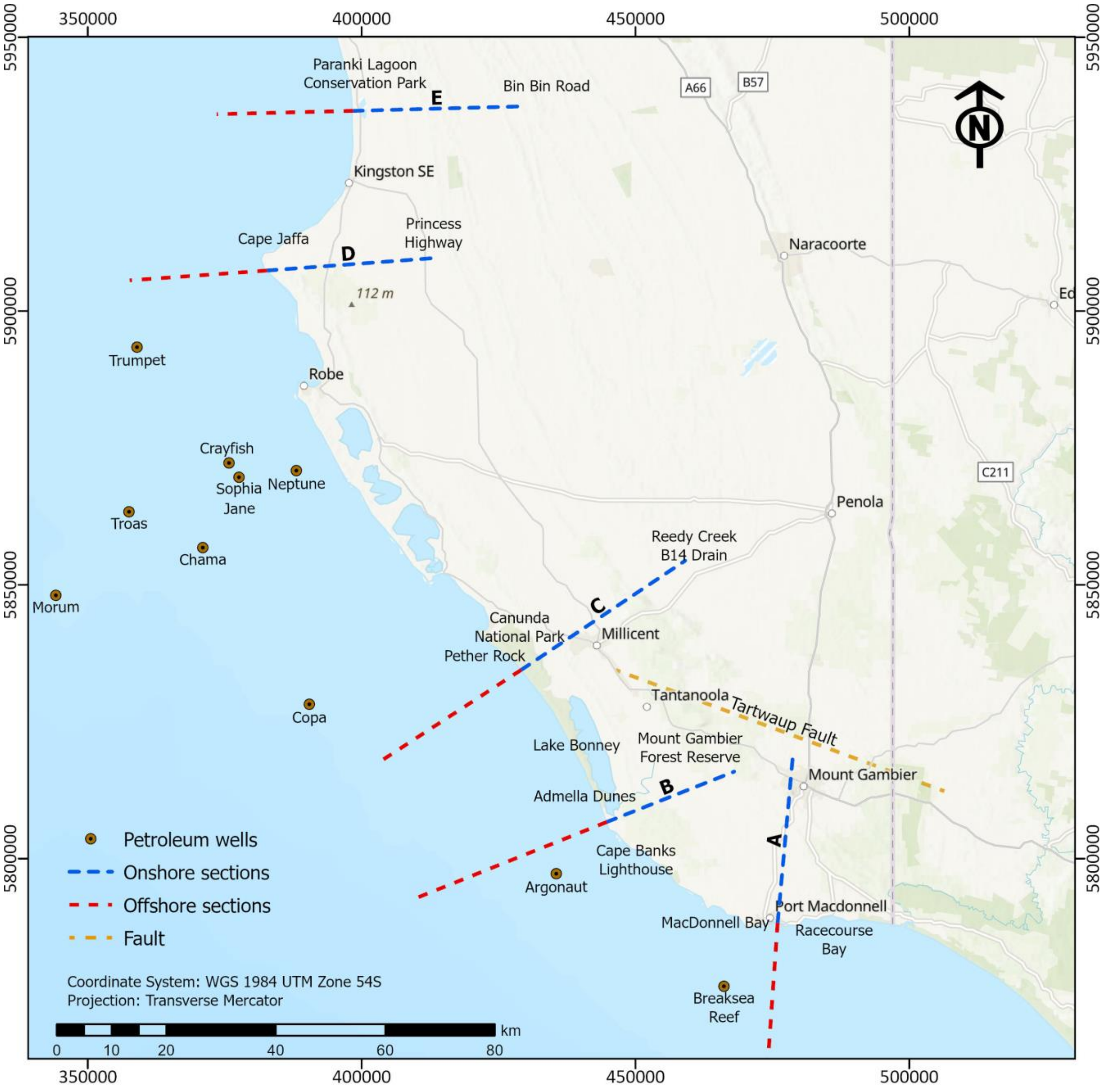

**Figure 1.** Study area showing the locations of the cross-sectional models.

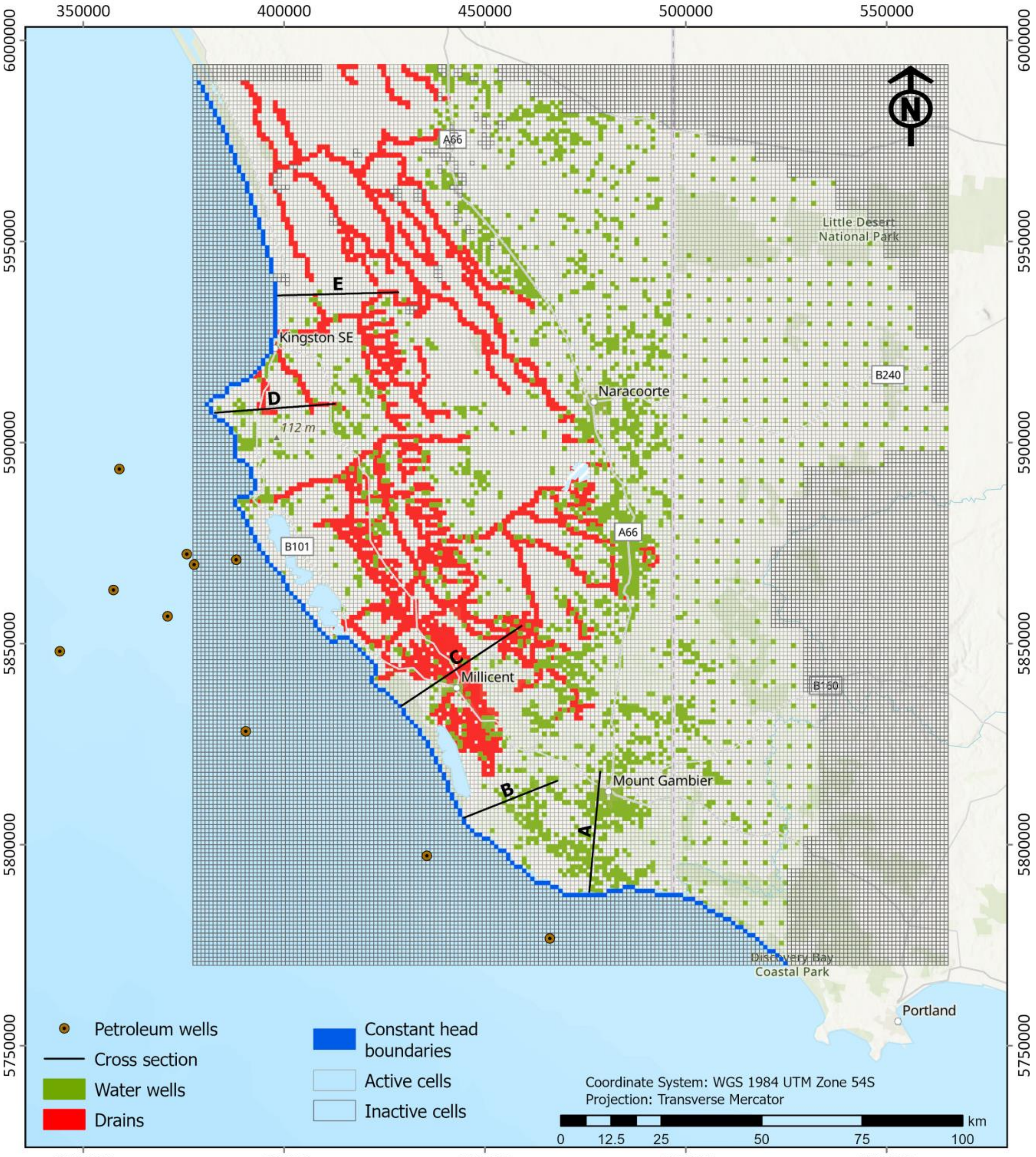

**Figure 2.** Regional model of the Lower Southeast of South Australia (Morgan et al., 2015), showing seawater intrusion model cross sections (the onshore parts that are based on the regional model are shown; offshore extensions are illustrated in Figure 1), drains, pumping wells and offshore oil exploration (petroleum) wells.

## 2.3 Extract cross sections from the regional-scale model

To assess the risks of SWI, five representative locations along the coastal fringe of the study area were selected. Cross-sectional models were extracted from the regional-scale model at these locations, initially as groundwater flow models and later converted to SWI models. The methodology for extracting the cross section from the 3D regional model is provided in Appendix A. Cross-sectional models were extended offshore using geological information from petroleum wells in the offshore areas, adopting a similar methodology to that described by Knight et al. (2019) and explained in more detail in Section 2.4. Figure 1 shows both the onshore and offshore extents of models, and labels the petroleum wells for reference within the text that follows, while Figure 2 shows the onshore locations of these models.

Cross section A (CSA) intercepts MacDonnell Bay between the Harbor of Port MacDonnell and Racecourse Bay, and extends landward near the city of Mount Gambier. CSA intercepts a high density of pumping wells, as shown in Figure 2. The regional model of Morgan et al. (2015) does not simulate drains in the vicinity of CSA (Figure 2), although there is nevertheless likely to be surface water-groundwater interactions in this region. The landward limit of CSA is the Tartwaup Fault, across which groundwater levels change abruptly. Initial attempts at cross-sectional models that pass through the fault demonstrated that it is very difficult to reproduce the hydrogeology of this fault in a cross-sectional model due to the strong lateral flows (parallel to the fault) that occur. CSA extends seaward close to the Breaksea Reef offshore petroleum well, and therefore, its offshore stratigraphy will reflect mostly that well, although the offshore stratigraphy was created based on all of the offshore wells plus the onshore stratigraphy from the regional model of Morgan et al. (2015). Therefore, the geological layering varies in the offshore domain (and in the cross sections) due to variations in all of the offshore wells. Interpolation of offshore layers used *Topo to Raster*; a GIS technique that is designed to produce smooth and continuous surfaces from scattered point data. This allowed for the generation of continuous spatial distributions of the layer geometry.

Cross section B (CSB) was included based on an AEM survey transect to allow for comparison between AEM and numerical modelling results. CSB passes south of Lake Bonney, between the Admella Dunes and the Cape Banks Lighthouse, extending northward to the Mount Gambier Forest Reserve. CSB also intercepts numerous pumping wells, especially close to its landward limit. Seaward, CSB approaches the Argonaut petroleum well, a key reference for extrapolating the offshore geology in CSB.

Cross section C (CSC) crosses Canunda National Park approximately 4 km southeast of Pether Rock. The landward boundary of CSC is marked by the Reedy Creek B14 Drain, while the seaward extension runs between the Copa and Argonaut offshore petroleum wells. This cross section intercepts several drain cells (Figure 2), which simulate the interactions between the aquifer and surface water features in this area.

Cross section D (CSD) intersects the coastline at Cape Jaffa, extending seaward to a point approximately 12 km north of the Trumpet petroleum well. Its inland boundary lies about 1 km east of Princess Highway.

Cross section E (CSE) is the northernmost cross section simulated in this study, oriented west to east. It crosses the Paranki Lagoon Conservation Park, extends approximately 25 km offshore, and terminates near Bin Bin Road in the landward direction.

The heads on the inland boundary of the cross sections shown in Figures 1 and 2 were extracted from the regional-scale model and set as either constant (in time) values for steady-state models or were time-varying specific heads in transient models. Heads in the regional-scale model were then compared with those of the cross-sectional models (initially without seawater being simulated) to evaluate consistency between the two.

## 2.4 Subsea extension and refinement of cross-sectional models

Cross-sectional models were extended to include the offshore sections of Limestone Coast aquifers (Step 3; Table 1). The offshore wells used for this purpose are illustrated in Figures 1 and 2. Seafloor elevation data was used to establish the top of the model in offshore regions, sourced from the Australian bathymetry and topography grid (https://data.gov.au/data/dataset/australian-bathymetry-and-topography-grid-geoscience-australia). Bottom elevations for extending the top and intermediate model layers were inferred from lithology data from petroleum wells, as provided within the Water Connect database (https://www.waterconnect.sa.gov.au/Pages/Home.aspx). The approximate offshore extent of the cross-sectional models was initially set to 25 km. Figure 3a presents an example of the offshore extension to the onshore part of a cross-sectional model, showing cross-sectional model D (CSD).

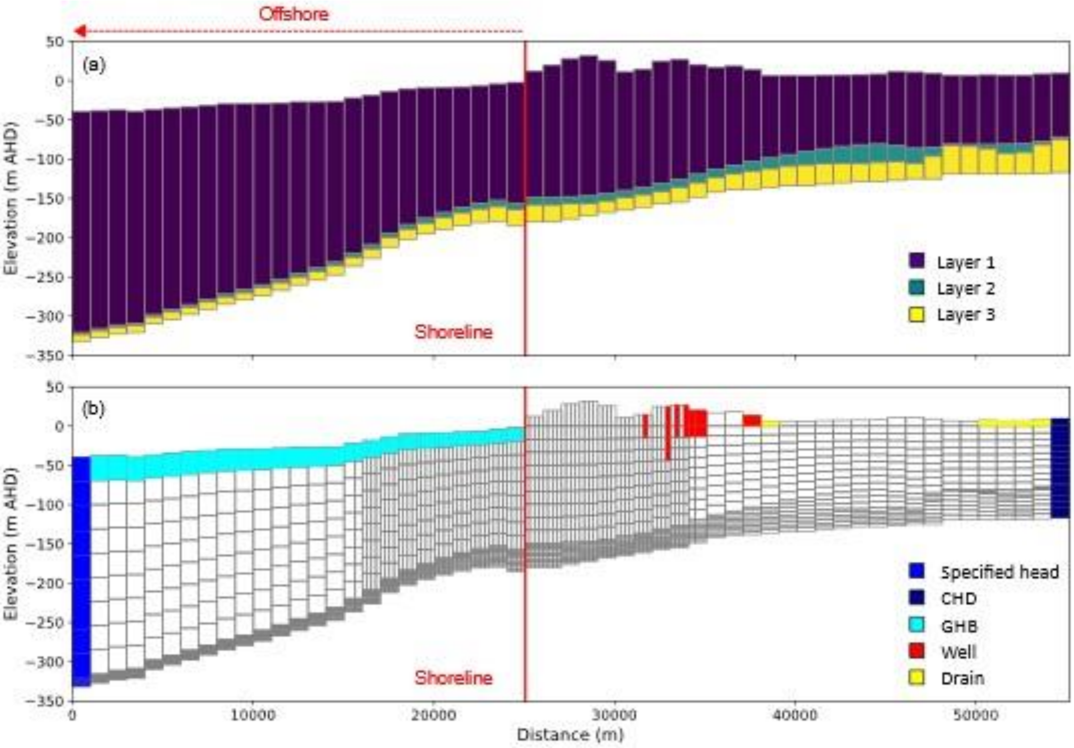

**Figure 3.** Example of model cell refinement for SWI simulations: (a) cross-section extracted from the regional-scale model (cross-sectional model D; see Figure 1 for its location), and (b) the same cross-section after vertical and horizontal refinement. The Time-Variant Specified-Head (CHD) and General Head Boundary (GHB) packages in MODFLOW were assigned to cells along the inland boundary and the seafloor, respectively.

Cross-sectional models were also refined to enable simulation of vertical variations in flow and salinity, along with enhanced horizontal resolution at the freshwater-seawater interface. For CSD, Layer 1 was divided into 10 layers, Layer 2 into 3 layers, and Layer 3 into 6 layers. The horizontal extent of cells was reduced in areas where the freshwater-seawater interface is likely to be found. For example, in CSD, cells near the shoreline were 250.7 m in the horizontal plane, reduced from 1002.8 m in the cross-sectional model that was extracted directly from the parent model. This refinement was necessary to produce a reasonable approximation of the complex zone of mixing between freshwater and seawater. The maximum ratio of each cells horizontal dimension to that of its adjacent cell was 1.6, which approximately reflects the criteria recommended by Anderson et al. (2015), who advised that the ratio of adjacent cell lengths should not exceed 1.5. Cell refinement represented a trade-off between model run times and the accuracy of model calculations, whereby smaller cells provide a higher resolution of calculations and salinity distributions, but require longer model run times. An example of the regional grid, the offshore extension, and the grid refinement is provided in Figure 3b for CSD.

A number of other adjustments were needed to create cross-sectional models from the regional model. For example, pumping cells in the regional model occupied the entire layer in which they occurred (because each stratigraphic layer was a single layer of cells in the regional model), whereas in cross-sectional models, we placed wells in the layers that contained the slotted sections of wells (red cells, Figure 3b). This was done because stratigraphic sequences were resolved into multiple model layers in the cross-sectional models. The proportion of pumping assigned to each layer was proportional to the respective screen length occurring in each layer, for a given pumping well. Similarly, drains (representing groundwater discharge to surface features) were located within the model layer that they occur in cross-sectional models, instead of occupying the entire stratigraphic unit. In doing so, pumping-induced vertical flows within stratigraphic units were captured in cross-sectional models that were neglected in the regional model of Morgan et al. (2015).

## 2.5 Steady-state and transient SWI models

Following the vertical and horizontal refinement of the grid, three scenario types were designed for SWI simulations, as: Scenario 1 – pre-development, steady-state conditions; Scenario 2 – transient conditions (1970–2013); Scenario 3 – projections of steady-state conditions under various contemporary (2013) and future conditions.

Scenario 1 represents steady-state *pre-development* conditions (i.e., prior to the expansion of irrigation across the study area) adopting the aquifer that the conditions in 1970 reflect a modified situation since European settlement. The results of pre-development simulations were treated as baseline conditions from which landward seawater movements were assessed, thereby serving as initial conditions in transient simulations. Steady-state results were obtained by running models for sufficient durations to reach stable conditions, requiring some 30,000 years of run time for models of SWI, starting from initially fresh conditions and allowing the seawater to penetrate the aquifers until an equilibrium state was obtained. Given that sea levels have varied substantially over the past 30,000 years (e.g., sea levels of 30,000 years ago were around 125 m lower than today), it is possible that the seawater extent in the aquifer is still responding to past paleo-sea level changes. However, we have neglected the paleo-history of both sea level variations and sediment deposition/erosion in our investigation, primarily because this would add considerable modelling analysis to the project that may or may not affect the modern seawater extent in the aquifer. It is likely that paleo-conditions are more relevant to the freshwater-seawater extent in the TCSA rather than the TLA, given the findings of previous investigations of offshore aquifers (e.g., Morgan et al., 2018).

The main solute transport parameters were taken from literature values, and considering simple relationships between solute transport parameters and other aquifer properties. For example, porosity was set to the specific yield ($S_y$) of the regional model. Longitudinal dispersivity ($\alpha_L$) was assigned a value of 12.5 m, determined after a wide range of values were tested within a trial-and-error approach, whereby numerical stability required a higher dispersivity but a lower dispersivity produced more realistic freshwater-seawater mixing zone widths, reflecting typical field conditions observed in aquifers with higher-density monitoring of the coastal salinity distribution (e.g., Cooper, 1964). This is notwithstanding the considerable variability in mixing zone widths observed within field studies of coastal aquifers, and the generally poor understanding of the local-scale processes affecting seawater intrusion in karst aquifer systems (Werner et al., 2013). It is worth noting that dispersivity acts as a surrogate for heterogeneity, making it challenging to determine the appropriate value for specific field sites (Lee et al., 2018). Early models adopting $\alpha_L$ values $\geq 50$ m resulted in overly dispersed mixing zones and near-vertical freshwater-seawater interfaces, which is probably unrealistic based on the collective experience of the authors. Both transverse and vertical dispersivities ($\alpha_T$ and $\alpha_V$, respectively) were set at 0.075 m. The small $\alpha_T$ value aligns with the findings of the review undertaken by Zech et al. (2019), who observed that the most reliable investigations of dispersion parameters reported relatively low (< 1 m) $\alpha_T$ and $\alpha_V$ values in previous studies. The total variation diminishing (TVD) scheme was used to solve the advection-dispersion equation (Zheng and Bennett, 2002), because this approach is known to minimise artificial dispersion and numerical errors, while providing solutions within reasonable timeframes.

Some other adaptations were needed to create cross-sectional models of SWI. For example, the seaward boundary conditions at the vertical left-hand model boundary (offshore) adopted a constant seawater head of 0 m AHD, with any incoming flow occurring at the seawater concentration. The inland boundary was modelled using the Time-Variant Specified-Head (CHD) package in MODFLOW 2000, while the seafloor was represented by a head-dependent flux condition using the General Head Boundary (GHB) MODFLOW 2000 package. In this setup, the salinity of any incoming flux was also set to seawater concentration (Figure 3b), following a similar approach to that used by Solórzano-Rivas and Werner (2018).

The results of the steady-state pre-development simulations were used to evaluate inland and offshore positions for truncating 2D models, whereby the onshore seawater and offshore freshwater extents were captured within the model domain. The landward boundary was shifted inland so that any SWI within modelling scenarios was likely to be accommodated. An assessment was made as to whether seawater encroached on the inland boundary for all modelling scenarios, and where necessary, a landward shift occurred as needed.

Scenario 2 involved transient simulations, covering the period 1970–2013. The pre-development, steady-state models were used to generate initial conditions for transient simulations. In transient models, the stressors (e.g., recharge, pumping) were extracted from the regional model (Morgan et al., 2015), while the model grid, solute transport parameters and the numerical solver were the same as those used in the steady-state model. The salinity distribution at the end of the transient simulation was compared to the pre-development salinity distribution to evaluate SWI within Limestone Coast aquifers during the 44-year period of simulation.

Scenario 3 involved four simulations to assess future conditions, including:

- (3a) future steady-state conditions under the average climate stresses of 2004–2013 and the mean pumping (considering both the TLA (Layer 1) and TCSA (Layer 3)) of 2013,
- (3b) the same as (3a) except with the effects of sea-level rise,
- (3c) the same as (3a) except with reduced recharge due to climate change impacts (to approximate the scale of rainfall changes under climate change effects by the year 2050), and
- (3d) the same as (3a) except with modified pumping to estimate the increase in extraction to full allocation levels by the year 2050.

The reduction in recharge is consistent with the investigation by DEW (2023), which examined future climate impacts using projections from RCP 8.5 to 2050 (DEW, 2022), predicting an 18% recharge reduction in response to the 6% rainfall decline. DEW (2023) also adopted an increase in pumping of 71%, representing a rough estimate of the extraction that would occur under full allocation. Scenario 3a adopted average stresses (recharge, evapotranspiration, etc.) from the period 2004–2013, assuming that the pumping conditions of 2013 persist into the future. The purpose of Scenario 3a is to provide insights into the stability of the seawater wedge, specifically to determine whether the seawater wedge is likely to move inland in the future under “existing” (in 2013) conditions. Scenario 3a assesses the eventual inland distance the seawater wedge may reach, and whether the wedge reached a stable condition in 2013 (at the end of the transient simulation). In this way, Scenario 3a provides an approximation of the eventual landward extent of seawater for periods extending beyond the 44-year timeframe of the transient simulations, assuming “business (and climate) as usual”.

Scenario 3b builds on the conditions of Scenario 3a by raising the sea level by 0.3 m, as an approximation of sea-level rise, which is expected to be between 0.13 m and 0.33 m by 2050, according to URPS (2015). The higher sea level was assigned for the entire simulation duration, rather than adopting a gradual increase, as occurs in reality. Here, the inland boundary conditions, the recharge and the pumping are identical to Scenario 3a – i.e., sea-level rise was applied to the cross-sectional model while using the inland boundary heads representing the situation without sea-level rise. This is a type of worst-case sea-level rise scenario, because the heads would be expected to rise at the inland boundary with sea-level rise, and by maintaining them at the conditions without sea-level rise, we are adopting the “head-controlled” condition of Werner and Simmons (2009), rather than “flux-controlled” conditions, where the former is known to cause worse SWI than the latter. A future simulation that imposes sea-level rise in the regional model, prior to extracting the stressors for the cross-sectional models, would allow for an assessment of SWI under less conservative conditions (i.e., where the inland boundary head is allowed to rise in response to sea-level rise, as occurs in flux-controlled conditions according to Werner and Simmons (2009)). We expect that the relatively large distances to the inland boundaries of models likely reduce the effect of the inland boundary condition on SWI.

Scenario 3c modifies the conditions of Scenario 3a by reducing recharge by 18% consistent with the analysis by DEW (2023), in which a scaling factor of 3 was adopted in reducing recharge in response to the 6% rainfall decline projected by climate change models (Green et al., 2012), leading to an 18% decline in recharge. This was firstly applied to the regional groundwater model of Morgan et al. (2015) prior to the extraction of cross-sectional model stressors from the regional model. In this way, the inland boundary in the cross-sectional models reflects the regional effects of the recharge decline, in addition to the local effects of recharge applied directly to cross-sectional models.

Scenario 3d adopts pumping rates that are higher by 71%, which is the increased pumping assumed by DEW (2023) reflecting extraction rates at full allocation by 2050. As with Scenario 3c, the pumping change is applied to the regional model prior to the construction of cross-sectional models, and therefore, the effects of pumping change on cross-sectional models are manifested in both the heads at the landward boundary and in the change to pumping rates within cross-sectional models. Table 2 summarizes the SWI scenarios used in the current study.

**Table 2.** Summary of model scenarios used for SWI simulation.

| Scenario | Aim | Simulation period (years) | Recharge | Evapotranspiration | Pumping | Inland boundary condition |
|---|---|---|---|---|---|---|
| 1 | Establish initial, steady-state seawater distribution | 30,000 | Constant value, taken from the regional-scale model (pre-1970) | Constant value, taken from the regional-scale model (pre-1970) | None | Constant head extracted from the regional-scale model |
| 2 | Simulate transient seawater movements during 1970–2013 | 44 (1970–2013) | Time-varying, taken from the regional-scale model (1970–2013) | Time-varying, taken from the regional-scale model (1970–2013) | Time-varying, historical pumping (1970–2013) | Time-varying head extracted from the regional-scale model |
| 3a | Predict long-term, steady-state SWI | 30,000 | Constant recharge – average of 2004–2013 in the regional-scale model | Constant evapotranspiration – average of 2004–2013 in the regional-scale model | Constant pumping - average of 2013 pumping | Constant inland head – average of 2004–2013 in the regional-scale model |
| 3b | Predict long-term, steady-state SWI caused by sea-level rise of 0.3 m | 30,000 | Constant recharge – average of 2004–2013 in the regional-scale model | Constant evapotranspiration – average of 2004–2013 in the regional-scale model | Constant pumping – average of 2013 pumping | Constant inland head – average of 2004–2013 in the regional-scale model |
| 3c | Predict long-term, steady-state SWI caused by an 18% decline in recharge | 30,000 | Constant recharge – 18% lower than the average of 2004–2013 in the regional-scale model | Constant evapotranspiration – average of 2004–2013 in the regional-scale model | Constant pumping – average of 2013 pumping | Constant inland head – average of 2004–2013 in the regional-scale model with an 18% recharge reduction |
| 3d | Predict long-term, steady state SWI caused by a 71% increase in pumping | 30,000 | Constant recharge – average of 2004–2013 in the regional-scale model | Constant evapotranspiration – average of 2004–2013 in the regional-scale model | Constant pumping – 71% higher than the average of 2013 pumping | Constant inland head – average of 2004–2013 in the regional-scale model with a 71% increased pumping |

# 3 Results

This section describes the results of five cross-sectional models; the locations of these are shown in Figure 1. The results of cross section E (CSE) are presented in the main body of the report, while the results of cross sections A to D (CSA to CSD) are provided in the Appendices. Figure 2 also outlines the boundary of the regional *parent* model of Morgan et al. (2015) that was used as the basis for cross-sectional model parameters, showing the locations of wells, drains and the position of offshore oil wells that allowed for coastal aquifer models to be extended into the continental shelf. Results are presented at various steps within the workflow to demonstrate the changes introduced with each step, such as the extraction of cross sections from the regional model, changes to the grid, extrapolation into the continental shelf, and the addition of density effects, to give the reader confidence that cross-sectional models reasonably reflect the parent model simulations of groundwater heads and flow.

## 3.1 Cross section E: Groundwater flow model construction

Here, the outcomes of Steps 1 to 3 in the modelling approach (see Table 1) are shown for cross section E (CSE). Figure 4 illustrates the grid for CSE extracted from the regional model, truncated to focus on the coastal zone, and extended offshore. Corresponding figures for cross sections A to D (CSA to CSD) are included in Appendix B.

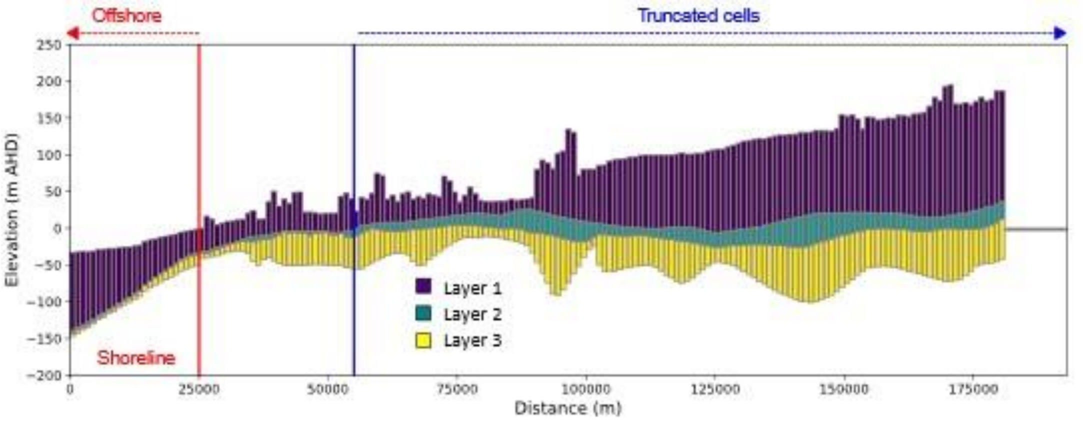

**Figure 4.** Grid extracted from the parent model of Morgan et al. (2015) for cross section E, showing the region where cells were removed (Truncated cells), and the extrapolation of the cross section into the continental shelf (Offshore), with the shoreline location shown as the red vertical line.

The heads in CSE were compared to the corresponding cells in the parent 3D model for steady-state, pre-development conditions (Step 4; Table 1). The results are shown in Figure 5 for the CSE model that adopts the same coastal boundary condition as that used by Morgan et al. (2015), and assigns steady-state heads from Morgan et al. (2015) as the inland fixed-head boundary condition. The largest negative and positive biases were -0.46 m and 1.02 m, respectively, shown as the darker blue and red cells in Figure 5. Here, a positive bias means that CSE produced higher heads than the parent model, whereas the heads were lower in CSE than in the parent model where the bias is negative. Although we consider the scale of these biases to be acceptable, further investigation is warranted to explore the cause of these given the many possible reasons that these may have arisen out of the CSE construction methodology. Note that the bias at the inland boundary of CSE is zero because heads from the parent model were assigned to the inland boundary through a specified-head condition, and therefore, CSE matches the head exactly at that location. This is also the case at the coastal boundary. The bias distributions of the four other 3-layer cross-sectional models are provided in Appendix C.

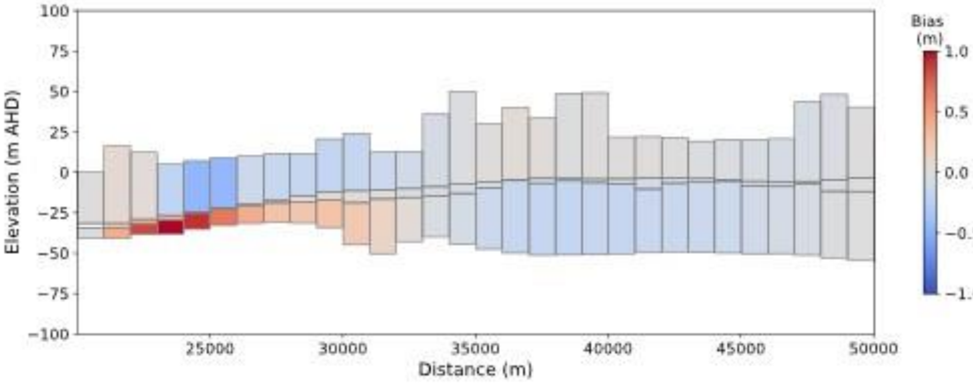

**Figure 5.** Comparison of heads between CSE (only freshwater is simulated) and the parent 3D model for steady-state, pre-development conditions, in terms of the bias, where a positive bias indicates that CSE heads are greater than the parent model. Heads from the parent model were transferred directly to specified-head conditions at the shoreline (left boundary) and the inland limit of the model (right boundary). Note here that the *x*-axis scale reflects distances in the regional model of Morgan et al. (2015) whereas the earlier *x*-axis (in Figure 4) is specific to the cross sections with extended offshore domains. The white cell located on the left boundary belongs to Layer 2 (aquitard) and represents an inactive cell at the shoreline in the regional model.

Next, the CSE model shown in Figure 5 was extended offshore (see Figure 4), and a check of the heads against those of the parent 3D model was repeated. The distribution of head bias is provided in Figure 6, while the corresponding plots for the other cross-sectional models are given in Appendix D. The results show that the bias increased at the coastal boundary once the specified heads of Morgan et al. (2015) were removed and replaced with a representation of the offshore aquifer. Note that the sea was simulated as equivalent freshwater heads (i.e., the heads on the seafloor boundary were assigned the pressure of the ocean at the sea floor, but treating the sea as having the density of freshwater), while the offshore aquifer was treated as containing freshwater (i.e., density effects are neglected in freshwater-only simulations). Thus, it appears that the explicit simulation of the sea provides alternative heads at the shoreline relative to those used by Morgan et al. (2015). Comparison to field measurements of groundwater heads near the coast is warranted to assess whether the more physically based simulation of the coast adopted in CSE has produced a more reliable prediction of near-shore groundwater heads than those adopted by Morgan et al. (2015). This would require the installation of near-coastal wells is various locations, given that there are few of these in the study area.

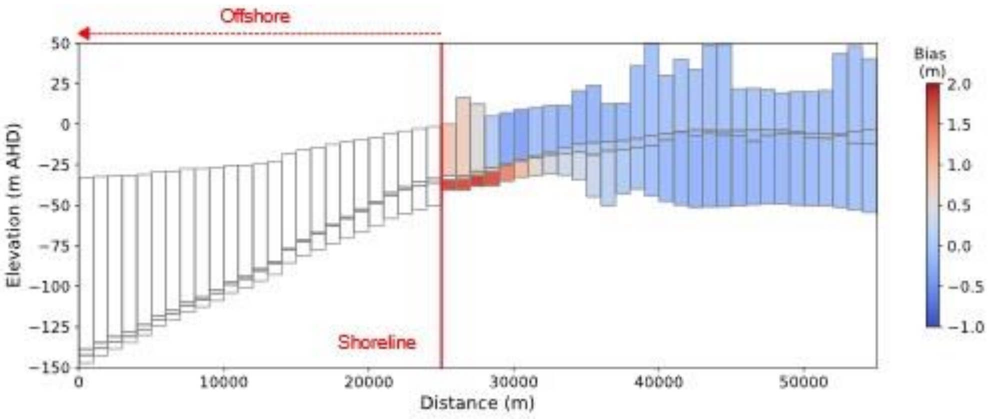

**Figure 6.** Comparison of heads between CSE (with offshore extension, only freshwater is simulated) and the parent 3D model for steady-state, pre-development conditions, in terms of the bias, where a positive bias indicates that CSE heads are greater than the parent model. Heads from the parent model were transferred directly to specified-head conditions at the inland limit of the model (right boundary), whereas the coastal boundary condition adopts the equivalent freshwater heads of the sea. Offshore cells are blank because these were not used in the parent model. The white cell located near the shoreline (onshore part), belongs to Layer 2 (aquitard), and represents an inactive cell at the shoreline in the regional model.

The next step in the model construction was to refine the grid (Step 5; Table 1). An example of this step leading to a refined grid within the vicinity of the freshwater-seawater interface is provided in Figure 3 for CSD. Figure 7 shows the refined grid for CSE, along with head values (shown as a colour flood), along with the corresponding heads in the parent model (interpolated to the location of CSE; Figure 7a), to show the match between this form of CSE and the original regional-scale model. Refinement of the grid in the horizontal direction was undertaken to ~15 km offshore and ~10 km onshore, resulting in a refined cell length of 25 m in these areas. This was intended to focus the numerical effort on parts of the modelling containing both seawater and freshwater, because freshwater-seawater mixing is a complex process that can only be properly simulated with sufficiently small cells (Werner, 2017a). The model's first layer was divided into ten sub-layers, the second into three, and the third into three – to allow for the vertical stratification of salinity (and associated water density) to be simulated. The ratio of cell lengths (in the horizontal direction) between adjacent cells was up to 1.6. The results for CSA to CSD are given in Appendix E.

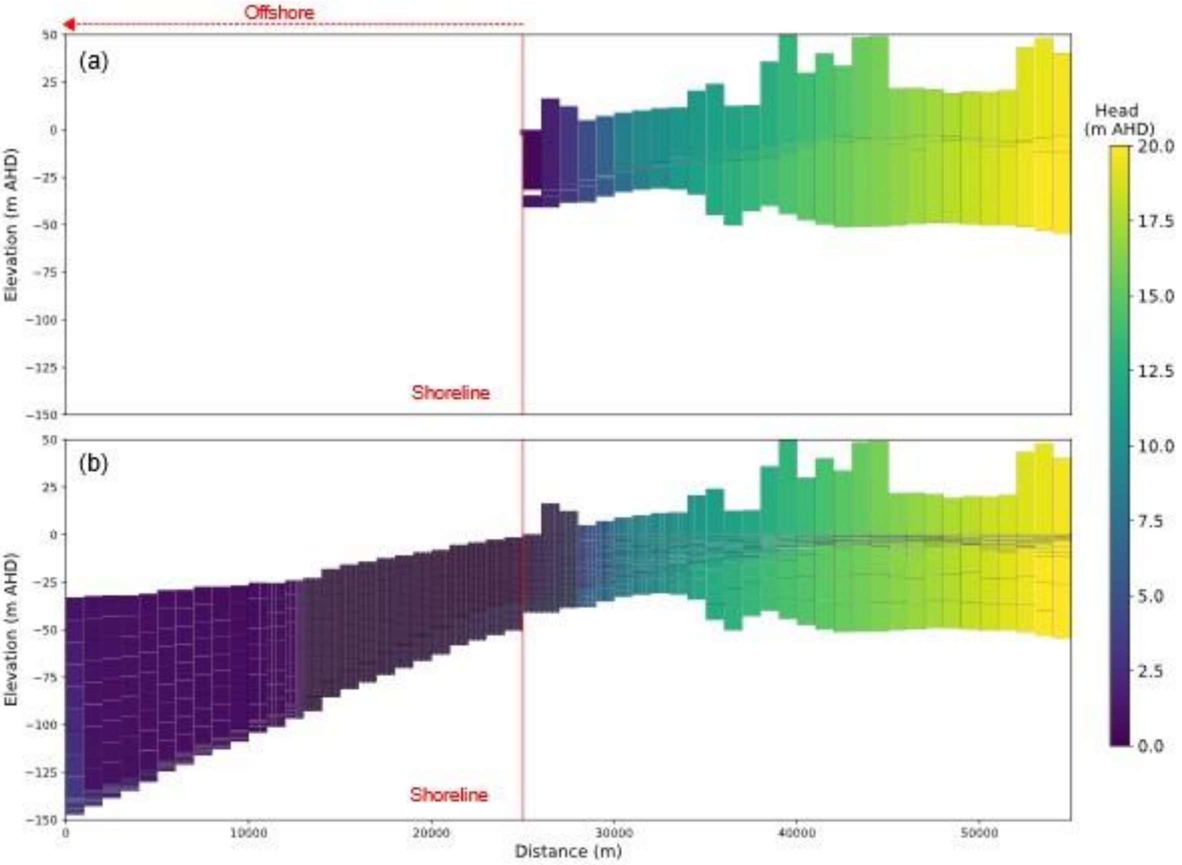

**Figure 7.** Comparison of heads between: (a) the parent 3D model at the location of cross section E (CSE), and (b) CSE with offshore extension and refined grid (only freshwater is simulated). This simulation represents steady-state, pre-development conditions. The white cell in (a), located near the shoreline, belongs to Layer 2 (aquitard), and represents an inactive cell at the shoreline in the regional model.

The results in Figure 7 demonstrate reasonable agreement between the extended, refined grid of this version of the CSE model and the parent model results extrapolated to the location of CSE. This result gives confidence that the methodology for extracting cross-sectional models from the regional model of Morgan et al. (2015) was effective in reproducing the parent model conditions.

Following completion of the pre-development, steady-state simulations (seawater is not considered, and we neglect density effects; this is referred to as “freshwater only” in the remainder, even though the terrestrial groundwater that is simulated in these cases is often not fresh in regions across the Limestone Coast), adopting the various model grid extents and resolutions shown in previous figures, the CSE model was assigned the transient stresses of the parent model to reflect the simulation period 1970–2013. For example, a time-varying specified-head condition was adopted at the inland boundary, with heads extracted from the parent model, while recharge and other hydrological stresses in CSE were also extracted from the regional model. As CSE is aligned with the principal axes of the rectilinear grid of Morgan et al. (2015), the stresses could be transferred directly from the parent model to CSE, without needing to average the stresses from multiple cells in the parent model. Other cross-sectional models that are not either north-south or east-west in their orientation required averaging procedures because each CSE cell corresponds with parts of multiple cells in the parent model. The methods for achieving this are described in Appendix A.

The CSE model grid initially adopted was the same as that shown in Figure 5, except the stresses are transient instead of steady state. Four groundwater level hydrographs from the parent model and at corresponding locations in the CSE are provided in Figure 8, while Figure 9 illustrates the bias at the end of the transient simulation. Corresponding plots for the other cross-sectional models are given in Appendix F (comparisons of hydrographs) and Appendix G (bias at the end of the transient simulation).

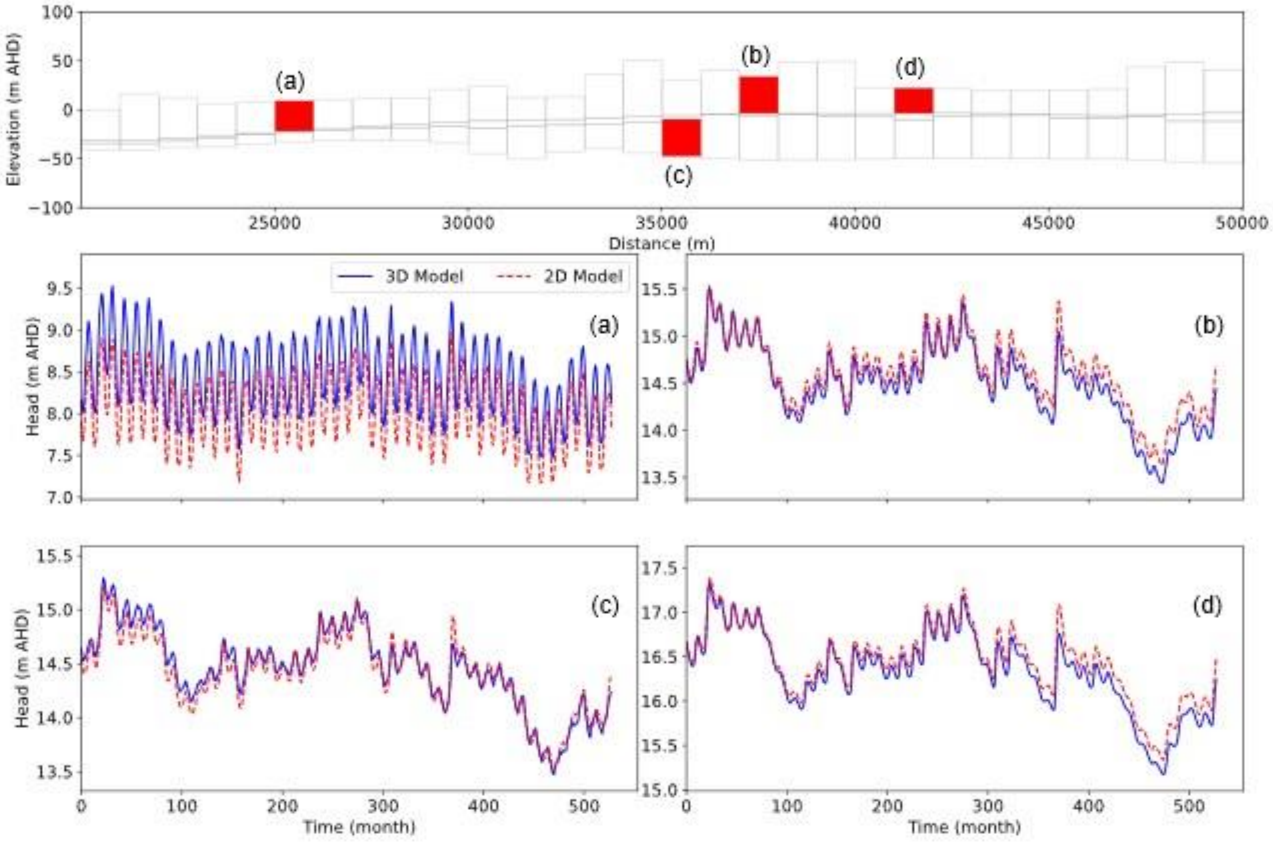

**Figure 8.** Four hydrographs comparing heads from the transient simulation (freshwater only) of cross section E with the parent 3D model. The top figure identifies the cells from which model hydrographs, (a) to (d), were extracted. The distribution of bias in the pre-development steady-state model (used as initial conditions for the transient model) is shown in Figure 5, while the bias at the end of the transient simulation is shown in Figure 9.

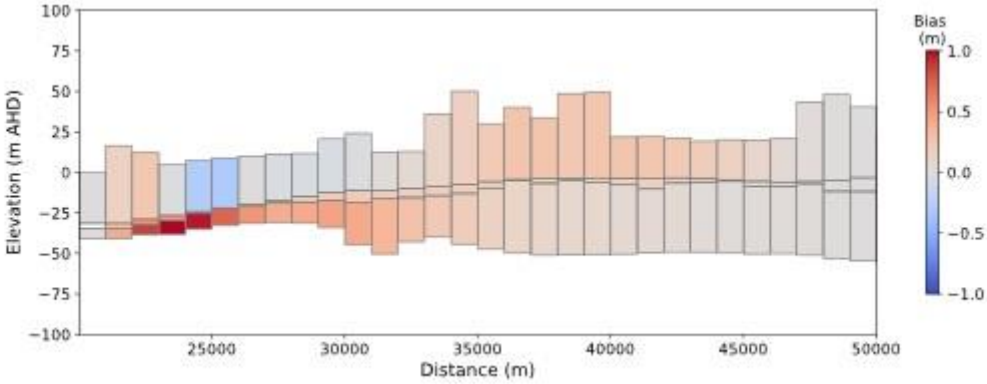

**Figure 9.** Comparison of heads from cross section E (CSE; transient simulation, freshwater only) and the parent model at the end of the transient simulation (1970–2013), where positive bias indicates that the heads of CSE exceed those of the parent model. The white cell located on the left boundary belongs to Layer 2 (aquitard) and represents an inactive cell at the shoreline in the regional model.

Figures 8 and 9 show that the regional model dynamics is reproduced reasonably well in CSE, given the closeness of hydrographs (Figure 8) and the adequately low bias (Figure 9). The bias at the beginning of the transient simulation (Figure 5) is somewhat similar to the bias at the end (Figure 9), although it appears that the CSE heads rose relative to the regional model during the transient simulation, as the bias tended to increase slightly (cell colours trend towards red, comparing Figures 5 and 9) over the course of the simulation. Note here that the bias in Figure 9 is consistent with the hydrographs presented in Figure 8. The main reason for this bias stems from inherent differences between 2D and 3D models, whereby extracting a cross section from a 3D model eliminates perpendicular flow components, leading to variations in head values. Other sources of bias have arisen from the methodology used to extract the cross sections.

## 3.2 Cross section E: Seawater intrusion model construction

### 3.2.1 Scenario 1: Pre-development, steady-state seawater extent

Once the truncated, offshore-extended, grid-refined cross-sectional models of groundwater flow were created (Steps 1 to 5; Table 1; Figure 7 shows the resulting grid for CSE), solute transport and density effects were added to the models to allow for the simulation of the seawater extent within the coastal aquifers. Figure 10 presents the freshwater-seawater distribution for pre-development, steady-state conditions in CSE, showing the truncated, offshore-extended and refined model grid. These results represent the salinity distribution, with aquifer stresses from 1970 imposed, after some 30,000 years. Figure 10 shows that seawater in the upper aquifer (TLA) penetrates only 124 m inland, while there is an extensive body of “freshwater” (or at least groundwater of terrestrial origin) in the lower aquifer (i.e., the freshwater head is sufficient to push the seawater offshore). The landward extent of seawater in the TLA is only observable in the close-up of the near-shore aquifer because the high density of cells in the larger-scale figure doesn’t allow the salinities to be shown in fine detail. The limited penetration of seawater in the aquifer is the consequence of the high groundwater heads, being some 8 m above sea level at 5 km inland from the coast (see Figure 8). With this head gradient and the high hydraulic conductivity (*K*) of the coastal aquifer (e.g., the TLA aquifer *K* is around 115 m/d near the coastline), the offshore discharge of groundwater is expected to be considerable. The seawater distributions obtained from CSA to CSD are provided in Appendix H.

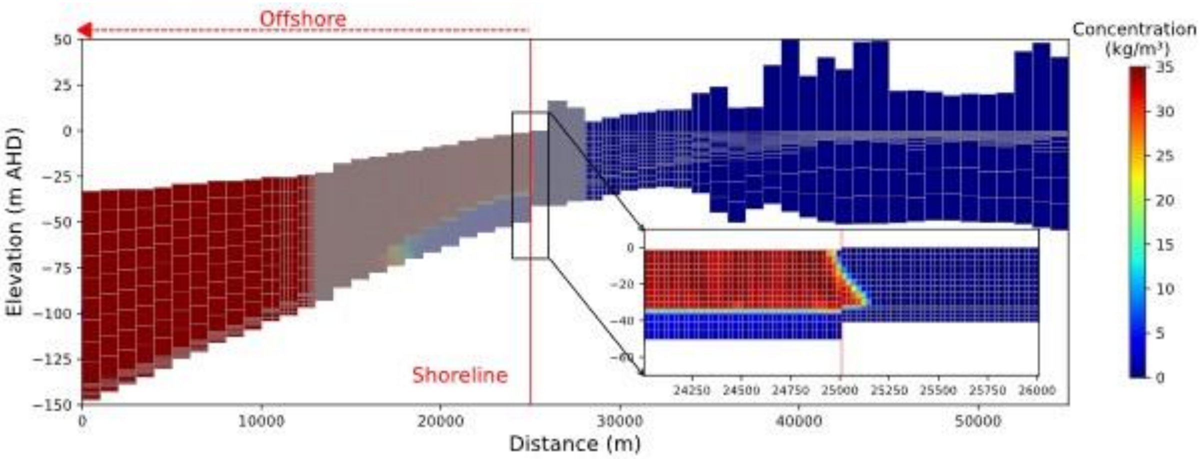

**Figure 10.** Salinity distribution of cross section E (CSE), representing pre-development, steady-state conditions. The grey shading near the shoreline in the main figure is due to the high concentration of grid cells. Grid refinement involved the subdivision of regional model cells into 40 smaller cells (in CSE) for simulation accuracy.

The close-up of the near-shore saltwater wedge in Figure 10 shows colour variations (i.e., light-dark shading of the red region shown in the inset close up of the saltwater region), indicating that mixing is occurring in the model between the freshwater in the TCSA (lower aquifer) and the overlying seawater in TLA. This produced complex patterns in the TLA, in the form of unstable fingering. This is characteristic of density-driven flow instabilities, where the freshwater and seawater mixing becomes irregular, resulting in complex patterns. These processes were investigated by Solórzano-Rivas et al. (2021), who showed the variability in buoyancy-driven freshwater plumes expected in subsea sediments under a range of conditions.

Figure 11 provides the head distribution from the density-dependent simulation of pre-development steady-state conditions at CSE (the corresponding salinity contours are shown in Figure 10). Note that the heads in the seawater zone are relative to the salinity of each cell, such that the equivalent freshwater head in a cell containing seawater is higher than the equivalent freshwater head in a cell containing freshwater but having the same reported head, due to the higher density of seawater. This influences the direction and rates of groundwater flow. For example, even where the groundwater levels of two cells are the same, groundwater will move from the cell with higher water density to the one with lower density. For this reason, the effects of salinity on the heads must be considered in comparing the heads of SWI models to freshwater-only models. Given that almost all of the onshore aquifer contains only freshwater, this is an issue in very few cells for CSE. The results in Figure 11 indicate that the head consistency obtained in the freshwater-only versions of CSE is adequately retained with density effects added to the model. We conclude from this that CSE, as a SWI simulator, is a reasonable reproduction of the regional model hydrogeology produced by Morgan et al. (2015). Appendix I shows this comparison for other cross sections (CSA to CSD).

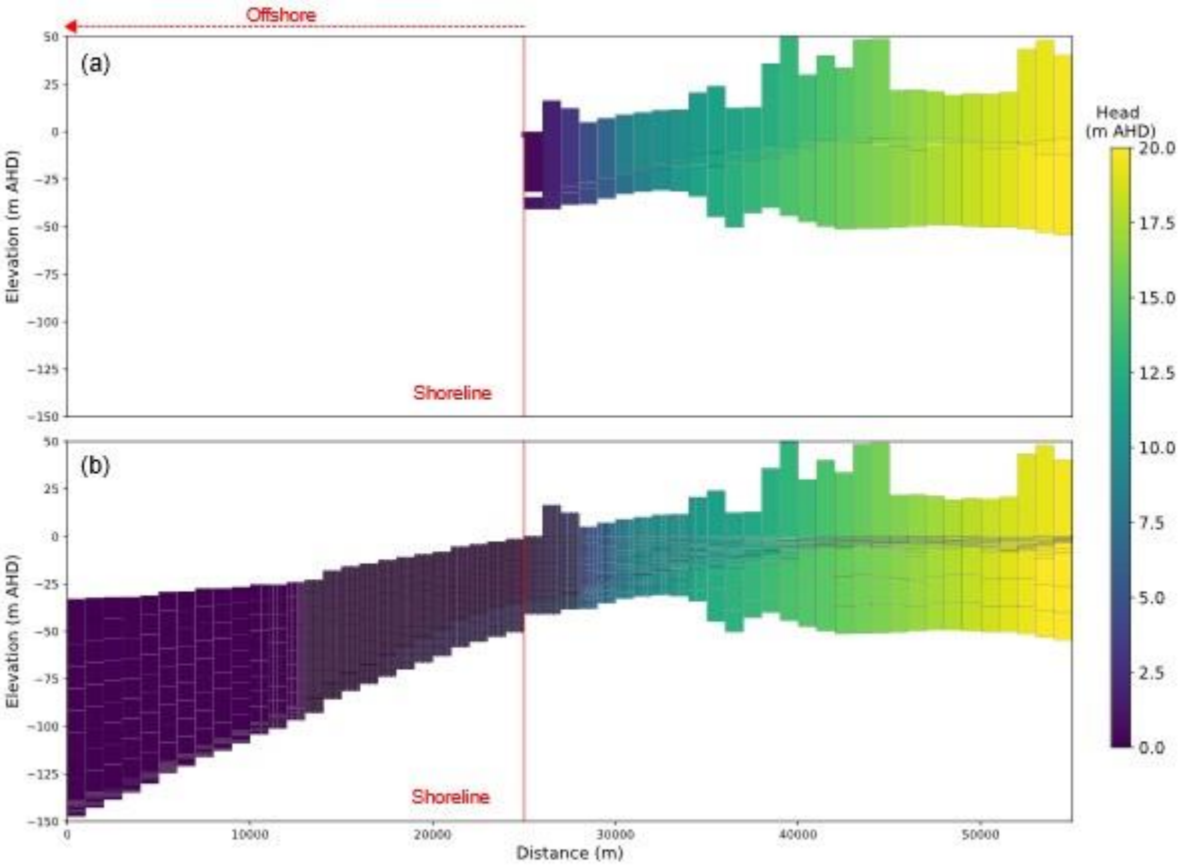

**Figure 11.** Comparison of heads between: (a) the parent model of Morgan et al. (2015), and (b) cross section E (density-dependent, steady-state, pre-development simulation of freshwater-seawater interactions). The white cell in (a), located near the shoreline, belongs to Layer 2 (aquitard), and represents an inactive cell at the shoreline in the regional model.

### 3.2.2 Scenario 2: Seawater intrusion, 1970–2013

Figure 12 presents the freshwater-seawater distribution at the end of the transient simulation using the truncated and grid-refined version of CSE. The results show negligible changes in the groundwater salinity of the upper and lower layers compared to the pre-development condition, suggesting that SWI is unlikely to have occurred during 1970–2013 in this location. To assess the reasons for this stability in the seawater extent, Figure 13 shows the difference in heads between the pre-development, steady-state condition and the end of the transient simulation. The results highlight the limited net changes in groundwater levels at this site during 1970–2013 – this is the primary reason for the stability in the seawater extent in CSE. Note that there is no pumping in CSE. The seawater distributions at the end of the transient simulation (1970–2013) from CSA to CSD are provided in Appendix J, which shows more extensive seawater movements under the stresses of 1970–2013.

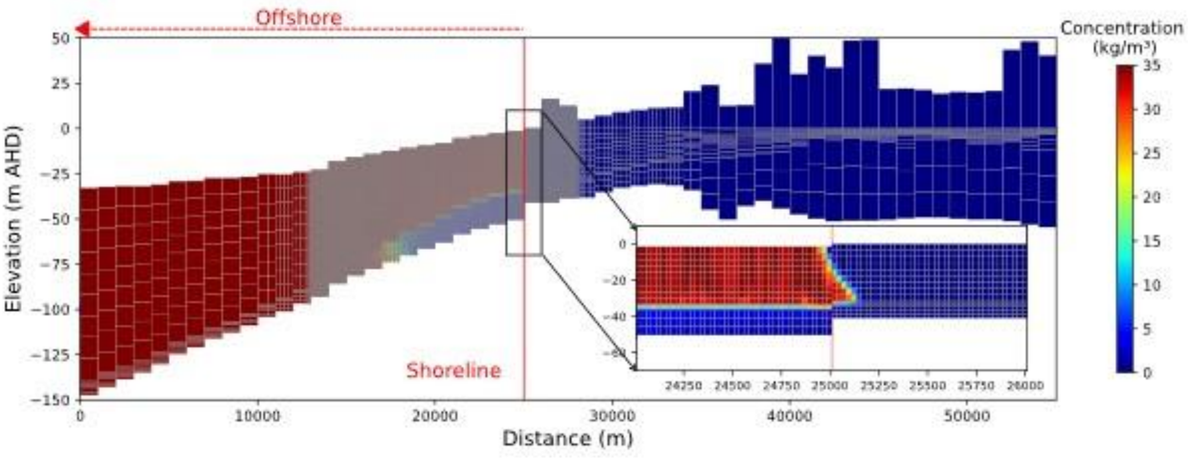

**Figure 12.** Spatial distribution of salinity at cross section E at the end of the transient simulation (1970–2013).

Figure 13 shows the groundwater head distributions corresponding to the SWI models shown in Figures 10 and 12. Comparing the two head distributions provides insight into head changes within CSE over the period 1970–2013. The results indicate negligible changes in the head distribution, consistent with the finding that the freshwater-seawater distribution changed minimally over the same timeframe, as evident from a comparison of Figures 10 and 12. The groundwater head distributions of the SWI models for CSA to CSD are included in Appendix K.

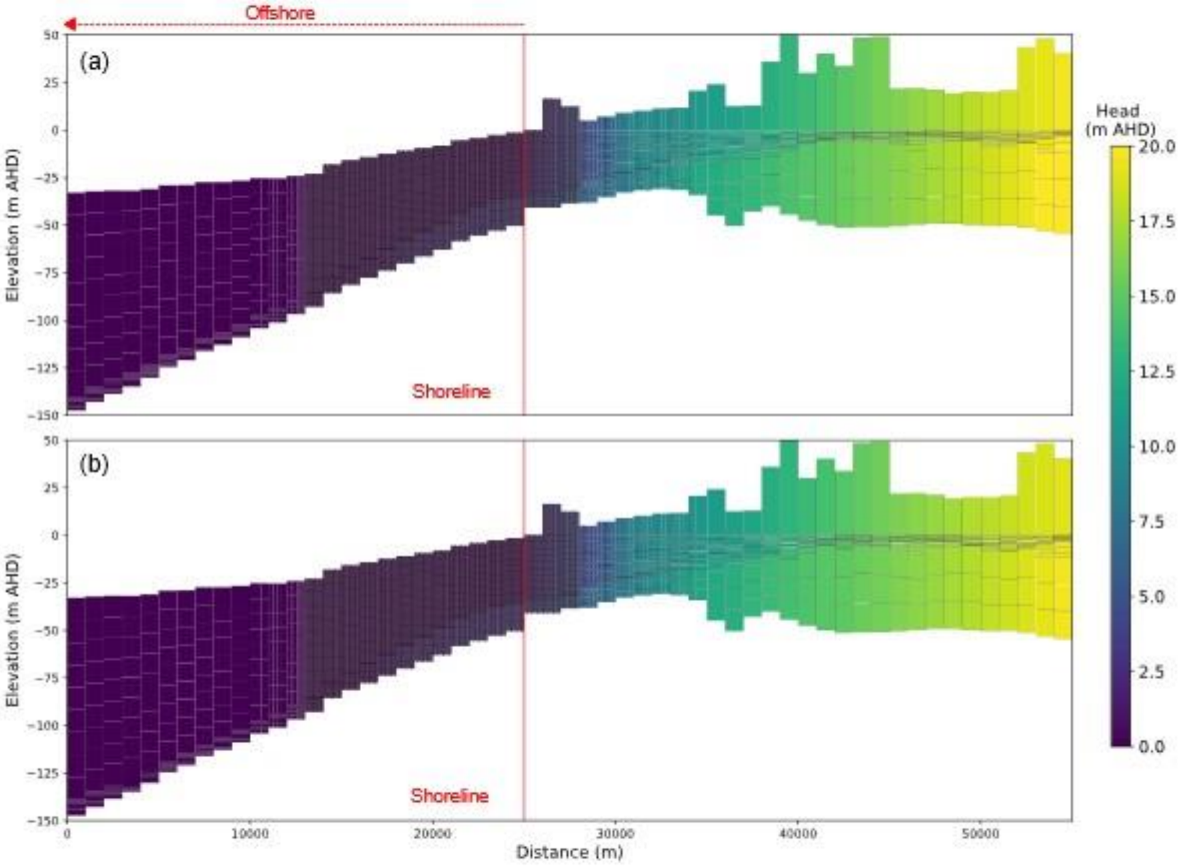

**Figure 13.** Head distributions during the transient simulation period (1970–2013) within cross section E (CSE), showing: (a) head distribution under pre-development conditions, and (b) head distribution at the end of the transient simulation (1970–2013).

### 3.2.3 Comparison to field salinities

The modelling results for CSE were assessed by comparing the salinity predictions to existing field measurements of groundwater salinity proximal to the axis of CSE. Figure 14 presents the distribution of wells near CSE that have electrical conductivity (EC) data. Only EC data for the TLA was available in this location, likely because most of the pumping wells in the Limestone Coast draw from the TLA. The simulated toe location (where the seawater wedge intercepts the bottom of the aquifer) from the pre-development, steady-state model is shown for the TLA (upper aquifer), while the tip (where the seawater wedge intercepts the top of the aquifer) is omitted because it occurs approximately at the shoreline in the unconfined TLA. Although the pre-development, steady-state numerical modelling results are used for comparison, the discussed results are applicable to all CSE scenarios tested in this study, as the changes in toe location for each CSE scenario are effectively imperceptible at the scale of Figure 14. The simulated toe and tip in the lower aquifer (TCSA) are offshore and are therefore not shown in Figure 14 (note that the extent of offshore freshwater in the TCSA is apparent in Figure 12, at the end of the transient simulation of CSE, and in other figures to follow for the results of scenarios). The distribution of wells near CSA to CSD that have electrical conductivity (EC) data are provided in Appendix L.

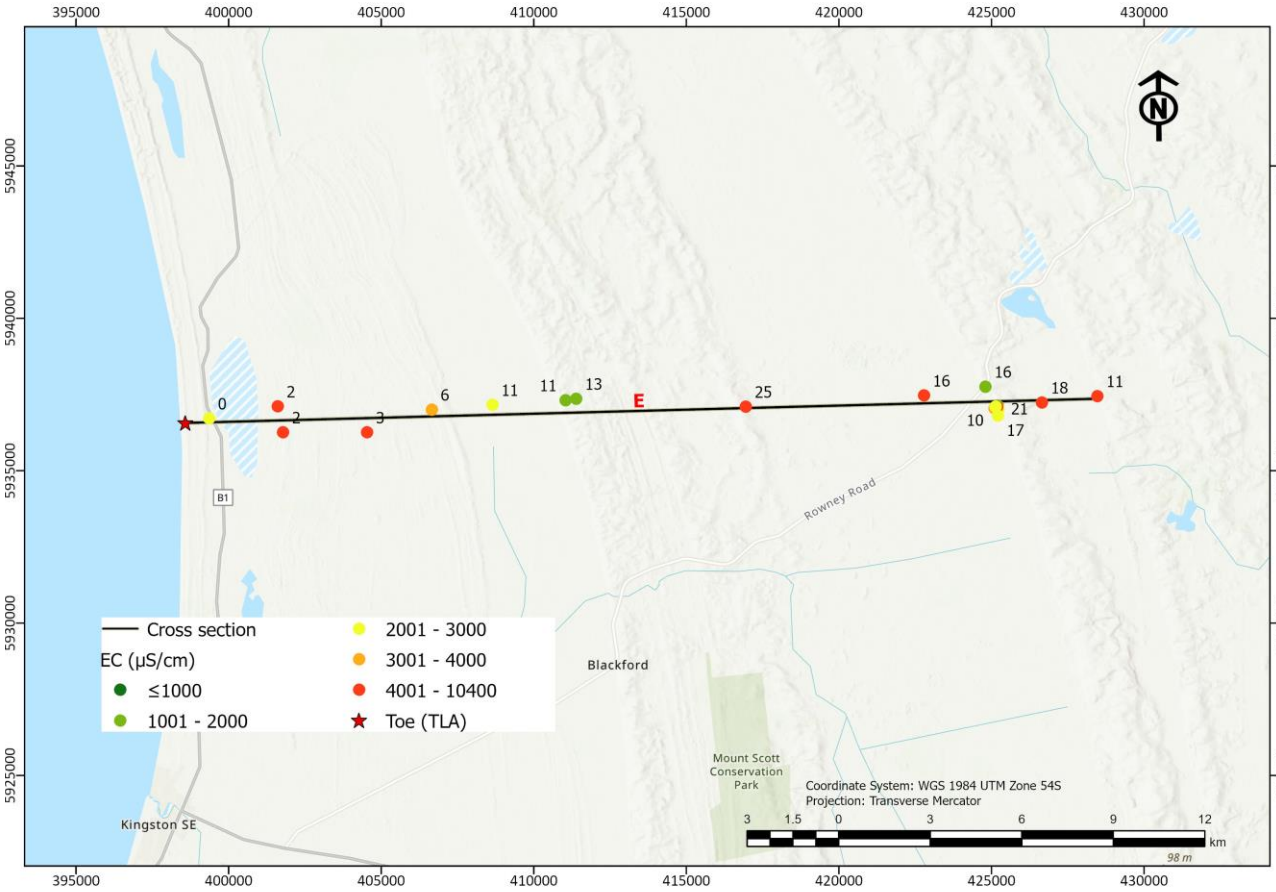

**Figure 14.** Location of wells with salinity data proximal to cross section E for the TLA (upper) aquifer. The numbers next to wells indicate the elevation of the bottom of the wells, rounded to the nearest integer, in m AHD, where 0 m AHD is sea level. The tip of the seawater wedge in the TLA is approximately at the shoreline. The toe location for the TLA is shown by the red star, while the TCSA toe is omitted because it is offshore. Toe locations were taken from pre-development conditions (see Figure 10).

Figure 14 indicates that there are significant areas of saline groundwater (EC >4,000 µS/cm) observed in wells installed in the TLA, occurring at locations of up to 31 km from the coast. The bottom of the wells shown in Figure 14 vary from 0 m AHD to 36 m AHD, and therefore, the salinity of only the shallow groundwater has been assessed. For a monitoring well to be used as a sentinel well for seawater intrusion, it must be installed below sea level, preferably below the mid-depth of the aquifer. Thus, the saline groundwater encountered in observation wells along the transect of CSE is not associated with modern seawater processes or seawater intrusion occurring in recent decades. This conclusion arises from: (a) the high groundwater levels of this area that are more likely to force the seawater wedge close to the shoreline, and (b) the occurrence of high salinity groundwater at elevations above mean sea level cannot be caused by modern seawater movements. A hydrochemical and environmental isotope analysis would be needed to ascertain the origins of the saline groundwater encountered in the observations wells proximal to CSE, but the evapoconcentration of rainfall is a likely contributing factor amongst other possibilities. Mustafa et al. (2012) investigated the water chemistry of the coastal aquifers of the Lower Limestone Coast, but their analysis didn't extend as far north as CSE. Their findings suggest that, in general, saltwater derives from multiple salinity sources in the Lower Limestone Coast.

The current study includes a comparison between cross-sectional models and recent AEM survey results for CSA and CSB, which coincide with AEM flight lines (Appendix Q).

### 3.2.4 Scenario 3: Steady-state scenarios to assess future seawater intrusion

Here, we present the results of steady-state simulations (obtained by long-term time-marching) that provide guidance on future SWI at the location of CSE. Four scenarios are presented, as described in Section 2.5.

***Scenario 3a:*** This scenario aims to assess the steady-state seawater extent that arises when stresses from the latter stages of the transient simulation (1970–2013) are applied for a prolonged period (~30,000 years). We consider this a business-as-usual case, and a baseline for testing the effects of sea-level rise (Scenario 3b), recharge change (due to climate change; Scenario 3c) and higher groundwater pumping (Scenario 3d). Figure 15 shows the results of Scenario 3a, including a zoomed-in depiction of the interface toe in the TLA aquifer.

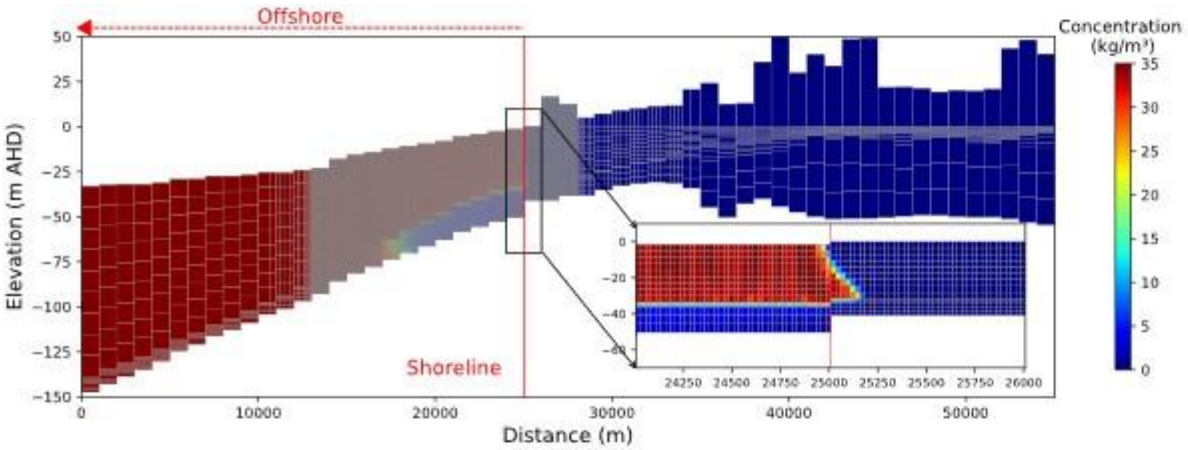

**Figure 15.** The salinity distribution arising from the steady-state simulation of future conditions at CSE, arising when pumping stresses in 2013 and the average recharge of 2004–2013 are applied for a prolonged (future) period of time.

Figure 15 shows that the interface is effectively unchanged after reaching a new steady-state condition under the pumping stresses of 2013. This result is expected, given that the heads in 2013 are similar to those of 1970, leading to similar salinity distributions under the pre-development steady-state condition (reflecting 1970 stresses) and Scenario 3a (reflecting 2013 stresses). In this scenario, the seawater toe shifts 129 m landward in the TCSA (relative to its position at the end of the transient simulation), compared to the 23 m landward movement of the seawater toe in the TLA. This difference is attributed primarily to the hydraulic conductivity values in the TLA and TCSA, whereby a higher hydraulic conductivity (~115 m/d) occurs near the coast in the TLA. In contrast, the TCSA, with a lower hydraulic conductivity of about 64 m/d near the coast, required longer to transition to a new steady state. Appendix M includes the results of Scenario 3a for the other cross sections.

***Scenario 3b:*** This scenario evaluates the effect of sea-level rise (the sea level is 0.3 m higher than the value of 0 m AHD used in Scenario 3a) on the steady-state distribution of groundwater salinities. Other stresses are adopted from Scenario 3a, including the inland boundary heads (and therefore, this reflects a head-controlled case of SWI arising from sea-level rise, using the classification of Werner and Simmons, 2009). Figure 16 shows the results of Scenario 3b. Appendix N includes the results of Scenario 3b for the other cross sections.

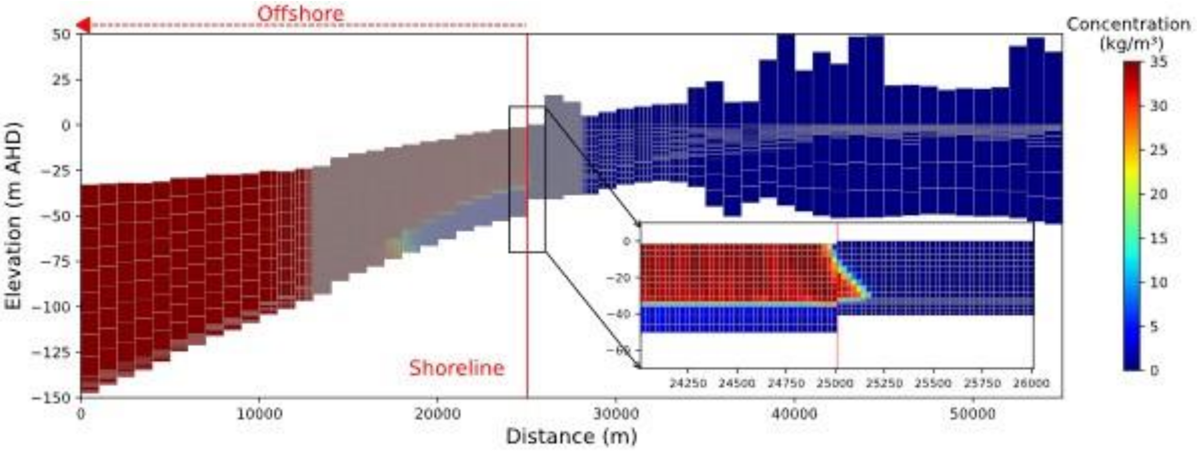

**Figure 16.** Steady-state distribution of salinity at CSE following sea-level rise of 300 mm occurring instantaneously in 2013.

The salinity distribution depicted in Figure 16 indicates that sea-level rise is unlikely to cause significant changes to the groundwater salinity in the coastal zone, although we have not assessed the potential for seawater to move further inland via surface pathways. That is, the shoreline is presumed to be unmoved due to sea-level rise. The result shown here that sea-level rise is largely inconsequent is due to the high groundwater heads at the inland boundary, such that a 0.3 m rise in sea level modifies the regional groundwater hydraulic gradient only slightly. The inland movement of the toe in the TLA due to sea-level rise is approximately 5 m, as determined by the 0.5 isochlor (50% relative salinity with respect to seawater salinity, which is assumed to be 35 kg/m$^3$). The model cells in the interface area are 25 m wide, and therefore, the toe location is found through linear interpolation.

***Scenario 3c:*** The impact of an 18% decline in recharge, caused by climate change, was assessed in this scenario. In this case, the inland boundary head fell relative to Scenario 3a because the recharge decline was applied to the regional model before extracting the stresses to apply to CSE for this scenario. Thus, the effects of the recharge drop are twofold; the inland head falls and the recharge over the cross section drops. Figure 17 shows the results of Scenario 3c. Appendix O includes the results of Scenario 3c for the other cross sections.

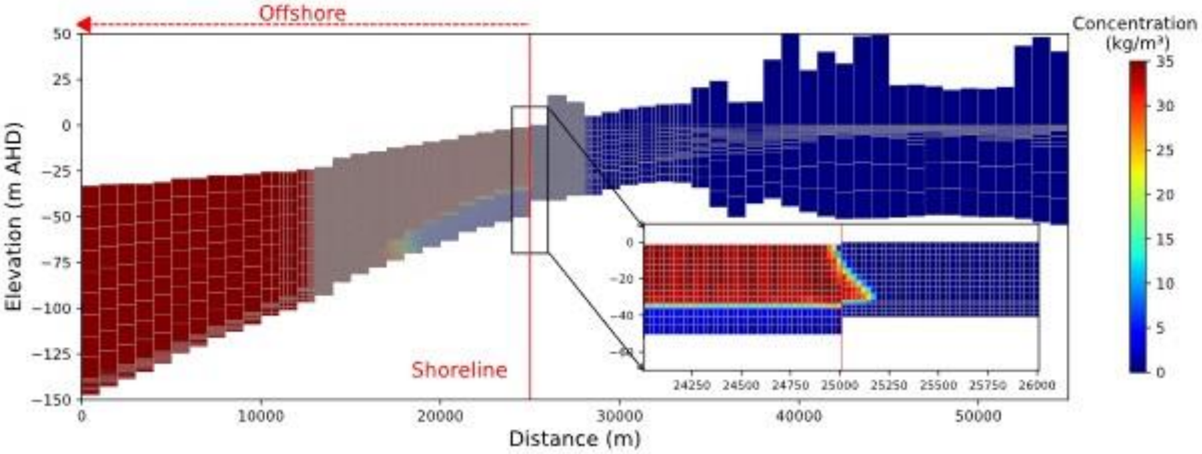

**Figure 17.** Steady-state distribution of salinity at CSE caused by a decline of 18% (relative to 2004–2013) in recharge.

Again, we see little impact (in Figure 17) on the salinity distribution from the imposed hydrologic changes to the groundwater system – in this case, an 18% drop in recharge. This is further evidenced by the slight relative inland movement of the toe in the TLA, approximately 4 m, compared to Scenario 3a.

***Scenario 3d:*** In this scenario, the pumping rate is increased by 71%, and the effect on the steady-state salinity distribution is assessed. Although there are no pumping wells that are intercepted by CSE (wells are located to the north and south of CSE, but not alongside it), the increased pumping will affect the regional heads, and therefore, the head at the inland boundary is expected to drop in this scenario. That is, the pumping increase was applied to all of the wells in the regional model prior to extracting the cross section. Figure 18 shows the results of Scenario 3d. Appendix P includes the results of Scenario 3d for the other cross sections.

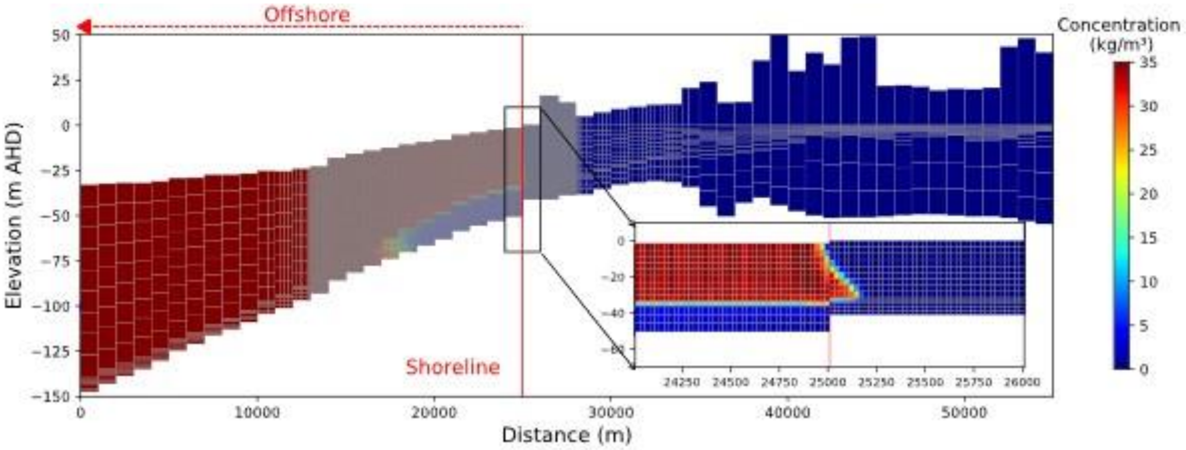

**Figure 18.** Steady-state distribution of salinity at CSE where the average pumping rate of 2013 was increased by 71%.

Consistent with the other two scenarios assessing seawater intrusion under future conditions, Figure 18 indicates minimal impact on the seawater extent when pumping is increased by 71%. A negligible toe movement of 1 m in the TLA caused by increased pumping is the least seawater intrusion that occurred within predictive scenarios, i.e., compared to the sea-level rise and reduced recharge simulations.

## 3.3 Summary of findings: Cross sections A to D

Tables 3 and 4 provide a summary of the results for Scenarios 1, 2, and 3, showing the distances of the interface (toe location) from the shoreline for CSA, CSB, CSC, CSD and CSE in the upper and lower aquifers. Table 3 presents the toe location distances for the upper aquifer, with negative values indicating onshore positions, whereas Table 4 shows the toe location distances for the lower aquifer, where positive values represent offshore positions.

**Table 3.** Toe location distances in the upper aquifer for CSA, CSB, CSC, CSD and CSE. Negative numbers indicate that the toe is onshore.

| | CSA | CSB | CSC | CSD | CSE |
|---|---|---|---|---|---|
| Scenario 1 | -3,181 m | -3,176 m | -2,401 m | -3,965 m | -124 m |
| Scenario 2 | -4,036 m | -4,281 m | -2,734 m | -4,171 m | -123 m |
| Scenario 3a | -4,207 m | -5,242 m | -2,802 m | -4,607 m | -146 m |
| Scenario 3b | -4,293 m | -5,406 m | -2,926 m | -4,998 m | -151 m |
| Scenario 3c | -4,959 m | -6,338 m | -2,992 m | -4,969 m | -150 m |
| Scenario 3d | -4,667 m | -5,714 m | -2,876 m | -4,729 m | -147 m |

**Table 4.** Toe location distances in the lower aquifer (TCSA) for CSA, CSB, CSC, CSD and CSE (where negative numbers represent the distance inland from the shoreline to the seawater wedge toe, and positive numbers indicate that the toe is offshore in the TCSA).

| | CSA | CSB | CSC | CSD | CSE |
|---|---|---|---|---|---|
| Scenario 1 | -9,344 m | 10,556 m | -5,129 m | -4,964 m | 7,018 m |
| Scenario 2 | -9,359 m | 10,543 m | -5,141 m | -4,965 m | 7,007 m |
| Scenario 3a | -14,250 m | 7,339 m | -5,473 m | -5,702 m | 6,878 m |
| Scenario 3b | -14,785 m | 6,870 m | -5,525 m | -6,092 m | 6,618 m |
| Scenario 3c | -17,841 m | 5,440 m | -5,844 m | -5,998 m | 6,681 m |
| Scenario 3d | -15,562 m | 6,428 m | -5,713 m | -5,835 m | 6,862 m |

**Cross Section A:** The modelling results for this cross section shows seawater in the landward part of the aquifer in both the upper and lower aquifers. This contrasts with CSE, in which the toe is around 7 km offshore. Recall that the toe is defined as the position of the 50% relative salinity contour (i.e., where the salinity is 50% of the seawater value, where seawater is assumed to be 35 kg/m$^3$) in the lowest model layer. Despite the onshore toe in the lower aquifer, there is considerable offshore freshwater in that aquifer, with the interface tip extending approximately 12 km offshore (see Figure H1). Freshwater discharge from the lower aquifer into the upper aquifer is also apparent (as unstable flow, as observed in the CSE results), causing freshwater-seawater mixing in the offshore part of the upper aquifer from upward leakage through the intervening aquitard.

The results of Scenario 2 indicate minimal seawater intrusion in the lower aquifer between 1970 and 2013 compared to pre-development conditions. This is reflected in a slight inland shift of the seawater toe by approximately 15 m (Scenario 1 versus Scenario 2; Table 4). This stability (in the seawater wedge) can be attributed to the low hydraulic conductivity of this layer (3 m/d). In contrast, the upper aquifer shows a noticeable increase in the seawater extent during the same 44-year period, with the seawater toe advancing approximately 855 m further inland (Scenario 1 versus Scenario 2; Table 3). This occurs because the modelled heads in the upper aquifer dropped by approximately 1 m at 5 km from the shoreline during 1970–2013, and the hydraulic conductivity of this layer has a high value (115 m/d).

Sea-level rise had only a small impact on the seawater extent in the upper aquifer, resulting in an inland toe shift of about 86 m (Scenario 3a versus Scenario 3b; Table 4). However, the lower aquifer appears more vulnerable to seawater intrusion under sea-level rise, with the seawater toe advancing approximately 535 m further inland (Scenario 3a versus Scenario 3b; Table 3). The reason for this difference is apparent in Figure B1 (Appendix B), showing the geometry of the CSA, whereby the lower aquifer is especially deep, and the base of the aquifer is mostly horizontal where the toe occurs, allowing it to more easily shift inland with the increased seawater head caused by sea-level rise. On the contrary, the upper aquifer has an upward sloping aquifer base near the coastline, acting as an impediment to seawater intrusion. Compared to the impacts observed under sea-level rise (Scenario 3b) and increased pumping (Scenario 3d), reduced recharge (Scenario 3c) had the most pronounced effect on seawater intrusion in both aquifers. It caused significant inland toe shifts of approximately 752 m in the upper aquifer (Scenario 3a versus Scenario 3c; Table 3) and 3,591 m in the lower aquifer (Scenario 3a versus Scenario 3c; Table 4).

Existing field measurements of groundwater salinity at wells near this location correspond to the TLA aquifer. The salinity distribution shows relatively fresh groundwater along this transect with EC values less than 2,000 µS/cm (Figure L1). These results are in agreement with the fresh groundwater that occurs at this location in the model, noting that a selection of the wells in this area are sufficiently deep (with the well bottom below mean sea level) to inform the extent of seawater in the aquifer, although none of the wells are installed to the base of the TLA, which would be necessary to observe shifts in the seawater toe.

A comparison between modelling results and the findings of a concurrent AEM survey is shown in Figure 19. The results indicate that a reasonable match between numerical model results and the AEM data was obtained in terms of the occurrence of the seawater wedge in the upper aquifer (TLA). Note that the AEM results can only be used to evaluate the occurrence of seawater in the upper aquifer (TLA) because the depth of the AEM survey for this cross section is shallower than the bottom of the TCSA.

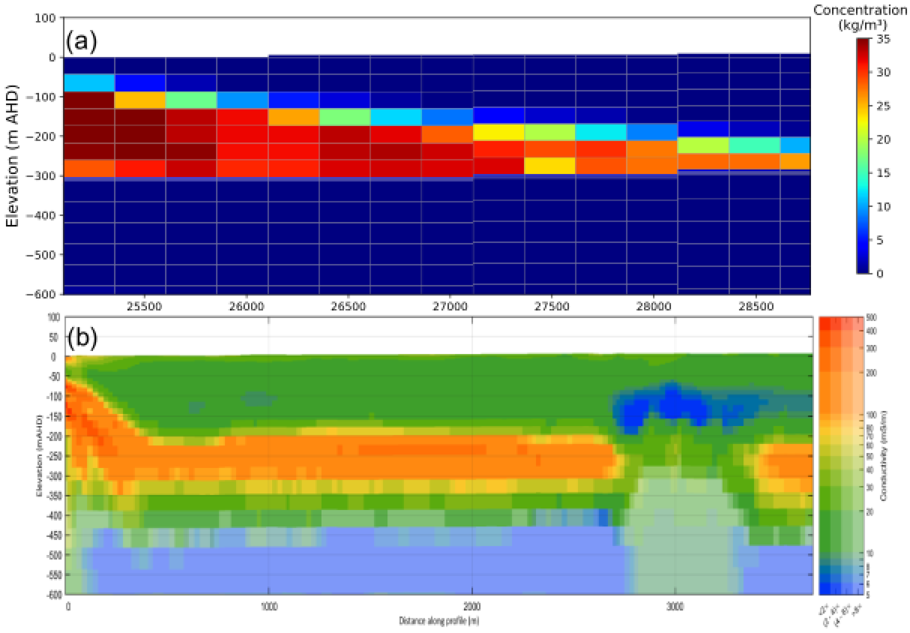

**Figure 19.** Comparison of numerical model and AEM (flight line 300121) results for cross section CSA. (a) Numerical model results derived from the salinity distribution at the end of the transient simulation (Figure J1); (b) interpretation of AEM survey derived from Davis et al. (2025a, 2025b). This figure is repeated in Appendix Q, in which the results for CSB are also shown.

**Cross Section B:** The model produced offshore fresh groundwater in the lower aquifer under pre-development conditions, with the seawater wedge tip occurring over 24 km from the shoreline (see Figure H2).24 In the model, the seawater wedge occurs at 3,176 m inland from the shoreline in the upper aquifer (TLA) under pre-development conditions. Evidence of fresh groundwater discharge from the lower aquifer into the upper aquifer is observed in the modelling results as patches of lower-salinity columns of water within the offshore zone of the upper aquifer that is otherwise filled with seawater.

The results of Scenario 2 indicate that significant seawater intrusion has occurred in the upper aquifer between 1970 and 2013, with the inland extent of the seawater wedge advancing by over 1 km (Scenario 1 versus Scenario 2; Table 3) since pre-development conditions. This occurs because the modelled heads in the upper aquifer dropped by approximately 1 m at 5 km from the shoreline during 1970–2013, and the hydraulic conductivity of this layer has a high value (115 m/d). In contrast, the simulation results of Scenario 2 exhibit limited seawater intrusion in the lower aquifer during the same 44-year period, with the seawater toe shifting landward by only 13 m (Scenario 1 versus Scenario 2; Table 4). The seawater wedge remained stable largely because the hydraulic conductivity of this layer has a low value (3 m/d).

Modelling results indicate that sea-level rise (Scenario 3b) presents the lowest risk of seawater intrusion compared with an 18% reduction in recharge (Scenario 3c) and a 71% increase in pumping (Scenario 3d). The toe shifts caused by sea-level rise (i.e., from one steady-state condition to another) were approximately 164 m inland in the upper aquifer (Scenario 3a versus Scenario 3b; Table 3) and 469 m landward in the lower aquifer (Scenario 3a versus Scenario 3b; Table 4). Simulation results indicate that reduced recharge (Scenario 3c) poses the highest risk (similar to CSA), leading to toe shift of approximately 1,096 m further inland in the upper aquifer, and a landward shift of 1,899 m in the lower aquifer.

Available groundwater salinity field measurements of the TLA near CSB indicate relatively fresh groundwater (including at depths below mean sea level), with most salinity values below 2,000 µS/cm (Figure L1). These field observations are consistent with the numerical modelling results, which produced relative concentration values close to zero near the above-mentioned well locations.

The comparison between the cross-sectional model outputs and the AEM survey data for CSB shows good alignment between the numerical model and AEM results in terms of the occurrence of the seawater wedge (Figure Q2). Similar to CSA, the AEM data is limited to assessing seawater occurrence in the upper aquifer (TLA), as the measurements do not extend below the base of the TCSA. Therefore, it is not possible to compare the AEM and numerical model predictions of the occurrence of seawater in the lower aquifer (TCSA).

**Cross Section C:** The modelling results from CSC indicate that seawater occurs at 2,401 m inland of the shoreline in the upper aquifer (TLA) and 5,129 m inland in the lower aquifer (TCSA) under pre-development conditions (see Figure H3), with some evidence of fresh groundwater discharge from the lower aquifer to the upper aquifer near the shoreline. The results of Scenario S1 (pre-development condition) indicate freshening of the offshore TCSA aquifer as a result of groundwater discharge, although significant mixing between waters of terrestrial and marine origins occurs causing mostly brackish water, rather than freshwater, in the offshore part of the lower aquifer. The interface tip is predicted to be approximately 3 km seaward in the TCSA.

The results indicate minimal seawater intrusion in the lower aquifer between 1970 and 2013, as reflected by a small inland toe shift of approximately 12 m (Scenario 1 versus Scenario 2; Table 4). The stability of the seawater wedge is due to the low hydraulic conductivity of the layer (3 m/d). No offshore fresh groundwater was predicted to occur at this location. In contrast, the seawater extent in the upper aquifer increased compared to pre-development conditions, with the toe advancing approximately 333 m further inland (Scenario 1 versus Scenario 2; Table 3). This occurs because the modelled heads in the upper aquifer dropped by approximately 0.5 m at 5 km from the shoreline during 1970–2013, and the hydraulic conductivity of this layer has a high value (115 m/d).

The simulation results indicate that sea-level rise had little impact on the seawater extent in the TCSA, with the toe shifting inland by approximately 52 m (Scenario 3a versus Scenario 3b; Table 4). The toe moved further in the upper aquifer, advancing about 124 m inland (Scenario 3a versus Scenario 3b; Table 3). Reduced recharge again caused the most seawater intrusion in both aquifers, resulting in inland toe shifts of approximately 190 m in the upper aquifer (Scenario 3a versus Scenario 3c; Table 3) and 371 m in the lower aquifer (Scenario 3a versus Scenario 3c; Table 4).

Shallow fresh groundwater (in the TLA) has been confirmed by salinity field measurements (in bores constructed below mean sea level) near CSC, with values below 2,000 µS/cm (Figure L2) but also, some wells showing elevated salinities that are more likely associated with terrestrial rather than marine sources of saltwater. These measurements align with the numerical model, which also predicts shallow fresh groundwater in CSC.

**Cross Section D:** Results for the pre-development simulation (Scenario 1) of CSD indicate the presence of an onshore seawater wedge in both the upper and lower aquifers, with the landward extent of seawater being larger in the lower aquifer (see Figure H4). Notably, no offshore fresh groundwater is observed in this location, likely due to the relatively low hydraulic heads - approximately 4 m AHD in the lower aquifer in 2013 at an inland distance of 6 km (Figures I4 and K4).

During the transient simulation (1970–2013), the seawater wedge was relative stable in the lower aquifer due to the low value of hydraulic conductivity (3 m/d). Conversely, the seawater toe in the upper aquifer (TLA) shifted approximately 206 m further inland during the 44-year simulation period (Scenario 1 versus Scenario 2; Table 3). This occurs because the modelled heads in the upper aquifer dropped by approximately 0.5 m at 5 km from the shoreline during 1970–2013, and the hydraulic conductivity of this layer has a high value (115 m/d).

Future seawater intrusion scenarios suggest that sea-level rise (Scenario 3b) is likely to have a greater impact on the extent of the seawater wedge in both aquifers (at CSD) compared to the other scenarios (i.e., recharge decline and increased pumping). The inland toe shifts were approximately 391 m in the upper aquifer and 390 m in the lower aquifer under sea-level rise scenarios (Scenario 3a versus Scenario 3b; Tables 3 and 4). The simulation results show that compared to other scenarios (i.e., sea-level rise and recharge decline), a 71% increase in pumping (Scenario 3d) had the least impact in terms of the advancement of seawater in both the upper and lower aquifers (Scenario 3a versus Scenario 3d; Tables 3 and 4).

Figure L3 shows that field measurements of coastal groundwater in the TLA (near CSD) is relatively fresh, with salinity measurements mostly below 2,000 µS/cm. This is consistent with the predicted of the numerical model of CSD.

# 4 Discussion

This study has sought to improve the current understanding of the spatial extent of seawater within Limestone Coast aquifers. The analysis of five representative cross sections revealed significant variability of the extent and threat of seawater intrusion across the region. The main factors causing this variability are spatial differences in the hydraulic head and in predictions of head changes occurring over time (or between steady-state scenarios), and variability in aquifer hydraulic properties (e.g., hydraulic conductivity, aquifer thickness) between cross sections. The results indicate a somewhat consistent seawater penetration in the TLA, at least in CSA, CSB and CSD, with the inland toe wedge located ~4 km from the coast. In contrast, the toe location in the TLA at CSC is predicted to be about 2 km inland, while the most northern cross section, CSE, shows an inland seawater extent of just 123 m from the coast. These results build on the prior study of Mustafa et al. (2012), who identified the presence of seawater in Limestone Coast aquifers through water chemistry analysis. They encountered seawater up to 1.5 km from the coast in certain TLA units. Given the limited number of wells that penetrate to the base of the TLA, it is unlikely that Mustafa et al. (2012) had sufficient monitoring well coverage to discover the landward limit of seawater (as indicated by the toe position in our modelling results) in Limestone Coast aquifers. The current work also adds to the study by DEW (2023), which examined Limestone Coast coastal aquifers encompassing CSA and CSB in this study. Their results suggest a toe location of about 2 km inland in the vicinity of CSA and CSB, although they acknowledged that the simplified approach that was used to simulate the freshwater-seawater interface (with the SWI2 package) likely impacted their estimates of the seawater extent.

The comparison of groundwater heads between the cross-sectional model with offshore extension (where only freshwater is simulated) and the parent model shows a slightly difference. As there are few field measurements of heads near the coast to allow an assessment of which of the models (cross-sectional models or parent models) has produced a more accurate representation of the coastal boundary, it is presently unclear whether the more physically based coastal simulation undertaken in our study (relative to Morgan et al. (2015)) has provided a more reliable prediction of coastal groundwater heads than the parent model. Given the link between heads and salinities in coastal aquifer theory, the comparison between AEM-based estimates of the seawater extent (see Figures 19 to Q2) offers useful insight into the reliability of cross-sectional modelling outputs (as a direct comparison to salinity and an indirect assessment of heads), even if it is difficult to check the heads near the coast directly.

The modelling results support the potential occurrence of offshore fresh groundwater in the TCSA, particularly at CSA, CSB and CSE, as discussed by Lamontagne et al. (2015) and Morgan et al. (2015). This is consistent with the analysis of Knight et al. (2019), who found brackish groundwater up to 13.2 km offshore in the TCSA. Their analysis was based on a combination of offshore geophysical data and analytical modelling.

SWI in the TLA was assessed for the 44 year-period of simulation (1970 – 2013). Modelling results indicate inland shifts of the seawater wedge of about 1 km in CSA and CSB, and less severe SWI in the other cross sections, including almost no SWI at CSE. This difference in the SWI that occurred in the various cross sections arises because there is significantly more pumping and greater long-term drawdown in the southern part of the study area, where CSA and CSB are located. In contrast, the northern cross section (CSE) has little or no pumping, resulting in more stable groundwater levels and less SWI over time. These results add to the analysis of DEW (2023), who refrained from reporting on SWI modelling outcomes due to uncertainties associated with the SWI2 package. Furthermore, DEW (2023) did not assess the potential effects of future climate change or other scenarios on the seawater extent, highlighting a critical gap addressed in this study.

The karst nature of the Limestone Coast is undoubtedly an important control on seawater intrusion, and yet, the current study neglects karst conduits and fractures, and adopts the hydraulic properties of the regional model of Morgan et al. (2015). Where pumping occurs in the vicinity of conduits, we expect seawater to be drawn preferentially inland through those pathways. This process is not considered in the model, partly because it is unclear where karst conduits occur, but also, there are very few measurements in the coastal fringe that would assist in assessing the model’s goodness of fit as a resolution that could capture karst features. The AEM survey may provide observations of salinity (and geological) structure in the coastal aquifer at a multitude of sites, which would allow for additional modelling scenarios that incorporate alternative parameter distributions to reflect potential karst feature locations. Further research effort is also warranted to compare the results of the dispersive modelling undertaken in this study with the analysis of DEW (2023), in which the seawater intrusion (SWI) package of MODFLOW was used to obtain an approximate, regional-scale evaluation of the seawater extent in the aquifer. The SWI2 package adopts a sharp interface, and therefore, probably over-estimates the seawater extent according to prior studies comparing dispersive and sharp-interface models (e.g., Pool and Carrera, 2011; Werner, 2017b).

The match between numerical model results and the interpretations of the AEM survey, applicable to the TLA in terms of the occurrence of the seawater wedge, was found to be reasonable for CSA and CSB, where cross-sectional models were constructed within the AEM survey area. Differences between the two, independent forms of seawater extent analysis are attributable to a host of possible causes that influence the accuracy of two methods in deciphering the occurrence of the seawater wedge. For example, the cross-sectional models rely on homogenised representations of the TLA, TCSA, and the intervening aquitard, and yet, heterogeneities may play an important role in modifying the seawater extent, as discussed above. The salinity distributions extracted from the AEM survey will reflect the effects of heterogeneities; however, the AEM readings are themselves influenced by heterogeneities because the sediment properties influence the electrical conductance and the magnetic response an electromagnetic disturbance (Ball et al., 2020). As such, geological features (e.g., karst conduits) may be indistinguishable from salinity variability, albeit salinity and geological variability affect the subsurface electromagnetic signals by different amounts. Environmental conditions, such as electromagnetic noise from infrastructure or temperature variations during the survey, can also affect data quality (Kang et al., 2021). The depth limitations of AEM further limit the comparison between AEM results and the numerical model.

# 5 Conclusions

This report aimed to evaluate the extent of seawater intrusion in the coastal aquifers of the Limestone Coast and assess the risks associated with current and future groundwater stresses by simulating five representative cross sections perpendicular to the coast (CSA to CSE). This work was conducted as part of Task 4 (Seawater Intrusion Risk) of the Goyder Project: Adaptation of the South-Eastern Drainage System under a Changing Climate. Additionally, a key objective of this study was to develop a methodology for extracting seawater intrusion (SWI) models from existing regional groundwater flow models. This methodology is intended to facilitate future assessments of SWI across a broader range of locations within the study area. The main findings of this project are summarised as:

1. Steady-state numerical simulations predict an inland seawater wedge in the Tertiary Limestone Aquifer (TLA) as reflected in the numerical simulations of cross-sections CSA to CSE, whereas a seawater wedge that is inland of the coast in the lower Tertiary Confined Sand Aquifer (TCSA) was only obtained at three cross-section locations: CSA, CSC and CSD.
2. Transient simulations for the period 1970–2013 predict that SWI in the TLA during that time was generally less in the north (e.g., CSE) than in the south (e.g., CSA). An exception is CSB, in which a large SWI movement during 1970–2013 is simulated, with an inland shift of the seawater wedge toe exceeding 1 km.
3. The results indicate that SWI in the TCSA during 1970–2013 has been less than SWI in the TLA, with the maximum inland shift in the seawater wedge toe of only 15 m in the TCSA, which occurred in the model of CSA.
4. Simulations under sea-level rise scenarios underscore the variability of the accompanying SWI in both the TLA and TCSA across the Limestone Coast. SWI in the TLA (from sea-level rise) was largest at CSD (391 m), while CSA, CSB, and CSC exhibit moderate landward advances in the TLA (86 m, 164 m, and 124 m, respectively), and CSE showed minimal SWI (~5 m) in the TLA due to sea-level rise. Sea-level rise is expected to cause greater SWI in the TCSA. Inland and landward movements of the wedge toe were generally larger in the south, from 535 m at CSA down to 52 m at CSC, with intermediate values at CSB (469 m), CSD (390 m), and CSE (260 m).
5. Recharge-reduction simulations caused larger SWI than that resulting from sea-level rise or the transient historical period (1970–2013). In the TLA, CSB experienced the greatest toe movement (1,096 m), followed by CSA (752 m), CSD (362 m) and CSC (190 m), while CSE underwent only minor toe displacement from a reduction in recharge. In the TCSA, a reduction in recharge caused SWI that was as much as an order of magnitude larger than the predicted SWI in the TLA. That is, the toe moved 3,591 m at CSA, 1,899 m at CSB, 371 m at CSC, 296 m at CSD, and 197 m at CSE in the TCSA due to the imposition of an 18% recharge reduction.
6. Pumping-increase simulations revealed SWI that was larger than the SWI that was predicted to have occurred during 1970–2013. The maximum toe shift in the TLA occurred at CSB (472 m) and CSA (460 m), with CSD (122 m) and CSC (74 m) showing smaller toe advances, and CSE again negligible. In the TCSA, increased pumping led to the toe of the wedge moving 1,312 m at CSA, 911 m at CSB, 240 m at CSC, 133 m at CSD, and moved minimally at CSE.
7. A reasonable match between numerical model results and AEM data for the TLA in cross sections CSA and CSB (see Figures 19 and Q2) indicates that the models appear to have simulated the occurrence of the seawater wedge with a reasonable level of reliability, albeit direct measurements of the freshwater-seawater interface are needed to confirm the modelling predictions of seawater extent. The depth limitations of AEM data prevent a comparison with numerical model estimates of the seawater wedge in the TCSA, for which there are also very few monitoring sites that can be used to aid in validating the numerical models.
8. The proposed methodology in this study for extracting cross-sectional models from the regional model was validated by inter-model comparisons, as evidenced by the closeness of hydrographs and the adequately low bias observed when comparing the results of both models.

# 6 Recommendations

There are several shortcomings in the existing dataset where opportunities exist to update the existing models so that more realistic depictions of seawater intrusion can be simulated. For example, heterogeneity within the stratigraphic units likely plays a key role in the movement of seawater in the coastal aquifer. Geological modelling is warranted to produce stochastic realisations of the geology of the Limestone Coast, similar to other efforts to do this where groundwater transport depends on strong contrasts in sediment hydraulic properties (e.g., Schiavo, 2023; Li et al., 2022). This approach will allow for the assessment of geological uncertainty and its effect on the extent of seawater intrusion, and will no doubt provide opportunities to better understand coastal wetland-aquifer-ocean interactions, amongst a host of other relevant groundwater-related knowledge gaps (e.g., the estimation of submarine groundwater discharge, nutrient transport, etc.).

Given that we have relied upon the model of Morgan et al. (2015) in developing SWI models (because it better represents the regional stratigraphy compared to more recent studies), there is a need to update that model with more recent pumping and recharge values. This is notwithstanding recommendations by Morgan et al. (2015) for a suite of other improvements to their regional model. Additionally, a thorough evaluation of groundwater quality data is necessary, including assessing where saline groundwater is associated with terrestrial processes or seawater intrusion, and considering saline groundwater from non-marine sources. Also, the current representation of the drainage network is quite rudimentary and would benefit from being updated, particularly in terms of where fresh or saline groundwater enters the drains. Moreover, it is necessary to better capture the variation in topography due to its significant influence on modelled groundwater evapotranspiration, and the substantial impact of evapotranspiration on the water balance. Finally, the model's representation of wetlands, especially those along the coast, is rather simple and should be improved to better capture links between wetland hydrology and coastal groundwater movements.

# References

Anderson, M.P., Woessner, W.W., and Hunt, R.J., 2015. Applied groundwater modeling: Simulation of flow and advective transport, 2nd ed. Academic Press, London. 630 p. https://doi.org/10.1016/C2009-0-21563-7

Bakker, M., Schaars, F., Hughes, J.D., Langevin, C.D., and Dausman, A.M., 2013. Documentation of the seawater intrusion (SWI2) package for MODFLOW: U.S. Geological Survey Techniques and Methods, book 6, chap. A46, 47 p. http://pubs.usgs.gov/tm/6a46/

Ball, L.B., Davis, T.A., Minsley, B.J., Gillespie, J.M., and Landon, M.K., 2020. Probabilistic categorical groundwater salinity mapping from airborne electromagnetic data adjacent to California's Lost Hills and Belridge oil fields. Water Resources Research, 56(6), e2019WR026273. https://doi.org/10.1029/2019WR026273

Brookes, J., 2010. Introduction. In: Brookes J. Ed., South East Water Science Review, Lower Limestone Coast Water Allocation Plan Taskforce, Adelaide.

Cooper, H.Jr., 1964. A hypothesis concerning the dynamic balance of fresh water and salt water in a coastal aquifer. Sea water in coastal aquifers. Relation of salt water to fresh ground water. Geological Survey Water-Supply Paper 1613-C. Washington, USA, 95 p. https://pubs.usgs.gov/wsp/1613c/report.pdf (Accessed on 18 November 2024).

DEW, 2022. Guide to climate projections for risk assessment and planning in South Australia 2022. Government of South Australia, through the Department for Environment and Water, Adelaide, p 85. https://data.environment.sa.gov.au/Content/Publications/Guide%20to%20climate%20projections%20for%20risk%20assessment%20and%20planning%20in%20South%20Australia%202022.pdf (Accessed on 18 November 2024).

DEW, 2023. Lower Limestone Coast subregional model: coastal areas south of Mount Gambier, DEW Technical report 2023/81, Government of South Australia, Department for Environment and Water, Adelaide. https://www.waterconnect.sa.gov.au/Content/Publications/DEW/DEW_TR_2023_81.pdf (Accessed on 8 April 2025).

Davis, A., Munday, T.J., and Ibrahimi, T., 2025a. Adaptation of the South-Eastern drainage system under a changing climate - Limestone Coast Airborne Electromagnetic Survey: Acquisition, Processing and Modelling. Goyder Institute for Water Research Technical Report Series No. 25/5.1.

Davis, A., Munday, T.J., and Ibrahimi, T., 2025b. Adaptation of the South-Eastern drainage system under a changing climate - Limestone Coast Airborne Electromagnetic Survey: Conductivity-Depth Sections. Goyder Institute for Water Research Technical Report Series No. 25/5.2.

Gibbs, M.S., Maier, H.R., and Dandy, G.C., 2012. Development of decision support frameworks for water resources management in the south east, Goyder Institute for Water Research Technical Report Series No. 12/3, 99 p. https://goyderinstitute.org/wp-content/uploads/2023/04/goyder_trs_12-3_development_of_decision_support_frameworks-1.pdf (Accessed on 18 November 2024).

Green, G., Gibbs, M., Alcoe, D., and Wood, C., 2012. Impacts of Climate Change on Water Resources Phase 3 Volume 2 Eyre Peninsula Natural Resources Management Region, DFW Technical Report 2012/04, Government of South Australia, Department for Water, Adelaide. https://www.waterconnect.sa.gov.au/Content/Publications/DEW/DFW_TR_2012_04_WEB.pdf (Accessed on 8 April 2025).

Kang, S., Dewar, N., and Knight, R., 2021. The effect of power lines on time-domain airborne electromagnetic data. Geophysics, 86(2), E123-E141. https://doi.org/10.1190/geo2020-0089.1

King, H.J., and Dodds, A.R., 2002. Geophysical investigation of salt water invasion of freshwater aquifers in the Port MacDonnell area of South Australia. South Australia. Department of Water, Land and Biodiversity Conservation. Report, DWLBC 2002/21.

Knight, A.C., Werner, A.D., and Irvine, D.J., 2019. Combined geophysical and analytical methods to estimate offshore freshwater extent. Journal of Hydrology, 576, 529–540. https://doi.org/10.1016/j.jhydrol.2019.06.059

Lamontagne, S., Taylor, A.R., Herpich, D., and Hancock, G.J., 2015. Submarine groundwater discharge from the South Australian Limestone Coast region estimated using radium and salinity. Journal of Environmental Radioactivity, 140, 30-41. https://doi.org/10.1016/j.jenvrad.2014.10.013

Lee, J., Rolle, M., and Kitanidis, P.K., 2018. Longitudinal dispersion coefficients for numerical modeling of groundwater solute transport in heterogeneous formations. Journal of Contaminant Hydrology, 212, 41-54. https://doi.org/10.1016/j.jconhyd.2017.09.004

Li, H., Lu, C., Werner, A.D., Irvine, D.J., and Luo, J., 2022. Impacts of heterogeneity on aquifer storage and recovery in saline aquifers. Water Resources Research, 58(5), e2021WR031306. https://doi.org/10.1029/2021WR031306

Morgan, L.K., Harrington, N., Werner, A.D., Hutson, J.L., Woods, J., Knowling, M.J., 2015. South East regional water balance project–Phase 2. Development of a regional groundwater flow model. Technical Report Series No. 15/38, 142 p. https://goyderinstitute.org/wp-content/uploads/2023/06/goyder_trs_15-38_south_east_regional_water_balance_phase_2.pdf (Accessed November 04, 2024).

Morgan, L., Werner, A.D., and Patterson, A.E, 2018. A conceptual study of offshore fresh groundwater behaviour in the Perth Basin (Australia): Modern salinity trends in a prehistoric context. Journal of Hydrology: Regional Studies, 19, 318-334. https://doi.org/10.1016/j.ejrh.2018.10.002

Mustafa, S., Slater, S., and Barnett, S., 2012. Preliminary investigation of seawater intrusion into a freshwater coastal aquifer – Lower South East, Department of Environment, Water and Natural Resources, Technical Report DEWNR 2012/01, Adelaide, South Australia. https://www.waterconnect.sa.gov.au/Content/Publications/DEW/DEWNR_TR_2012_01.pdf (Accessed on 8 April 2025).

Pool, M., and Carrera, J., 2011. A correction factor to account for mixing in Ghyben-Herzberg and critical pumping rate approximations of seawater intrusion in coastal aquifers. Water Resources Research, 47(5), Art. no. W05506. https://doi.org/10.1029/2010WR010256

Schiavo, M., 2023. The role of different sources of uncertainty on the stochastic quantification of subsurface discharges in heterogeneous aquifers. Journal of Hydrology, 617, 128930. https://doi.org/10.1016/j.jhydrol.2022.128930

Solórzano-Rivas, S.C., and Werner, A.D., 2018. On the representation of subsea aquitards in models of offshore fresh groundwater. Advances in Water Resources, 112, 283-294. https://doi.org/10.1016/j.advwatres.2017.11.025

Solórzano-Rivas, S.C., Werner, A.D., and Irvine, D.J., 2021. Mixed-convective processes within seafloor sediments arising from fresh groundwater discharge. Frontiers in Environmental Science, 9, p. 600955. https://doi.org/10.3389/fenvs.2021.600955

URPS, 2015. Climate Limestone Coast regional adaptation plan project. Climate Projections Report. https://www.lclga.sa.gov.au/application/files/9415/4987/8891/Regional_Climate_Change_Adaptation_Plan.pdf (Accessed on 8 April 2025).

Werner, A.D., 2017a. On the classification of seawater intrusion. Journal of Hydrology, 551, 619-631. https://doi.org/10.1016/j.jhydrol.2016.12.012

Werner, A.D., 2017b. Correction factor to account for dispersion in sharp-interface models of terrestrial freshwater lenses and active seawater intrusion. Advances in water resources, 102, 45-52. https://doi.org/10.1016/j.advwatres.2017.02.001

Werner, A.D., Bakker, M., Post, V.E., Vandenbohede, A., Lu, C., Ataie-Ashtiani, B., Simmons, C.T., and Barry, D.A., 2013. Seawater intrusion processes, investigation and management: Recent advances and future challenges. Advances in Water Resources, 51, 3-26. https://doi.org/10.1016/j.advwatres.2012.03.004

Werner, A.D., and Simmons, C.T., 2009. Impact of sea-level rise on sea water intrusion in coastal aquifers. Groundwater, 47, 197–204. https://doi.org/10.1111/j.1745-6584.2008.00535.x

Zech, A., Attinger, S., Bellin, A., Cvetkovic, V., Dietrich, P., Fiori, A., Teutsch, G., and Dagan, G., 2019. A critical analysis of transverse dispersivity field data. Groundwater, 57, 632-639. https://doi.org/10.1111/gwat.12838

Zheng, C., and Bennett, G.D., 2002. Applied contaminant transport modeling. 2nd ed. John Wiley and Sons, Inc., New York.

# Appendix A – Development of cross-sectional models

This section outlines the procedure for extracting a cross section from a rectilinear 3D groundwater model. The methodology described below is adapted from Gholami et al. (2025), published in *Groundwater*. Except where stated, text, equations, and procedures follow that work. Portions are reproduced verbatim under the Creative Commons Attribution (CC BY) license (© 2025 The Authors). The cross sections were obtained from a 3D MODFLOW model of the Lower Limestone Coast (Australia) (Morgan et al., 2015) that simulates transient stresses for the period 1970 to 2013. The approach involves the translation of the following model components from the 3D model to the cross-sectional model: (1) model grid, (2) aquifer hydraulic properties, (3) initial and specified heads, and the distribution of active and inactive cells, (4) flux-based stresses (recharge and pumping), and (5) head-dependent stresses (evapotranspiration and drains). The workflow was developed using FloPy, a Python package for creating, running and post-processing MODFLOW-based models (Hughes et al., 2024; Leaf and Fienen, 2022).

The methodology for transferring each of the above-mentioned model components is described below. These were combined to extract ten cross sections (from the 3D regional model) that were subsequently run to compare with the heads of the parent model. Figure A1 shows the location of these cross sections and the outline of the 3D model, which was created by Morgan et al. (2015). Cross sections were selected to avoid disconnected regions of the 3D model domain (e.g., as would occur if a north-south cross section was adopted at an easting of 530,000 m). The cross sections represented a mixture of alignments relative to the groundwater flow direction, with several being strongly oblique to the head contours and/or crossing areas showing complex head patterns (e.g., see cross section AA′).

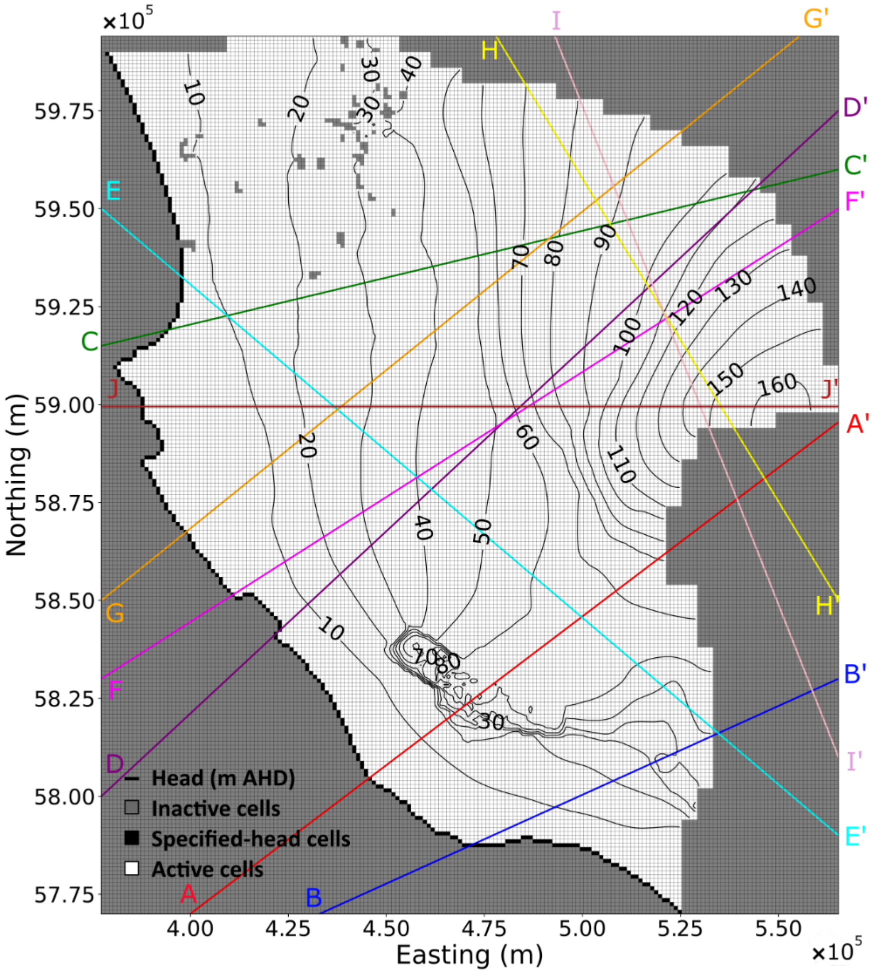

**Figure A1.** Locations of cross sections through the 3D model of the Lower Limestone Coast (Morgan et al., 2015). Contours of head from layer 1 and at the end of the first stress period (10 days of the 16,081-day simulation) are shown. AHD refers to the Australian Height Datum. Reproduced from Gholami, A., Jazayeri, A., and Werner, A.D., 2025. Cross-Sectional Models of Groundwater Flow: Review and Correction for Transverse Flow. Groundwater, 63(5), 752–763. https://doi.org/10.1111/gwat.70017. Licensed under CC-BY.

## A.1. Model grid

The usual practice of selecting the alignment of a cross-sectional model (presumed to have a straight-line axis in the current study) is to intersect head contours at right angles. This is difficult in the case of transient, real-world simulations because cross sections have a stationary position while head contours invariably shift in time. Nevertheless, lateral flow (i.e., perpendicular to the axis of the cross section) is minimized using this approach. Usually, the resulting cross sections are oblique to the 3D model grid. A cross section passing through a rectilinear grid at an oblique angle will intersect non-uniform portions of 3D cells. This may create irregular cell sizes in the 2D model if the intersected 3D cells are each represented individually in the 2D model, leading to numerical challenges if adjacent cells have contrasting dimensions. Figure A2 shows how the cells of a cross-sectional model will have varying lengths when aligned obliquely with a simple grid.

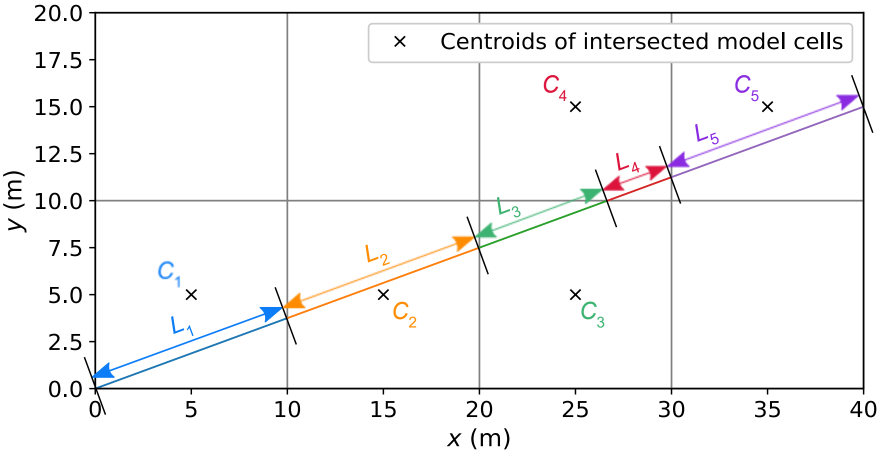

**Figure A2.** Plan view of a cross-sectional model extracted obliquely from a 3D model with a grid consisting of 2 rows (in the *y*-direction) and 4 columns (in the *x*-direction), where $L_1$ to $L_5$ are the lengths of cross-sectional model cells obtained from the intersection of 3D model cells $C_1$ to $C_5$, respectively. Reproduced from Gholami, A., Jazayeri, A., and Werner, A.D., 2025. Cross-Sectional Models of Groundwater Flow: Review and Correction for Transverse Flow. Groundwater, 63(5), 752–763. https://doi.org/10.1111/gwat.70017. Licensed under CC-BY.

The technique adopted in the current study for extracting the intersected lengths of 3D model cells, shown in Figure A2, involved the *GridIntersect* class in the FloPy package (Hughes et al., 2024). Initially, non-uniform 2D cell lengths were adopted, whereby lengths $L_1$, $L_2$ and $L_5$ are equal, while $L_3$ and $L_4$ differed (but sum to $L_1$). Non-uniform cell lengths with ratios of neighbouring cells that exceed recommended limits potentially create numerical errors. For example, Anderson et al. (2015) recommend restricting the expansion of cell lengths to a factor of 1.5. To avoid this issue, cells in the 2D model were merged so that the cell interval of the 3D model was effectively preserved, notwithstanding that the intersection length of an oblique cross-sectional grid exceeds the rectilinear cell dimensions of the 3D model (i.e., in Figure A2, $L_2$ exceeds the dimensions of cell $C_2$ according to Pythagoras). Thus, the length of each cross-sectional cell was set to $L_c$ [L], given by:

$$L_c = \begin{cases} \sqrt{(\Delta x)^2 + (s\Delta x)^2} & \text{if } s \le 1 \\ \sqrt{(\Delta y)^2 + (\dfrac{\Delta y}{s})^2} & \text{if } s > 1 \end{cases} \tag{1}$$

where *s* [-] represents the slope of the cross-section axis relative to the rectilinear grid, $\Delta x$ [L] is the width of a column in the 3D model, and $\Delta y$ [L] is the width of a row in the 3D model. Here, the method is described for uniform cell sizes in the 3D model. The approach for a 3D grid of variable cell sizes requires simple adjustments to the methodology. In Figure A2, *s* is $\sqrt{(L_1^2 - 10^2)} \big/ 10$, where the 3D model column width is a uniform 10 m. The unavoidable aggregation of 3D cells in building the 2D model grid led to the need for appropriate averaging methods for transferring 3D model properties (hydraulic parameters, boundary conditions, stresses, etc.) to the 2D model, as discussed in the next subsection.

For cross-sectional models aligned to the orientation of a 3D rectilinear model, 2D cells can directly adopt the top and bottom elevations of 3D model cells. This is also the case for the cells of oblique cross-sectional models where the cross section passes through the entire width of a 3D cell (e.g., $C_1$, $C_2$ and $C_5$; Figure A2) and thus merging of 3D cells is not required. For 2D cells resulting from the merger of two 3D cells, the cell top and bottom elevations were determined using distance-weighted averaging, as:

$$P_m = \frac{P_i L_i + P_{i+1} L_{i+1}}{L_i + L_{i+1}} \tag{2}$$

where $L_i$ [L] and $L_{i+1}$ [L] are the intersection lengths (e.g., $L_3$ and $L_4$ in Figure A2) of two neighbouring 3D cells that were merged in the 2D model, $P_i$ and $P_{i+1}$ are the model properties values linked to these cells (e.g., the top or bottom elevations of model cells), and $P_\mathrm{m}$ is the property assigned to the merged cell in the 2D model.

## A.2. Aquifer hydraulic properties

Where 2D model cells do not represent the merger of two 3D model cells, aquifer properties in the 2D model, such as the horizontal hydraulic conductivity ($K_\mathrm{h}$ [LT$^{-1}$]), the vertical hydraulic conductivity ($K_\mathrm{v}$ [LT$^{-1}$]), specific storage ($S_\mathrm{s}$ [L$^{-1}$]) and specific yield ($S_\mathrm{y}$ [-]), were taken directly from the 3D model. For merged 2D cells, Eq. (2) was used to calculate the cross-sectional values of $K_\mathrm{v}$, $S_\mathrm{s}$ and $S_\mathrm{y}$. Averaging of the $K_\mathrm{h}$ for merged cells took into consideration the method used to average $K_\mathrm{h}$ between adjacent cells in MODFLOW, namely the harmonic mean, treating the neighbouring cells as porous media that are connected in series (Langevin et al., 2017). This led to the following averaging formula:

$$K_{\mathrm{h,m}} = \frac{L_i + L_{i+1}}{\left(\dfrac{L_i}{K_{\mathrm{h},i}}\right) + \left(\dfrac{L_{i+1}}{K_{\mathrm{h},i+1}}\right)} \tag{3}$$

where $L_i$ and $L_{i+1}$ are the lengths of two neighbouring 3D cells that were merged in the 2D model, $K_{\mathrm{h},i}$ [LT$^{-1}$] and $K_{\mathrm{h},i+1}$ [LT$^{-1}$] are the horizontal hydraulic conductivities of the corresponding cells, and $K_\mathrm{h,m}$ [LT$^{-1}$] is the horizontal hydraulic conductivity of the merged cell in the 2D model.

## A.3. Initial heads, specified heads and active/inactive conditions

Initial heads, specified-head boundary conditions and active/inactive cell conditions for 2D model cells that are not the combination of two 3D model cells were the same as the 3D model. Here, “inactive” refers to no-flow cells that are omitted from MODFLOW calculations of head and flux, while “active” refers to cells that are included in the simulation (but are not fixed using a specified-head condition). Table A1 provides the method for assigning initial heads to the 2D model for merged cells. Table A1 also describes the rules for setting the conditions (active, inactive or specified head) of merged cells in the 2D model.

**Table A1.** Strategies for specifying the active (i.e., head is not specified by the user), inactive (i.e., cells that are excluded from MODFLOW calculations), or specified-head conditions of merged cells in the 2D model. $C_i$ and $C_{i+1}$ are the neighbouring 3D cells involved in the creation of the merged cell ($C_\mathrm{m}$) in the 2D model. The methods for determining initial and/or specified heads in the 2D model are also listed. Reproduced from Gholami, A., Jazayeri, A., and Werner, A.D., 2025. Cross-Sectional Models of Groundwater Flow: Review and Correction for Transverse Flow. Groundwater, 63(5), 752–763. https://doi.org/10.1111/gwat.70017. Licensed under CC-BY.

| Case | $C_i$ | $C_{i+1}$ | $C_\mathrm{m}$ | Calculation of initial and/or specified heads in the 2D model |
|---|---|---|---|---|
| 1 | Active | Active | Active | Eq. (2) |
| 2 | Inactive | Inactive | Inactive | Not required |
| 3 | Active | Specified head | Specified head | $C_{i+1}$ |
| 4 | Inactive | Active | Active | $C_{i+1}$ |
| 5 | Inactive | Specified head | Specified head | $C_{i+1}$ |
| 6 | Specified head | Active | Specified head | $C_i$ |
| 7 | Specified head | Specified head | Specified head | Eq. (2) |
| 8 | Active | Inactive | Active | $C_i$ |
| 9 | Specified head | Inactive | Specified head | $C_i$ |

## A.4. Aquifer stresses (pumping wells, recharge, evapotranspiration and drains)

2D cells that translate directly from the 3D model (i.e., cell amalgamation was not needed) adopted the same well pumping and recharge fluxes. For merged cells, pumping and recharge fluxes were obtained using Eq. (2), as were evapotranspiration parameters (surface elevation, maximum evapotranspiration flux, extinction depth) and the conductance of drain cells. The assignment of drain elevations ($z_\mathrm{d}$ [L]) to the 2D model adopted the methods outlined in Table A2.

**Table A2.** Method for determining the drain elevation ($z_\mathrm{d}$) of merged cells in the 2D model. $C_i$ and $C_{i+1}$ are the neighbouring 3D cells involved in the creation of the merged cell ($C_\mathrm{m}$) in the 2D model. $z_{\mathrm{d},i}$ and $z_{\mathrm{d},i+1}$ are the drain elevations of cell $C_i$ and $C_{i+1}$, respectively. "None" means that the 3D model cell does not include a drain. Reproduced from Gholami, A., Jazayeri, A., and Werner, A.D., 2025. Cross-Sectional Models of Groundwater Flow: Review and Correction for Transverse Flow. Groundwater, 63(5), 752–763. https://doi.org/10.1111/gwat.70017. Licensed under CC-BY.

| Case | $C_i$ | $C_{i+1}$ | $C_\mathrm{m}$ |
|---|---|---|---|
| 1 | $z_{\mathrm{d},i}$ | None | $z_{\mathrm{d},i}$ |
| 2 | None | $z_{\mathrm{d},i+1}$ | $z_{\mathrm{d},i+1}$ |
| 3 | None | None | None |
| 4 | $z_{\mathrm{d},i}$ | $z_{\mathrm{d},i+1}$ | Eq. (2) |

## A.5. Statistical measures of the match between 2D and 3D models

The heads of 2D and 3D models (along the alignment of the 2D cross section) were compared using the root-mean-square error (RMSE) and bias (Moriasi et al., 2007). Bias is the head from the 3D model minus the corresponding head of the 2D model. Values of RMSE and bias closer to 0 signify a higher degree of agreement. Positive and negative values of bias suggest that the head of the 2D model is, on average, lower and higher (respectively) than that of the 3D model. Where the 2D model represents the merger of two cells in the 3D model, Eq. (2) was employed to compute the 3D model head for comparison to the 2D model.

## References

Anderson, M.P., Woessner, W.W., and Hunt, R.J., 2015. Applied groundwater modeling: Simulation of flow and advective transport, 2nd ed. Academic Press, London. 630 p. https://doi.org/10.1016/C2009-0-21563-7

Gholami, A., Jazayeri, A., and Werner, A.D., 2025. Cross-Sectional Models of Groundwater Flow: Review and Correction for Transverse Flow. Groundwater, 63(5), 752–763. https://doi.org/10.1111/gwat.70017

Hughes, J.D., Langevin, C.D., Paulinski, S.R., Larsen, J.D., and Brakenhoff, D., 2024. FloPy workflows for creating structured and unstructured MODFLOW Models. Groundwater, 62(1), 124–39. https://doi.org/10.1111/gwat.13327

Langevin, C.D., Hughes, J.D., Banta, E.R., Niswonger, R.G., Panday, S., and Provost, A.M., 2017. Documentation for the MODFLOW 6 groundwater flow model. U.S. Geological Survey Techniques and Methods, book 6, chap. A55, 197 p. https://doi.org/10.3133/tm6A55

Leaf, A.T., and Fienen, M.N., 2022. Flopy: The Python interface for MODFLOW. Groundwater, 60(6), 710–12. https://doi.org/10.1111/gwat.13259

Morgan, L.K., Harrington, N., Werner, A.D., Hutson, J.L., Woods, J., and Knowling, M.J., 2015. South East regional water balance project–Phase 2. Development of a regional groundwater flow model. Technical Report Series No. 15/38, 142 p. https://goyderinstitute.org/wp-content/uploads/2023/06/goyder_trs_15-38_south_east_regional_water_balance_phase_2.pdf (Accessed November 04, 2024).

Moriasi, D.A., Arnold, J.G., Van Liew, M.W., Bingner, R.L., Harmel, R.D., and Veith, T.L., 2007. Model evaluation guidelines for systematic quantification of accuracy in watershed simulations. Transactions of the ASABE, 50(3), 885–900. https://doi.org/10.13031/2013.23153

# Appendix B – Extended offshore cross sections from parent model grid

Figures B1-B4 illustrate the grids for cross sections CSA, CSB, CSC and CSD, respectively, extracted from the regional model, truncated to focus on the coastal zone, and extended offshore. As can be seen in these figures, similar to CSE, cross sections CSA, CSC and CSD were extended offshore by 25 cells, while CSB was extended by 35 cells because freshwater reaches the offshore boundary in this cross section.

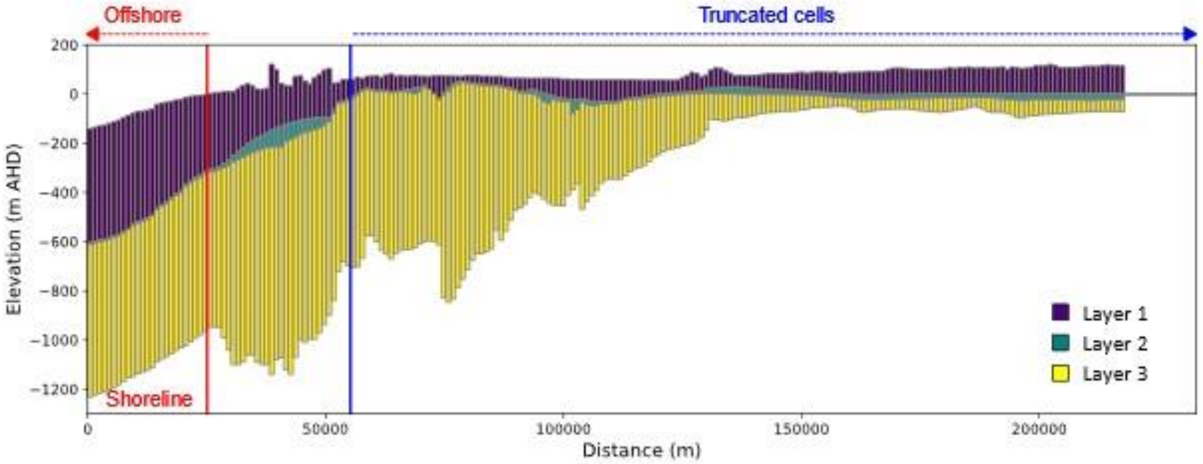

**Figure B1.** Grid extracted from the parent model of Morgan et al. (2015) for cross section A (CSA), showing the region where cells were removed (Truncated cells), and the extrapolation of the cross section into the continental shelf (Offshore), with the shoreline location shown as the red vertical line.

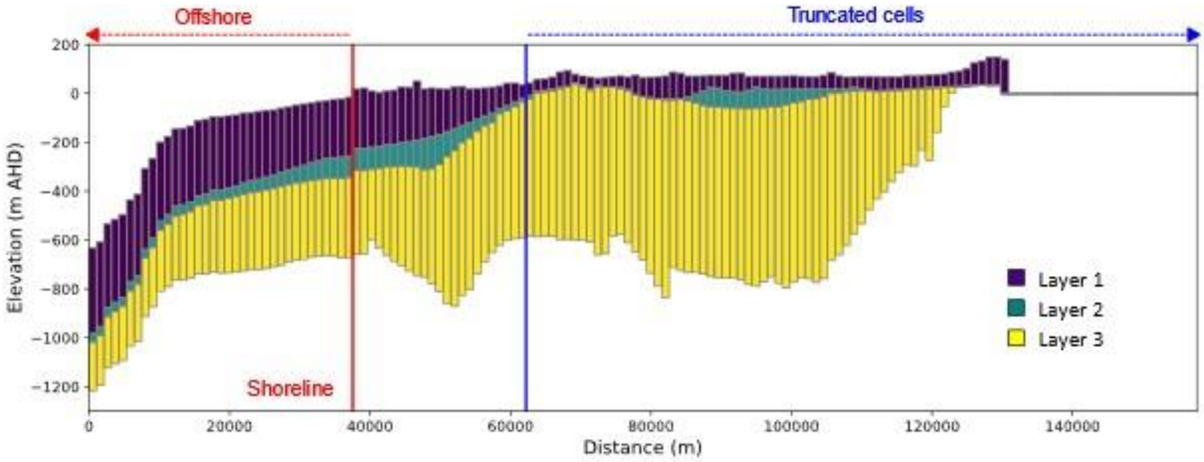

**Figure B2.** Grid extracted from the parent model of Morgan et al. (2015) for cross section B (CSB), showing the region where cells were removed (Truncated cells), and the extrapolation of the cross section into the continental shelf (Offshore), with the shoreline location shown as the red vertical line.

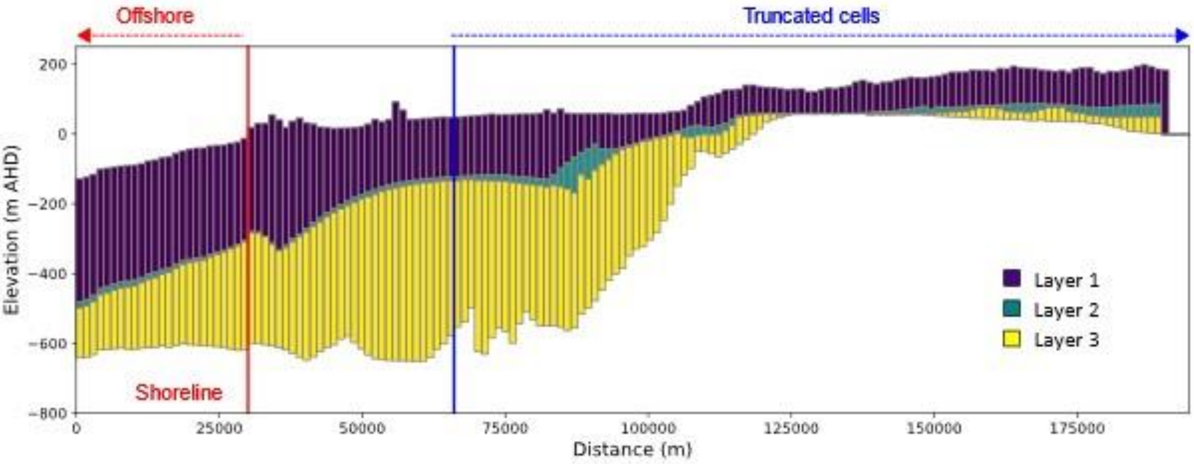

**Figure B3.** Grid extracted from the parent model of Morgan et al. (2015) for cross section C (CSC), showing the region where cells were removed (Truncated cells), and the extrapolation of the cross section into the continental shelf (Offshore), with the shoreline location shown as the red vertical line.

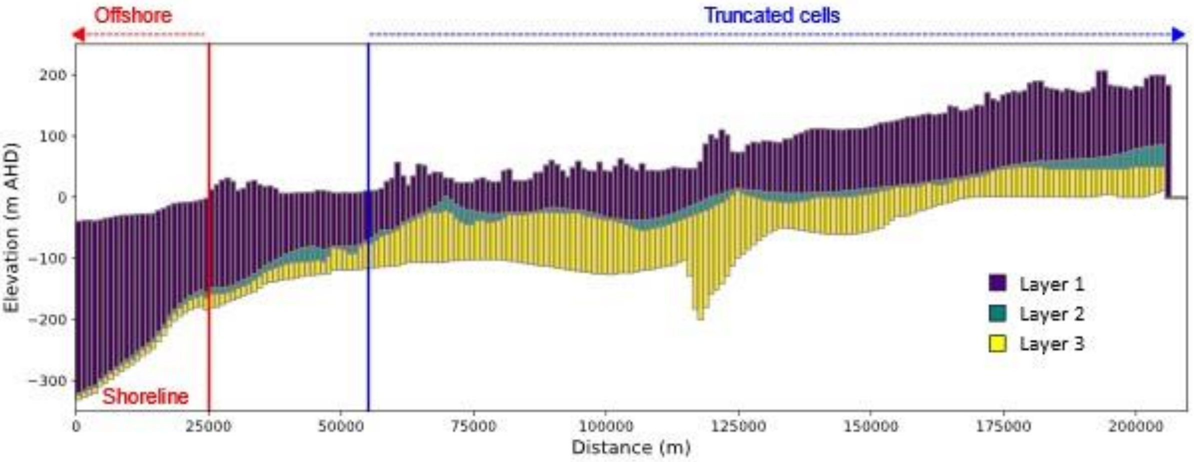

**Figure B4.** Grid extracted from the parent model of Morgan et al. (2015) for cross section D (CSD), showing the region where cells were removed (Truncated cells), and the extrapolation of the cross section into the continental shelf (Offshore), with the shoreline location shown as the red vertical line.

## References

Morgan, L.K., Harrington, N., Werner, A.D., Hutson, J.L., Woods, J., and Knowling, M.J., 2015. South East regional water balance project–Phase 2. Development of a regional groundwater flow model. Technical Report Series No. 15/38, 142 p. https://goyderinstitute.org/wp-content/uploads/2023/06/goyder_trs_15-38_south_east_regional_water_balance_phase_2.pdf (Accessed November 04, 2024).

# Appendix C – Head bias distribution in steady-state cross-sectional models

Figures C1-C4 show the comparison between the heads in CSA, CSB, CSC and CSD with the corresponding cells in the parent 3D model for steady-state, pre-development conditions.

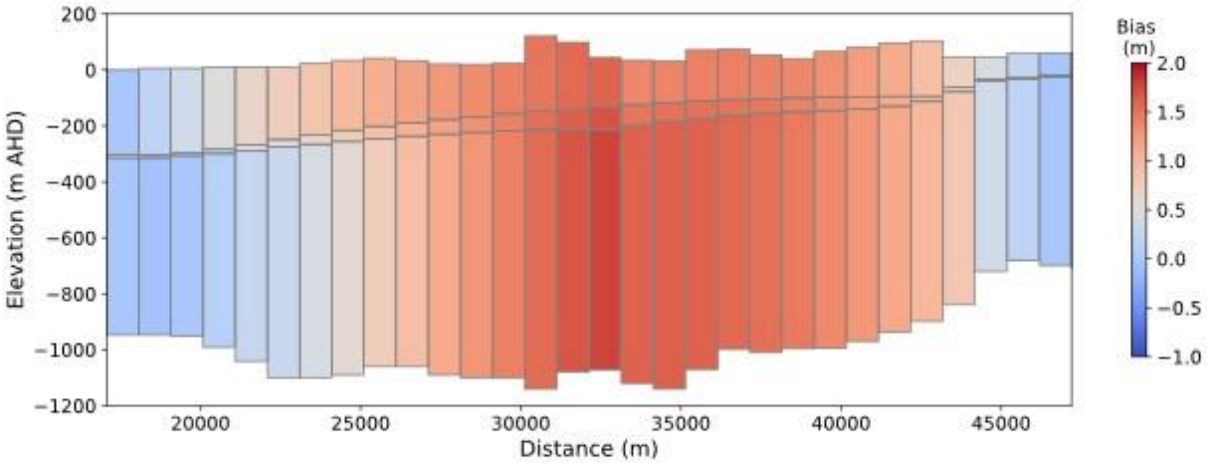

**Figure C1.** Comparison of heads between CSA (only freshwater is simulated) and the parent 3D model for steady-state, pre-development conditions, in terms of the bias, where a positive bias indicates that CSA heads are greater than the parent model. Heads from the parent model were transferred directly to specified-head conditions at the shoreline (left boundary) and the inland limit of the model (right boundary). Note here that the *x*-axis scale reflects distances in the regional model of Morgan et al. (2015) whereas the earlier *x*-axis (in Figure B1) is specific to the cross sections with extended offshore domains. The white cell located on the left boundary belongs to Layer 2 (aquitard) and represents an inactive cell at the shoreline in the regional model.

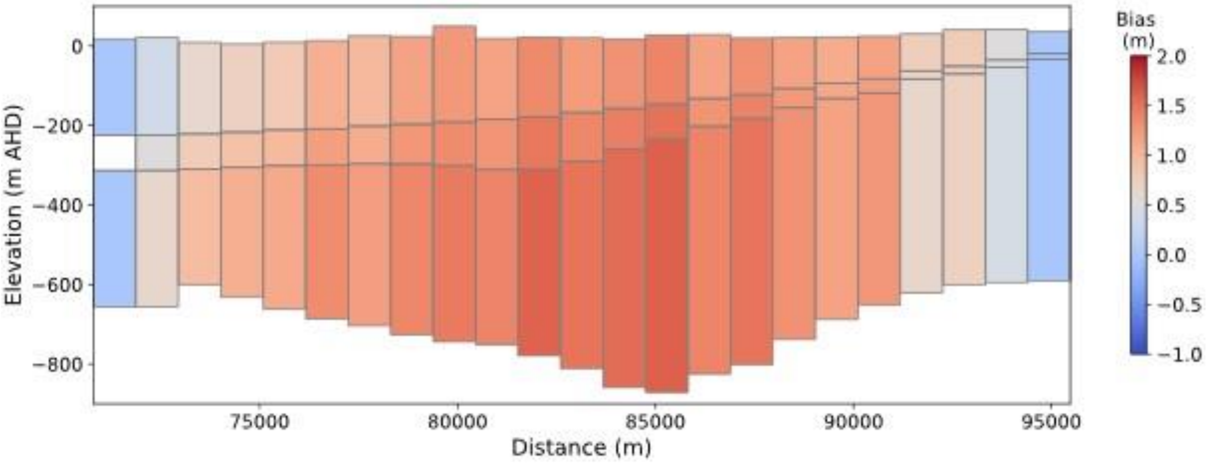

**Figure C2.** Comparison of heads between CSB (only freshwater is simulated) and the parent 3D model for steady-state, pre-development conditions, in terms of the bias, where a positive bias indicates that CSB heads are greater than the parent model. Heads from the parent model were transferred directly to specified-head conditions at the shoreline (left boundary) and the inland limit of the model (right boundary). Note here that the *x*-axis scale reflects distances in the regional model of Morgan et al. (2015) whereas the earlier *x*-axis (in Figure B2) is specific to the cross sections with extended offshore domains. The white cell located on the left boundary belongs to Layer 2 (aquitard) and represents an inactive cell at the shoreline in the regional model.

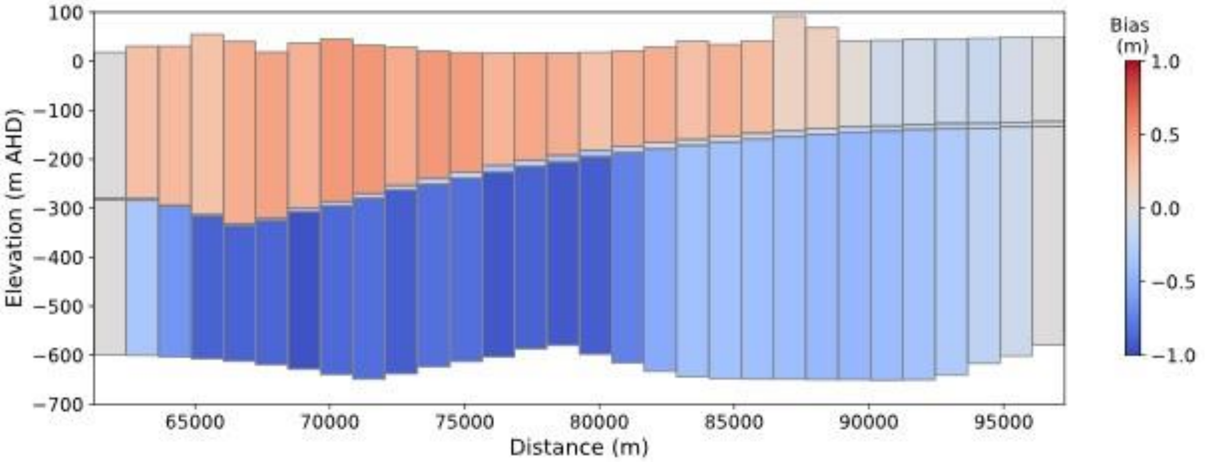

**Figure C3.** Comparison of heads between CSC (only freshwater is simulated) and the parent 3D model for steady-state, pre-development conditions, in terms of the bias, where a positive bias indicates that CSC heads are greater than the parent model. Heads from the parent model were transferred directly to specified-head conditions at the shoreline (left boundary) and the inland limit of the model (right boundary). Note here that the *x*-axis scale reflects distances in the regional model of Morgan et al. (2015) whereas the earlier *x*-axis (in Figure B3) is specific to the cross sections with extended offshore domains. The white cell located on the left boundary belongs to Layer 2 (aquitard) and represents an inactive cell at the shoreline in the regional model.

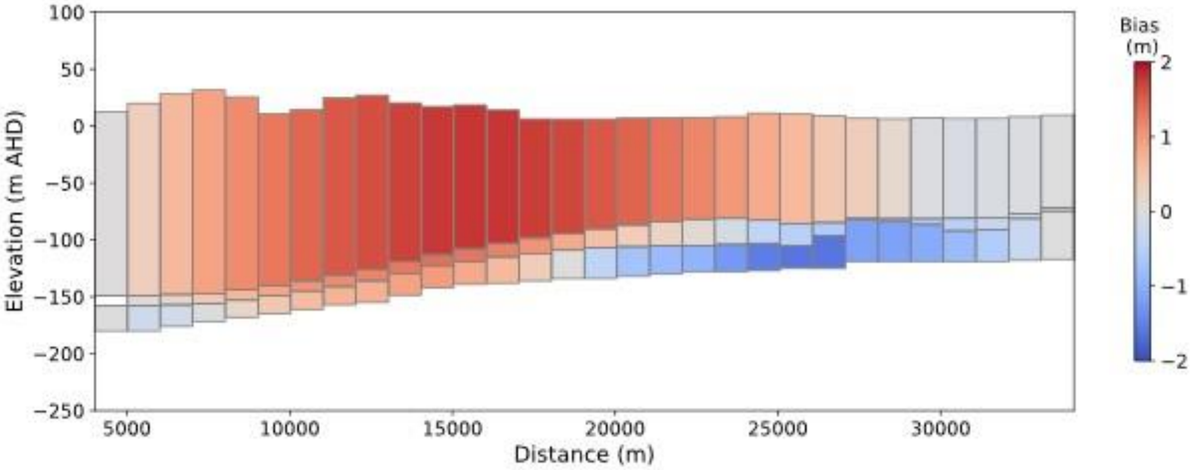

**Figure C4.** Comparison of heads between CSD (only freshwater is simulated) and the parent 3D model for steady-state, pre-development conditions, in terms of the bias, where a positive bias indicates that CSD heads are greater than the parent model. Heads from the parent model were transferred directly to specified-head conditions at the shoreline (left boundary) and the inland limit of the model (right boundary). Note here that the *x*-axis scale reflects distances in the regional model of Morgan et al. (2015) whereas the earlier *x*-axis (in FigureB4) is specific to the cross sections with extended offshore domains. The white cell located on the left boundary belongs to Layer 2 (aquitard) and represents an inactive cell at the shoreline in the regional model.

The bias values range from -0.05 m to 1.77 m for CSA, from -0.01 m to 1.62 m for CSB, from -0.97 m to 0.51 m for CSC and from -1.62 m to 1.79 m for CSD. While the magnitude of these biases across the four cross sections is considered acceptable, further investigation is warranted to better understand their origins—particularly given the various sources of error that may have arisen from the cross-section construction methodology. Note that, similar to the bias at the inland boundary of CSE, the bias in the four cross sections (CSA, CSB, CSC and CSD) is zero at their inland boundaries. This is because heads from the parent model were assigned to the inland boundary through a specified-head condition, and therefore, the head at their inland boundary matches exactly with the head at that location. A similar situation exists at the coastal boundary for all four cross sections (CSA, CSB, CSC and CSD). The white cell near the shoreline in Figures C1-C4 corresponds to Layer 2 (aquitard), which is an inactive cell in the regional model.

## References

Morgan, L.K., Harrington, N., Werner, A.D., Hutson, J.L., Woods, J., and Knowling, M.J., 2015. South East regional water balance project–Phase 2. Development of a regional groundwater flow model. Technical Report Series No. 15/38, 142 p. https://goyderinstitute.org/wp-content/uploads/2023/06/goyder_trs_15-38_south_east_regional_water_balance_phase_2.pdf (Accessed November 04, 2024).

# Appendix D – Head bias distribution in extended offshore steady-state cross-sectional models

Figures D1-D4 show the distribution of head bias (between the cross sections—where only freshwater is simulated in the offshore extension—and the parent 3D model under steady-state, pre-development conditions) when the cross sections were extended offshore.

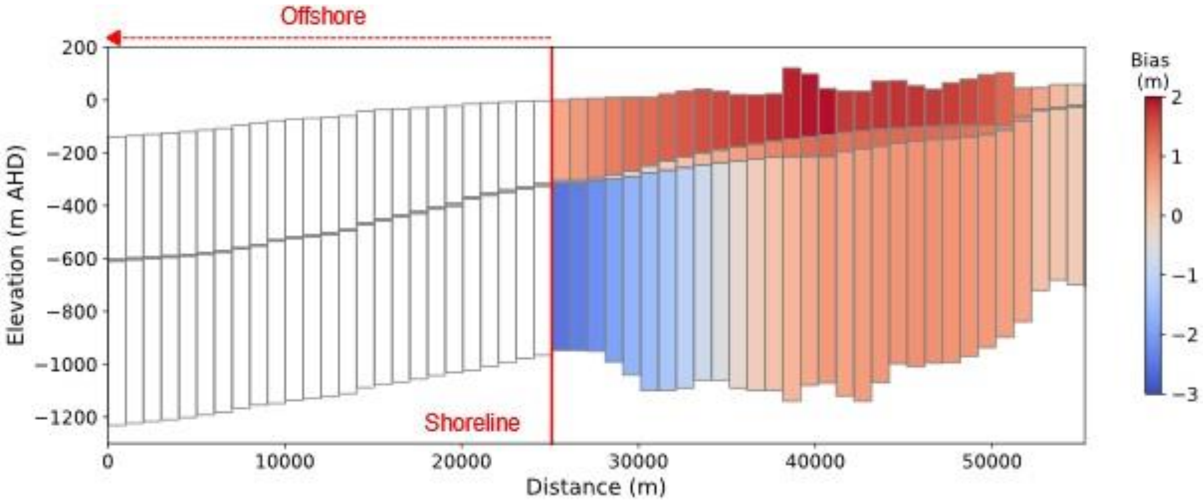

**Figure D1.** Comparison of heads between CSA (with offshore extension, only freshwater is simulated) and the parent 3D model for steady-state, pre-development conditions, in terms of the bias, where a positive bias indicates that CSA heads are greater than the parent model. Heads from the parent model were transferred directly to specified-head conditions at the inland limit of the model (right boundary), whereas the coastal boundary condition adopts the equivalent freshwater heads of the sea. Offshore cells are blank because these were not used in the parent model. The white cell located near the shoreline (onshore part), belongs to Layer 2 (aquitard), and represents an inactive cell at the shoreline in the regional model.

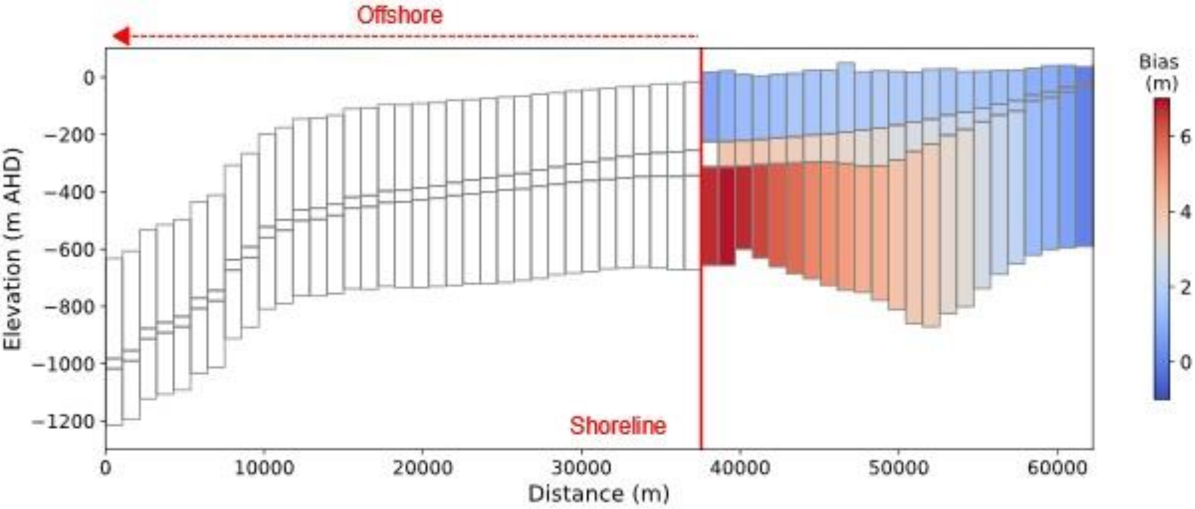

**Figure D2.** Comparison of heads between CSB (with offshore extension, only freshwater is simulated) and the parent 3D model for steady-state, pre-development conditions, in terms of the bias, where a positive bias indicates that CSB heads are greater than the parent model. Heads from the parent model were transferred directly to specified-head conditions at the inland limit of the model (right boundary), whereas the coastal boundary condition adopts the equivalent freshwater heads of the sea. Offshore cells are blank because these were not used in the parent model. The white cell located near the shoreline (onshore part), belongs to Layer 2 (aquitard), and represents an inactive cell at the shoreline in the regional model.

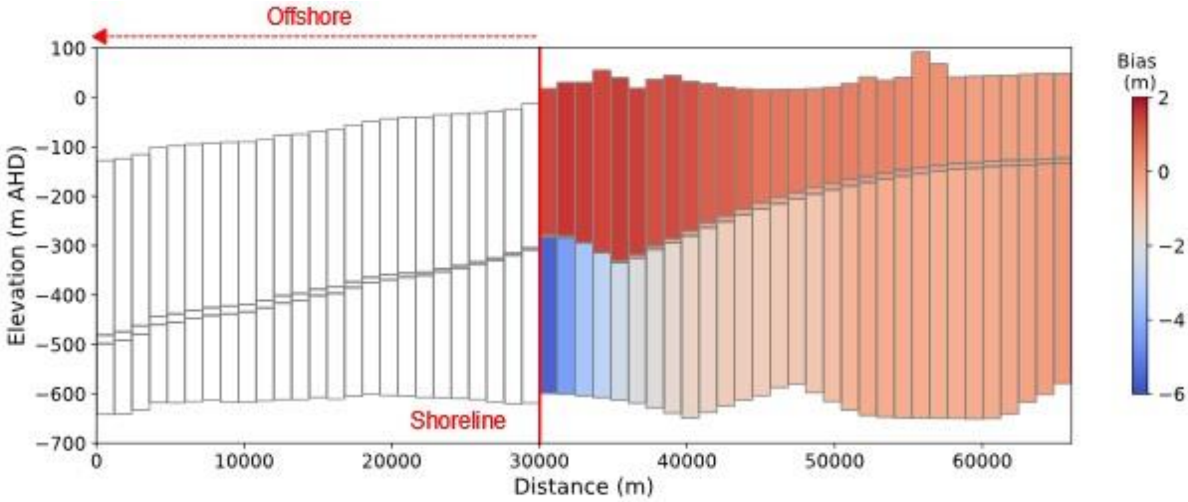

**Figure D3.** Comparison of heads between CSC (with offshore extension, only freshwater is simulated) and the parent 3D model for steady-state, pre-development conditions, in terms of the bias, where a positive bias indicates that CSC heads are greater than the parent model. Heads from the parent model were transferred directly to specified-head conditions at the inland limit of the model (right boundary), whereas the coastal boundary condition adopts the equivalent freshwater heads of the sea. Offshore cells are blank because these were not used in the parent model. The white cell located near the shoreline (onshore part), belongs to Layer 2 (aquitard), and represents an inactive cell at the shoreline in the regional model.

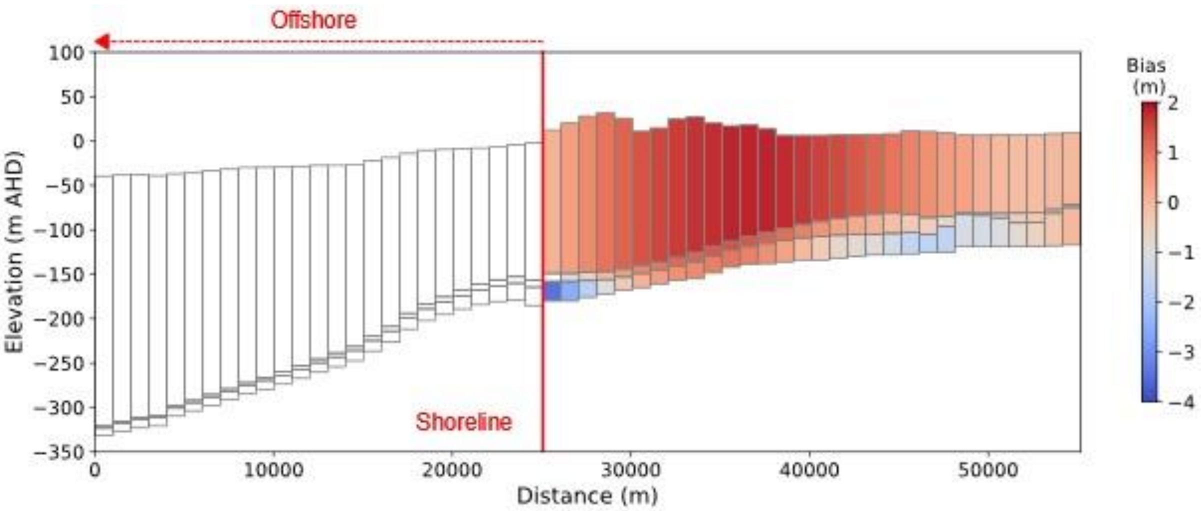

**Figure D4.** Comparison of heads between CSD (with offshore extension, only freshwater is simulated) and the parent 3D model for steady-state, pre-development conditions, in terms of the bias, where a positive bias indicates that CSD heads are greater than the parent model. Heads from the parent model were transferred directly to specified-head conditions at the inland limit of the model (right boundary), whereas the coastal boundary condition adopts the equivalent freshwater heads of the sea. Offshore cells are blank because these were not used in the parent model. The white cell located near the shoreline (onshore part), belongs to Layer 2 (aquitard), and represents an inactive cell at the shoreline in the regional model.

The bias values range from -2.52 m to 1.96 m for CSA, from --0.01 m to 6.89 m for CSB, from -5.58 m to 1.56 m for CSC and from -3.44 m to 1.83 m for CSD. These biases are larger than what was obtained from the direct extrapolation of cross sections from the regional model, as shown in Appendix C. We attribute this to the changes in the treatment of the coastal boundary in cross-sectional models relative to the regional model. That is, our simulation treated the sea as equivalent freshwater heads and the offshore aquifer as containing freshwater. The results indicate that the bias increased at the coastal boundary once the specified heads from Morgan et al. (2015) were removed and replaced with a more physically realistic representation of the offshore aquifer (albeit, we have neglected buoyancy forces within the offshore aquifer arising from the seawater in it). To determine which set of shoreline head values is more appropriate, i.e., those produced by the physically based coastal simulation in the four cross sections of the current study or those used by Morgan et al. (2015), it is essential to compare both with field measurements of groundwater heads near the coast. A review of the available observation well measurements in the near-coastal fringe indicates that there are no heads measurements close to the shoreline and near to our cross section with which we can compare field data to the near-shore heads in the various models.

## References

Morgan, L.K., Harrington, N., Werner, A.D., Hutson, J.L., Woods, J., and Knowling, M.J., 2015. South East regional water balance project–Phase 2. Development of a regional groundwater flow model. Technical Report Series No. 15/38, 142 p. https://goyderinstitute.org/wp-content/uploads/2023/06/goyder_trs_15-38_south_east_regional_water_balance_phase_2.pdf (Accessed November 04, 2024).

# Appendix E – Steady-state head distribution comparison: Refined offshore models vs parent model

Seawater intrusion simulation requires smaller cells than was necessary for the simulation of only fresh groundwater. Thus, refined grids were constructed that are based on the parent model except cells were subdivided to produce a finer grid resolution in cross sections. Figures E1-E4 illustrate the refined grids for CSA to CSD (respectively), displaying head values (only freshwater is simulated) represented as a colour flood, alongside the corresponding heads in the parent model, interpolated to the locations of CSA, CSB, CSC and CSD, respectively.

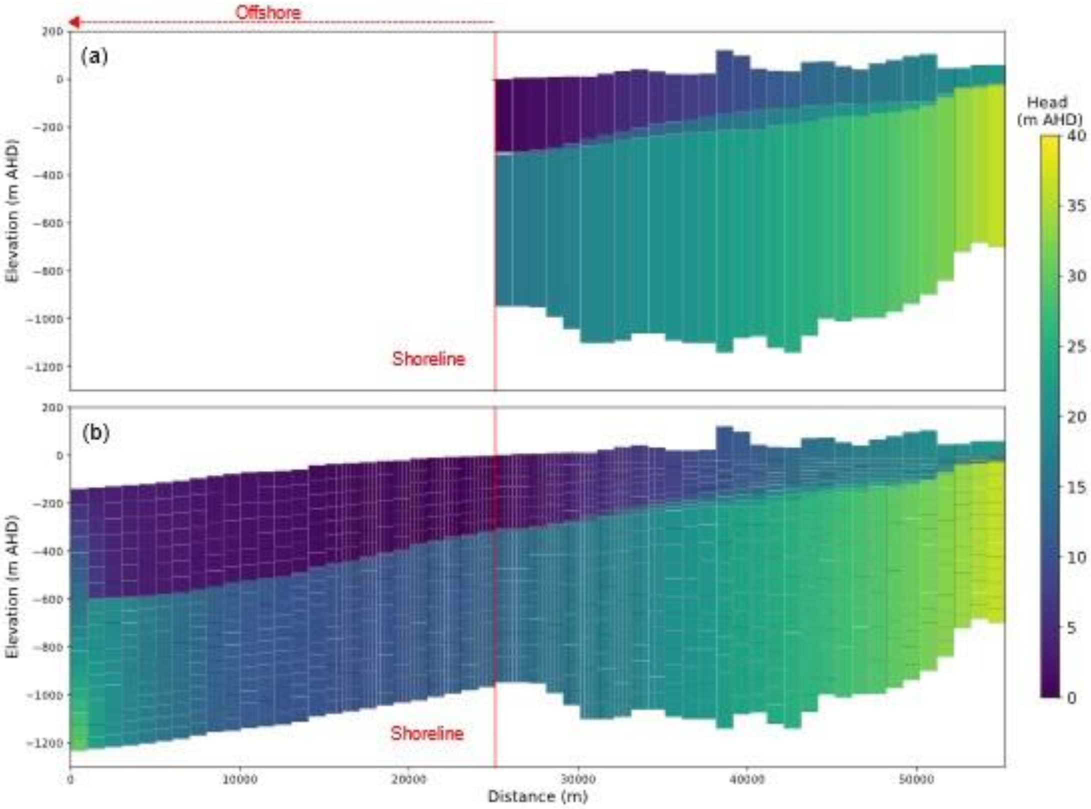

**Figure E1.** Comparison of heads between: (a) the parent 3D model at the location of cross section A (CSA), and (b) CSA with offshore extension and refined grid (only freshwater is simulated). This simulation represents steady-state, pre-development conditions. The white cell in (a), located near the shoreline, belongs to Layer 2 (aquitard), and represents an inactive cell at the shoreline in the regional model.

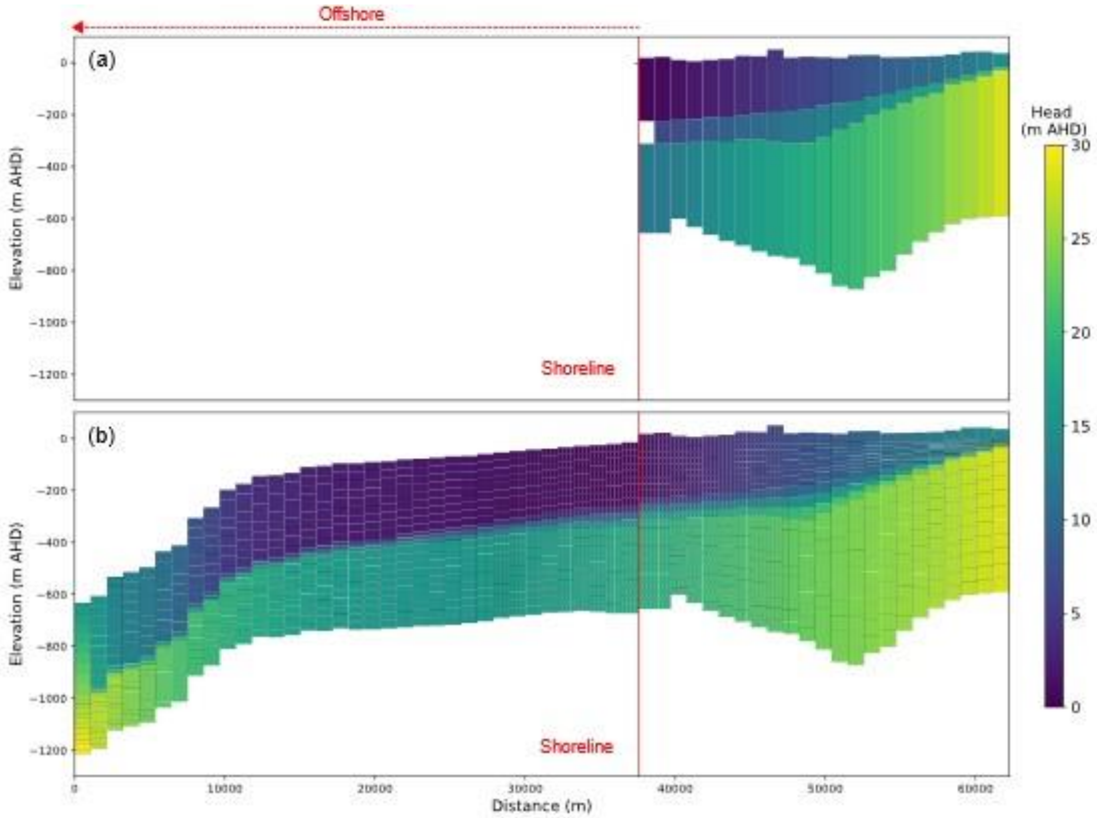

**Figure E2.** Comparison of heads between: (a) the parent 3D model at the location of cross section B (CSB), and (b) CSB with offshore extension and refined grid (only freshwater is simulated). This simulation represents steady-state, pre-development conditions. The white cell in (a), located near the shoreline, belongs to Layer 2 (aquitard), and represents an inactive cell at the shoreline in the regional model.

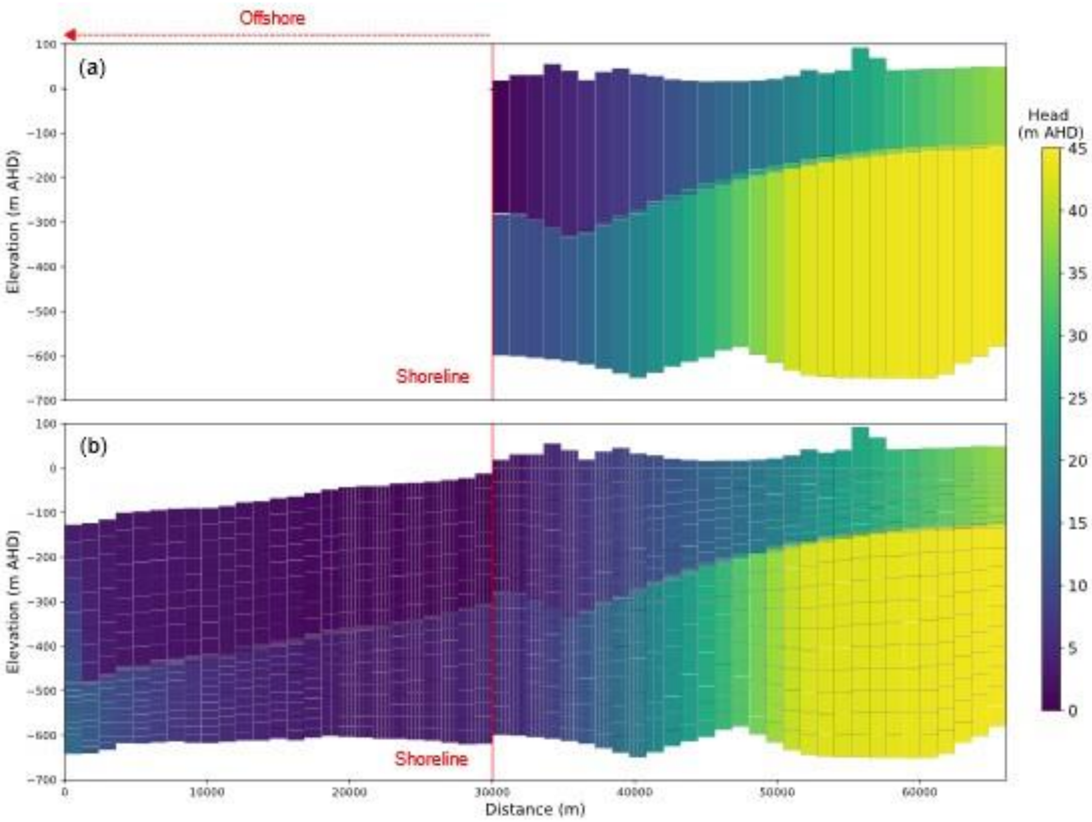

**Figure E3.** Comparison of heads between: (a) the parent 3D model at the location of cross section C (CSC), and (b) CSC with offshore extension and refined grid (only freshwater is simulated). This simulation represents steady-state, pre-development conditions. The white cell in (a), located near the shoreline, belongs to Layer 2 (aquitard), and represents an inactive cell at the shoreline in the regional model.

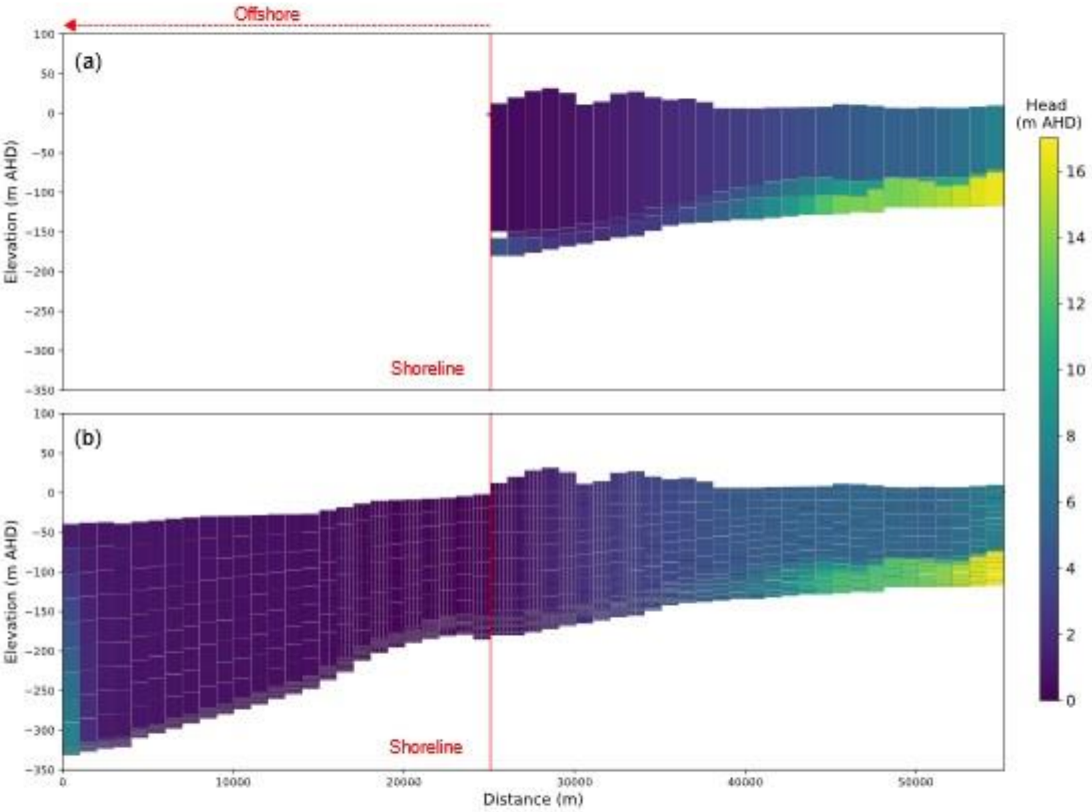

**Figure E4.** Comparison of heads between: (a) the parent 3D model at the location of cross section D (CSD), and (b) CSD with offshore extension and refined grid (only freshwater is simulated). This simulation represents steady-state, pre-development conditions. The white cell in (a), located near the shoreline, belongs to Layer 2 (aquitard), and represents an inactive cell at the shoreline in the regional model.

The results in Figures E1-E4 shows that the extended, refined grid of each cross-sectional model (CSA, CSB, CSC and CSD) produced heads that are reasonably consistent with the parent model (Morgan et al., 2015) extrapolated to their respective locations, although the variations in head values near the shoreline are larger than was originally anticipated. Although the match is not perfect, it is sufficient to provide confidence that the methodology for extracting cross-sectional models from Morgan et al. (2015) was effective. The sources of differences between the cross-sectional models and the Morgan et al. (2015) model may stem from inherent differences between 2D and 3D models (mainly the flow lateral (alongshore) to cross sections that is included in 3D models but neglected in 2D models), the methodology used to extract the cross sections, and the replacement of the constant-head boundary assigned by Morgan et al. (2015) with a representation of the offshore aquifer.

Grid refinement for CSA, CSB, CSC and CSD was applied in both the horizontal and vertical directions. For example, 10 of the original parent cells representing both offshore and onshore regions were reduced in their horizontal size. These 10 cells occupied horizontal distances, in the parent model, of approximately 10 km, 11 km, 12 km and 10 km for CSA, CSB, CSC and CSD, respectively (note that the cell length along the direction of the cross section varies due to the different orientations of each cross section). Near the shoreline, each cell in the extracted cross section from the regional model was subdivided into four smaller cells. The maximum ratio of a cell's horizontal dimension to that of its adjacent cell was 1.6, slightly exceeding the 1.5 ratio recommended by Anderson et al. (2015) for maintaining model stability and accuracy.

The vertical subdivision of the parent model layers, for each cross section, was as follows: (a) CSA: the first layer consists of twelve sub-layers, the second has three and the third has eight; (b) CSB: the first layer has ten sub-layers, the second has three and the third has ten; (c) CSC: the first layer has ten sub-layers, the second has three and the third has ten; (d) CSD: the first layer has ten sub-layers, the second has three and the third has six. There are differences in the number of sublayers across different cross sections due to varying layer thicknesses. The choice of cell subdivision was a trade-off between model run times and the accuracy of the model in reproducing complex freshwater-seawater mixing processes, as described in Appendix H.

## References

Morgan, L.K., Harrington, N., Werner, A.D., Hutson, J.L., Woods, J., and Knowling, M.J., 2015. South East regional water balance project–Phase 2. Development of a regional groundwater flow model. Technical Report Series No. 15/38, 142 p. https://goyderinstitute.org/wp-content/uploads/2023/06/goyder_trs_15-38_south_east_regional_water_balance_phase_2.pdf (Accessed November 04, 2024).

# Appendix F – Transient heads comparison: Cross-sectional models vs parent model

In this section, the heads of CSA, CSB, CSC and CSD were compared to the parent model during the transient simulation (44 years). In all cross sections, similar to the approach used in CSE, as explained in the main body of the report, a time-varying specified-head condition was applied at the inland boundary, with heads extracted from the parent model. Recharge and other hydrological stresses at the location of each cross section were also extracted from the regional model. Figures F1 to F4 each illustrate four groundwater level hydrographs, showing data from both the parent model and corresponding locations in CSA, CSB, CSC and CSD.

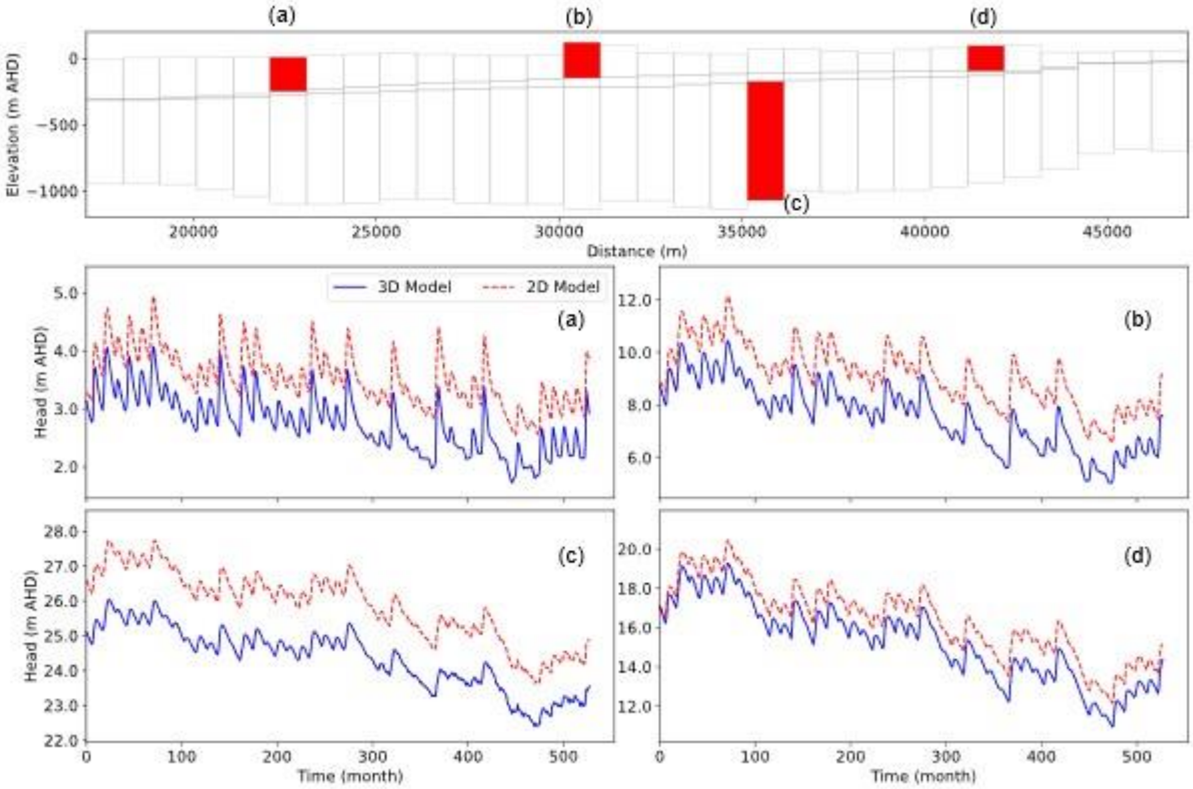

**Figure F1.** Four hydrographs comparing heads from the transient simulation (freshwater only) of cross section A (CSA) with the parent 3D model. The top figure identifies the cells from which model hydrographs, (a) to (d), were extracted. The distribution of bias in the pre-development steady-state model (used as initial conditions for the transient model) is shown in Figure C1, while the bias at the end of the transient simulation is shown in Figure G1.

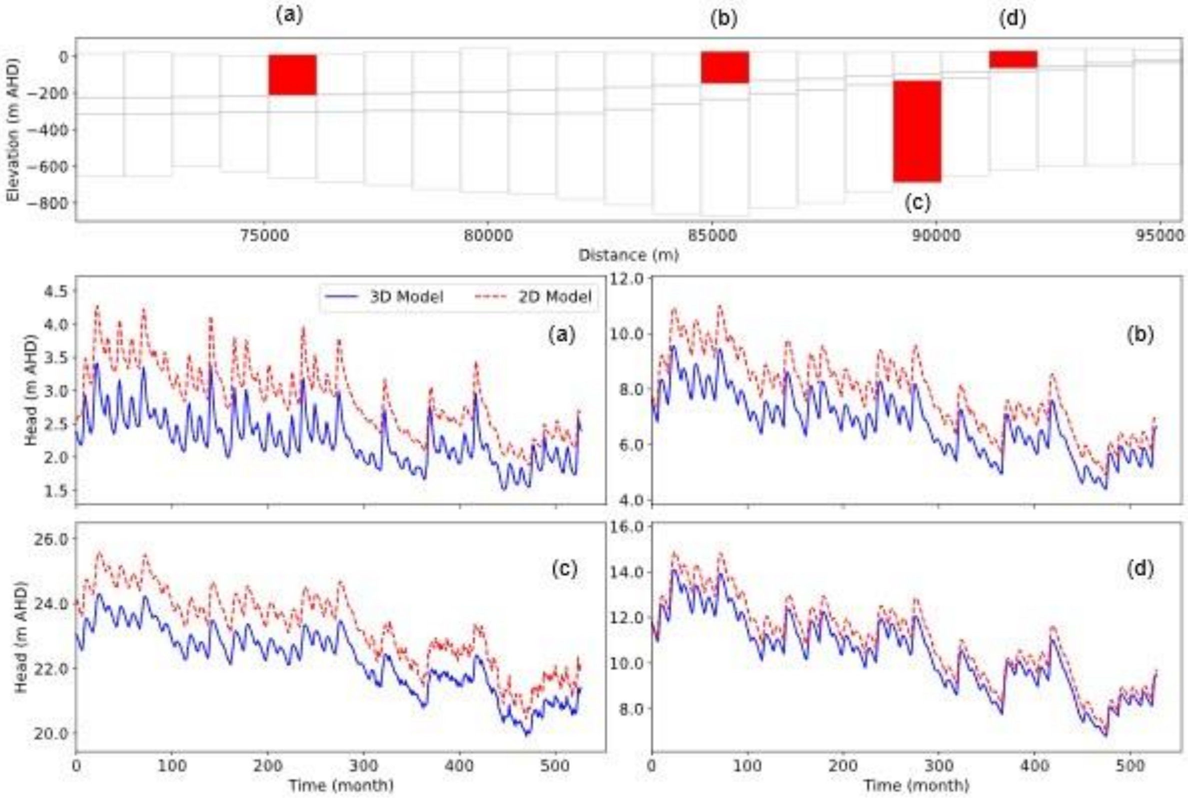

**Figure F2.** Four hydrographs comparing heads from the transient simulation (freshwater only) of cross section B (CSB) with the parent 3D model. The top figure identifies the cells from which model hydrographs, (a) to (d), were extracted. The distribution of bias in the pre-development steady-state model (used as initial conditions for the transient model) is shown in Figure C2, while the bias at the end of the transient simulation is shown in Figure G2.

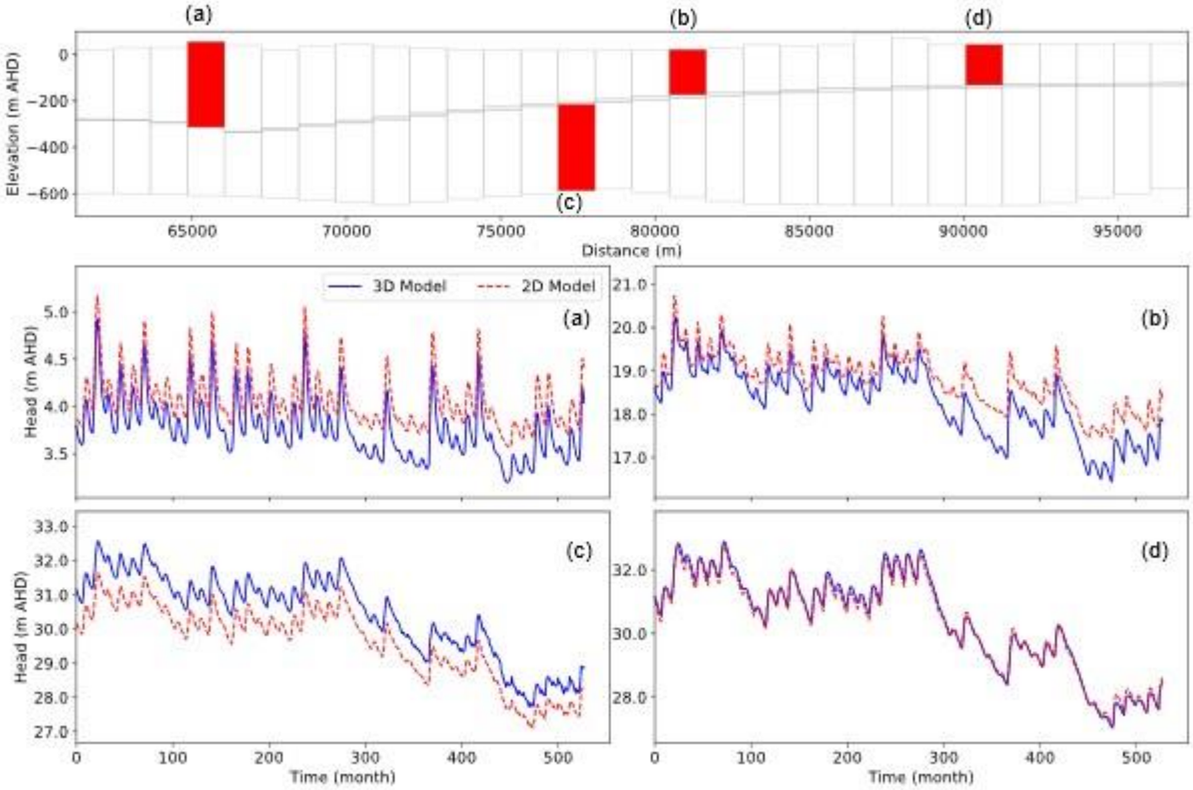

**Figure F3.** Four hydrographs comparing heads from the transient simulation (freshwater only) of cross section C (CSC) with the parent 3D model. The top figure identifies the cells from which model hydrographs, (a) to (d), were extracted. The distribution of bias in the pre-development steady-state model (used as initial conditions for the transient model) is shown in Figure C3, while the bias at the end of the transient simulation is shown in Figure G3.

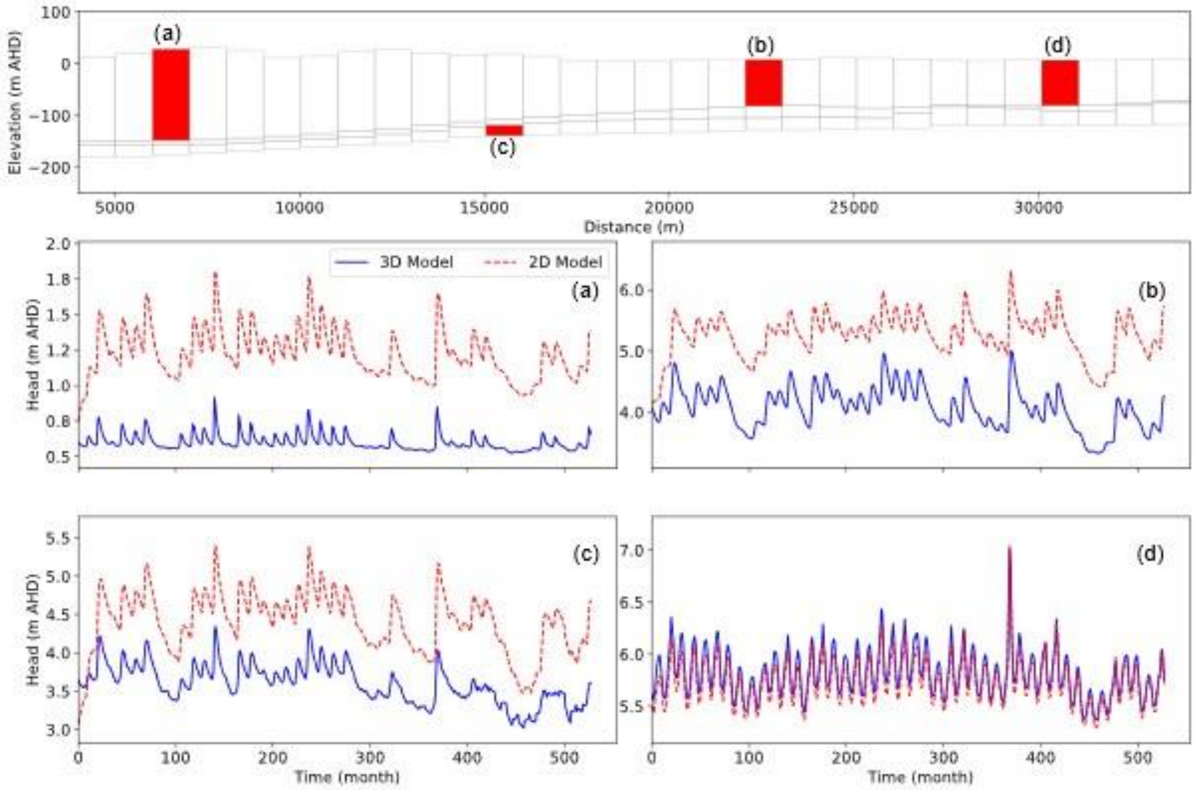

**Figure F4.** Four hydrographs comparing heads from the transient simulation (freshwater only) of cross section D (CSD) with the parent 3D model. The top figure identifies the cells from which model hydrographs, (a) to (d), were extracted. The distribution of bias in the pre-development steady-state model (used as initial conditions for the transient model) is shown in Figure C4, while the bias at the end of the transient simulation is shown in Figure G4.

Figure F1 demonstrates that the groundwater heads in CSA at all four locations are greater than those in the parent model. The average of this difference is approximately 1 m near the coast and around 2 m in the remaining cells. Figure F2 shows a similar trend for CSB, where the heads in the cross-sectional model are greater than those in the parent model. Although the head difference in CSB is smaller than that observed in CSA, a slight difference still exists. At the cell near the inland boundary (point d), the groundwater heads in the cross-sectional and parent models are close to each other, as expected. Figure F3 shows that the groundwater heads in the cross-sectional model for CSC are closer to those in the regional model compared to CSA and CSB. In the cells located in the upper aquifer (points a and b), the cross-sectional model predicts higher heads than the parent model, whereas in the lower aquifer (point c), the heads are lower than those in the regional model. Near the inland boundary (point d), the groundwater heads in the cross-sectional and regional models closely match. Figure F4 shows that the groundwater heads in the cross-sectional model for CSD are higher than those in the regional model in both the upper and lower aquifers. Figures F1 to F4 demonstrate that the regional model's dynamics are reasonably well reproduced in these cross sections, as indicated by mostly adequate alignments of the hydrographs. The mismatch in the heads of the cross-sectional models and the regional model highlight the importance of carefully parameterising the coastal fringe in regional models, where tidal fluctuations also modify the effective freshwater head at the cost, in addition to groundwater salinity profiles.

# Appendix G – Head bias distribution in extended offshore transient cross-sectional models

Figures G1 to G4 illustrate the bias at CSA, CSB, CSC and CSD at the end of the transient simulation (1970–2013).

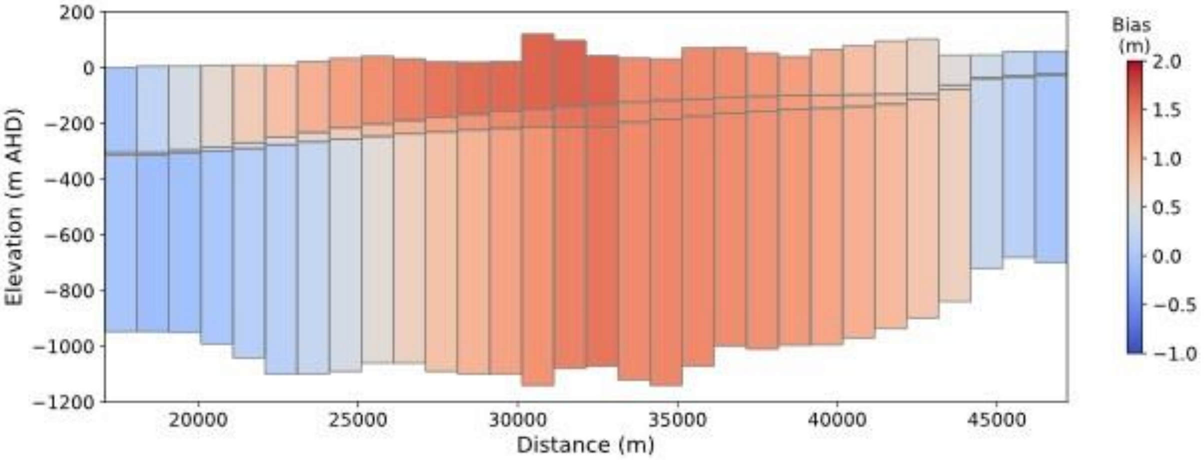

**Figure G1.** Comparison of heads from cross section A (CSA; transient simulation, freshwater only) and the parent model at the end of the transient simulation (1970–2013), where positive bias indicates that the heads of CSA exceed those of the parent model. The white cell located on the left boundary belongs to Layer 2 (aquitard) and represents an inactive cell at the shoreline in the regional model.

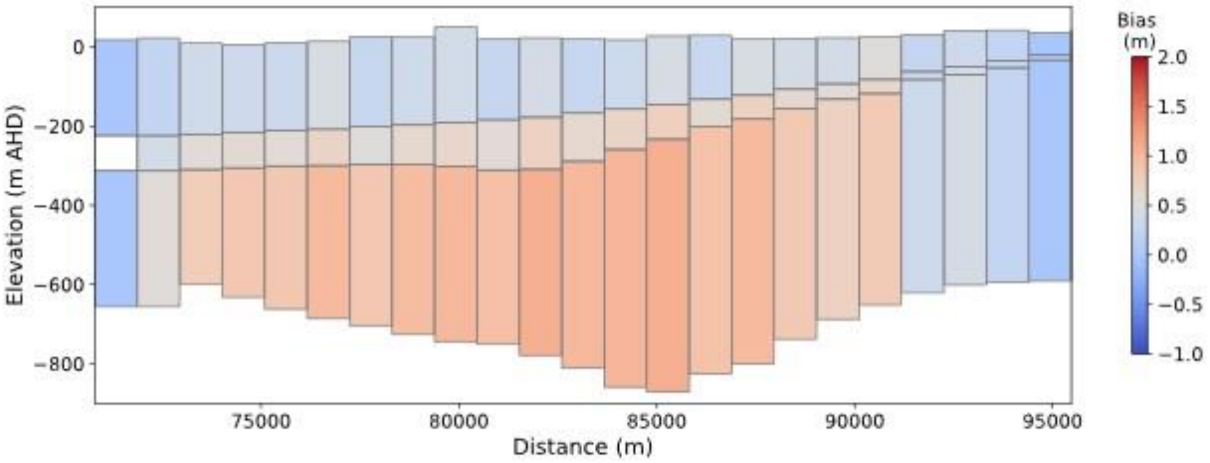

**Figure G2.** Comparison of heads from cross section B (CSB; transient simulation, freshwater only) and the parent model at the end of the transient simulation (1970–2013), where positive bias indicates that the heads of CSB exceed those of the parent model. The white cell located on the left boundary belongs to Layer 2 (aquitard) and represents an inactive cell at the shoreline in the regional model.

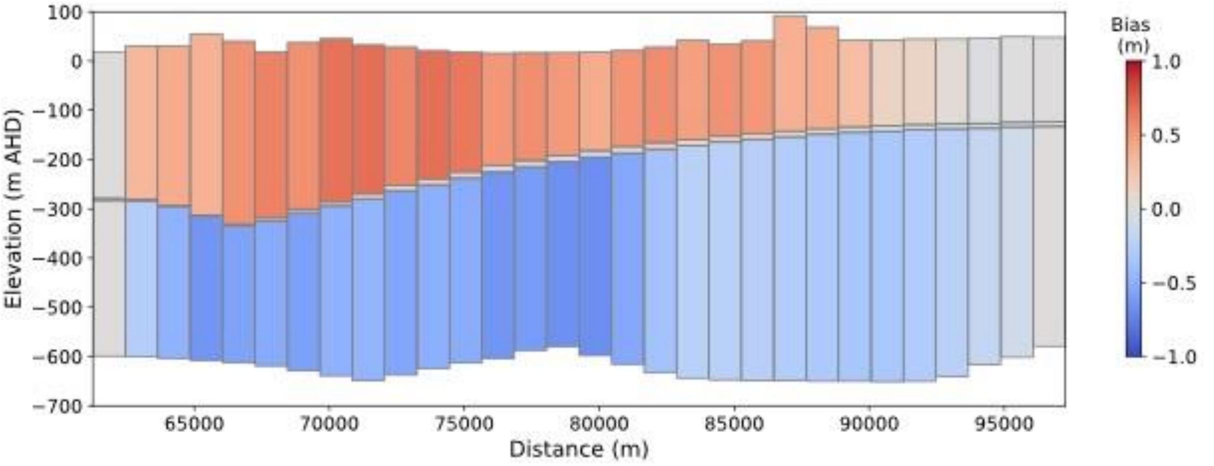

**Figure G3.** Comparison of heads from cross section C (CSC; transient simulation, freshwater only) and the parent model at the end of the transient simulation (1970–2013), where positive bias indicates that the heads of CSC exceed those of the parent model. The white cell located on the left boundary belongs to Layer 2 (aquitard) and represents an inactive cell at the shoreline in the regional model.

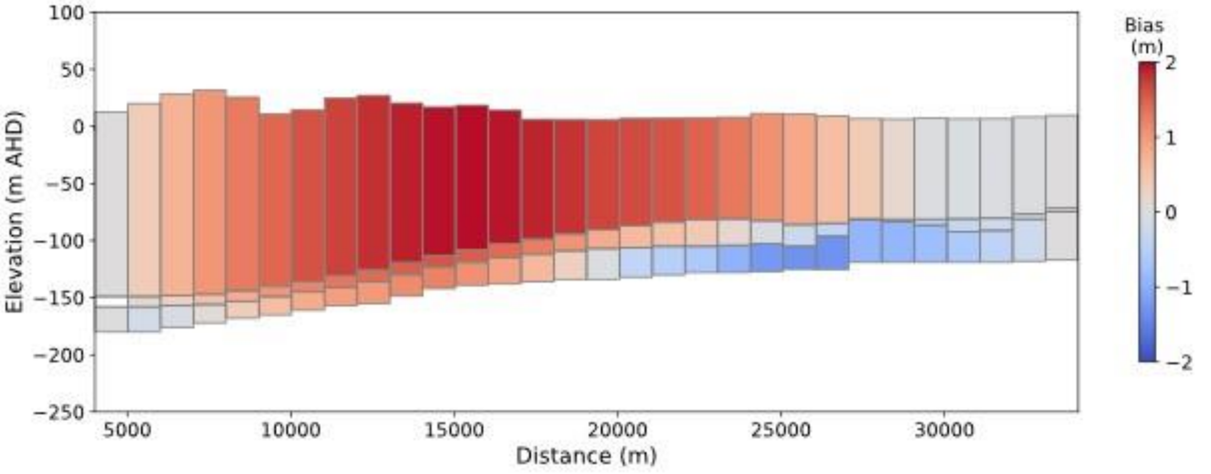

**Figure G4**. Comparison of heads from cross section D (CSD; transient simulation, freshwater only) and the parent model at the end of the transient simulation (1970–2013), where positive bias indicates that the heads of CSD exceed those of the parent model. The white cell located on the left boundary belongs to Layer 2 (aquitard) and represents an inactive cell at the shoreline in the regional model.

The bias values range from -0.10 m to 1.61 m for CSA, from -0.01 m to 1.08 m for CSB, from -0.69 m to 0.69 m for CSC and from -1.32 m to 1.96 m for CSD. These results demonstrate that the match between the cross-sectional model and the parent model is reasonable for all cross sections. Notice that the bias in Figures G1 to G4 aligns with the hydrographs shown in Figures F1 to F4, respectively. The main reason behind this bias is the fundamental difference between cross-sectional and 3D models; extracting a cross section from a 3D model removes flow components perpendicular to the section, which can lead to variations in head values. Error may also potentially arise from the averaging of the aquifer properties from the regional model that is needed to develop cross sections.

The patterns of bias observed in Figures G1 to G4 show many of the same patterns as observed in the bias of the steady-state results (Figures C1 to C4). For example, in CSC, heads are over-estimated in the upper aquifer and under-estimated in the lower aquifer in the steady-state results and at the end of the 44-year transient simulation.

# Appendix H – Steady-state salinity distribution: Scenario 1

Figures H1 to H4 present freshwater-seawater distributions under pre-development, steady-state conditions for CSA, CSB, CSC and CSD, showing the truncated, offshore-extended and refined model grid. In these cases, the density-dependence of freshwater-seawater interactions is simulated, which modifies the model heads due to the accompanying buoyancy forces and causes considerably longer model run times (up to 10 hours on a standard desktop computer). These results illustrate the salinity distribution after approximately 30,000 years, with aquifer stresses taken from 1970. It is usual practice to consider these types of steady-state simulations as the "pre-development" condition, even though significant pumping is included in the regional model from which these cases were derived.

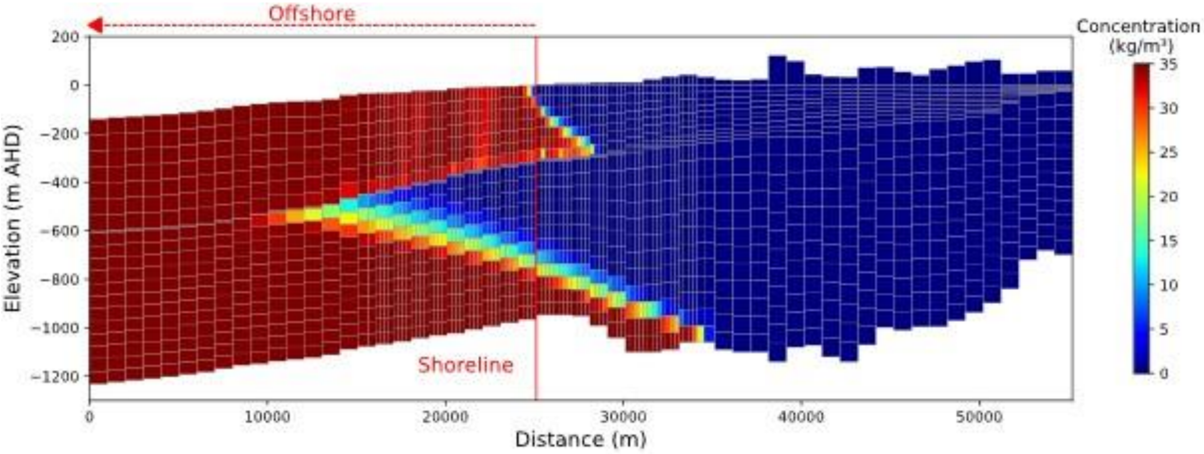

**Figure H1.** Salinity distribution of cross section A (CSA), representing pre-development, steady-state conditions.

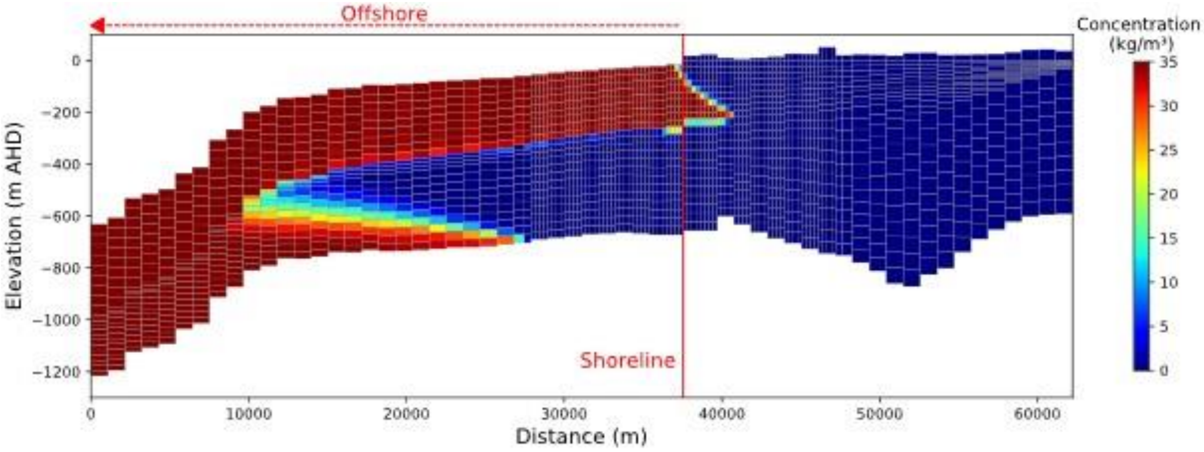

**Figure H2.** Salinity distribution of cross section B (CSB), representing pre-development, steady-state conditions.

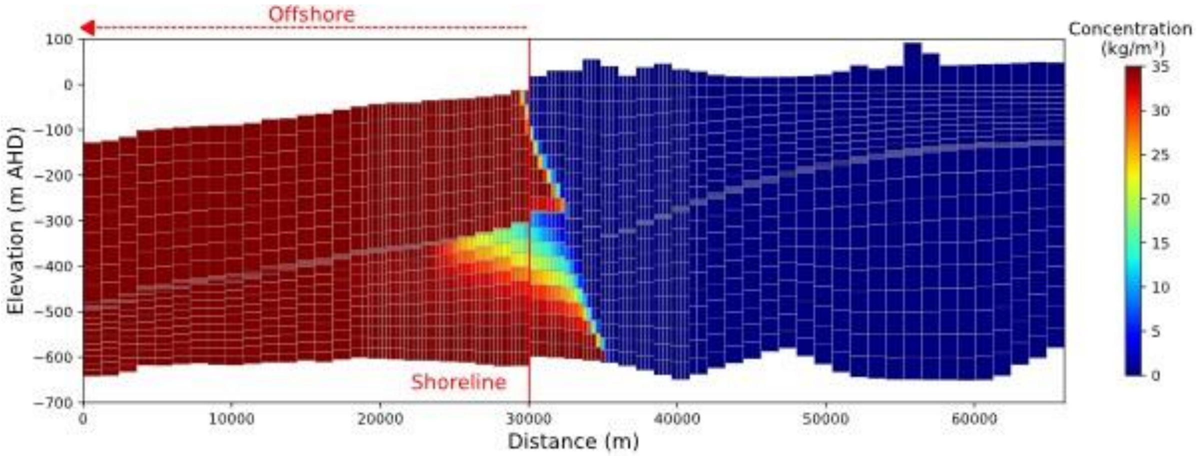

**Figure H3.** Salinity distribution of cross section C (CSC), representing pre-development, steady-state conditions.

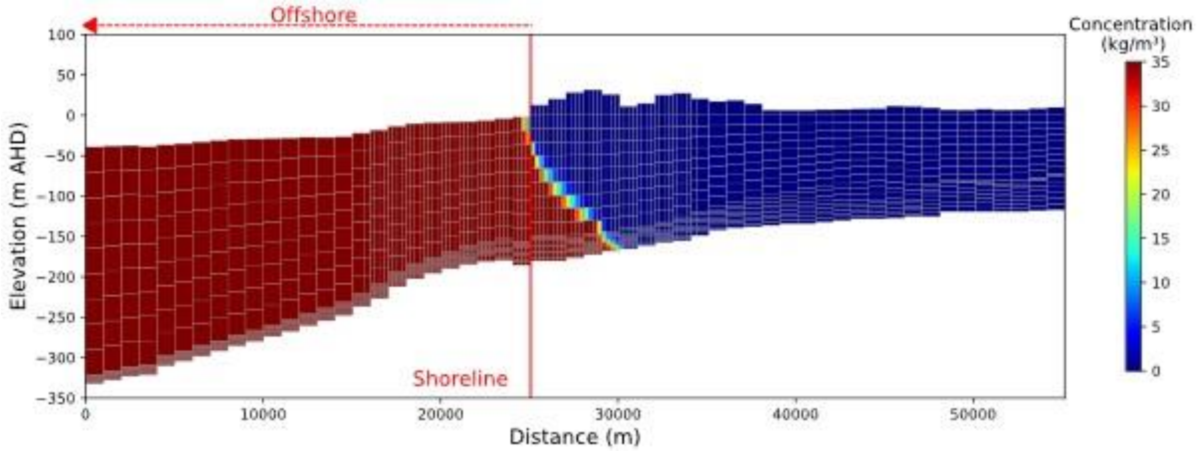

**Figure H4.** Salinity distribution of cross section D (CSD), representing pre-development, steady-state conditions.

Figure H1 demonstrates that, at CSA, seawater occurs up to 3,181 m inland in the upper aquifer (TLA), while it reaches up to 9,344 m inland in the lower aquifer (TCSA). Figure H1 also shows a substantial offshore freshwater extent in the TCSA, with the interface tip extending approximately 12,251 m offshore. Here, the distance to the tip is based on the 50% of seawater salinity at the top of the aquifer. Thus, the freshwater-seawater interface has a vast length of almost 22 km. The colour variations in the seawater region of the TLA of CSA (Figure H1) result from unstable fingering, as explained in main report for CSE. The extent to which this occurs in reality is likely to depend on the properties of the offshore aquitard, for which little is known.

Figure H1 shows two distinct types of mixing zone: a relatively sharp interface in the TLA and a more dispersed mixing zone in the TCSA. That is, there is greater mixing between freshwater and seawater in the TCSA, causing significant regions containing brackish water. The contrast between the mixing zones of the TLA and TCSA is likely influenced by differences in hydraulic conductivity and inland head gradients. The upward leakage of freshwater into overlying aquifers adds to the freshwater-seawater mixing.

In the model setup, the head value at the inland boundary is the same with depth in the TCSA (Layer 3) because we neglect any water density effects at the landward boundary. However, offshore cells that are filled with seawater create an increasing freshwater-equivalent head with depth. The greater thickness of the TCSA in the offshore region magnifies this effect, causing high equivalent-freshwater heads at the base of the TCSA due to buoyancy (water density) effects. This elongates the wedge of seawater, where seawater pushes further landward in the lower part of the aquifer, while the upper aquifer tends to contain freshwater. That is, the thickness of the TCSA aquifer plays a significant role in shaping the seawater wedge. The flatness of the freshwater-seawater interface is also influenced by the horizontal-to-vertical anisotropy in the hydraulic conductivity, where the vertical hydraulic conductivity is 10% of the horizontal value. This tends to enhance the groundwater flow rates in the horizontal direction, which is expected to "flatten" the seawater wedge. We also expect that in places, karst conduits or other features of higher hydraulic conductivity, such as fractures, modify the seawater wedge shape, as shown by Sebben et al. (2015), who explored the role of fractures on the seawater wedge using a simple hypothetical case study.

The large extent of regions where freshwater overlies saltwater highlights the importance of "saltwater upconing" as a threat to the water quality of pumping wells where these extract freshwater from aquifers with saltwater at greater depths. Images of saltwater upconing were presented experimentally by Werner et al. (2009), while the zone of influence of upconing plumes was explored by Jakovovic et al. (2016). Further investigations are warranted to assess the threat of saltwater upconing, to determine pumping thresholds that avoid upward shifts in the interface that may threaten the viability of pumping wells. The 2D cross-sectional analysis of the current study is not able to properly explore saltwater upconing because of the local scale at which this occurs and the need to assess flow in three dimensions. Thus, local-scale, block models (3D) are needed for this analysis.

Figure H2 demonstrates that, at CSB, seawater occurs 3,176 m inland in the TLA, while the toe in TCSA is located 10,556 m offshore. Thus, there is a substantial offshore freshwater body predicted in the TCSA, with the interface tip extending approximately 24,500 m seaward. Unstable fingers of freshwater are again apparent in the offshore TLA (Figure H2), for reasons explained in the main text for CSE. Figure H2 shows similar patterns of dispersiveness as observed for CSA—that is, a relatively narrow mixing zone in the TLA and a more dispersed interface in the TCSA. The thickness of the TCSA in CSB is smaller than the TCSA of CSA, which leads to smaller equivalent-freshwater heads in the lower aquifer, and consequently, the distance between the toe and the tip of the wedge in CSB is less than that observed in CSA.

Figure H3 shows that at CSC, seawater occurs 2,401 m inland in the TLA and 5,129 m inland in the TCSA. The freshwater head in the model is sufficient to push seawater offshore in the TCSA, with the interface tip predicted to extend approximately 2,972 m offshore. Again, freshwater fingering is apparent in the offshore TLA (Figure H3). Figure H3 reveals dispersive patterns similar to CSA and CSB, with a relatively sharp interface in the TLA and a more dispersive one in the TCSA. The thinner TCSA in CSC yields lower equivalent freshwater heads, resulting in a shorter wedge extent compared to CSA and CSB.

Figure H4 shows seawater wedges with toes extending 3,965 m inland in the TLA and 4,964 m inland in the TCSA. The seawater wedge tip in the TCSA extends approximately 4,512 m inland. Although the equivalent-freshwater heads in the offshore boundary of TCSA are lower than in CSA, CSB and CSC, the inland head within 10 km of the shoreline is also significantly lower (4.6 m AHD). As a result, there is insufficient head to create offshore fresh groundwater in either aquifer (TLA or TCSA). The very thin TCSA in CSD also contributes to the seawater wedge occurrence in that aquifer, creating a shorter seawater wedge extent.

## References

Jakovovic, D., Werner, A.D., de Louw, P.G., Post, V.E., and Morgan, L.K., 2016. Saltwater upconing zone of influence. Advances in Water Resources, 94, 75-86. https://doi.org/10.1016/j.advwatres.2016.05.003

Sebben, M.L., Werner, A.D., and Graf, T., 2015. Seawater intrusion in fractured coastal aquifers: A preliminary numerical investigation using a fractured Henry problem. Advances in Water Resources, 85, 93-108. https://doi.org/10.1016/j.advwatres.2015.09.013

Werner, A.D., Jakovovic, D., and Simmons, C.T., 2009. Experimental observations of saltwater up-coning. Journal of Hydrology, 373(1-2), 230-241. https://doi.org/10.1016/j.jhydrol.2009.05.004

# Appendix I – Comparison of heads: Scenario 1 vs parent modelling results

Figures I1 to I4 compare the head distribution from the density-dependent simulation of pre-development steady-state conditions (Scenario 1) with that of the regional model for CSA, CSB, CSC and CSD, respectively. Note that the heads are reported relative to the salinity of the cell. That is, if the cell contains seawater (which is the case for much of the offshore aquifers), then the head represents the height of a column of seawater above that cell. That is, if the reported head is $h$, and the density of groundwater in the cell is $\rho$, then the pressure in the cell is $P = \rho g h$, where $g$ is gravitational acceleration.

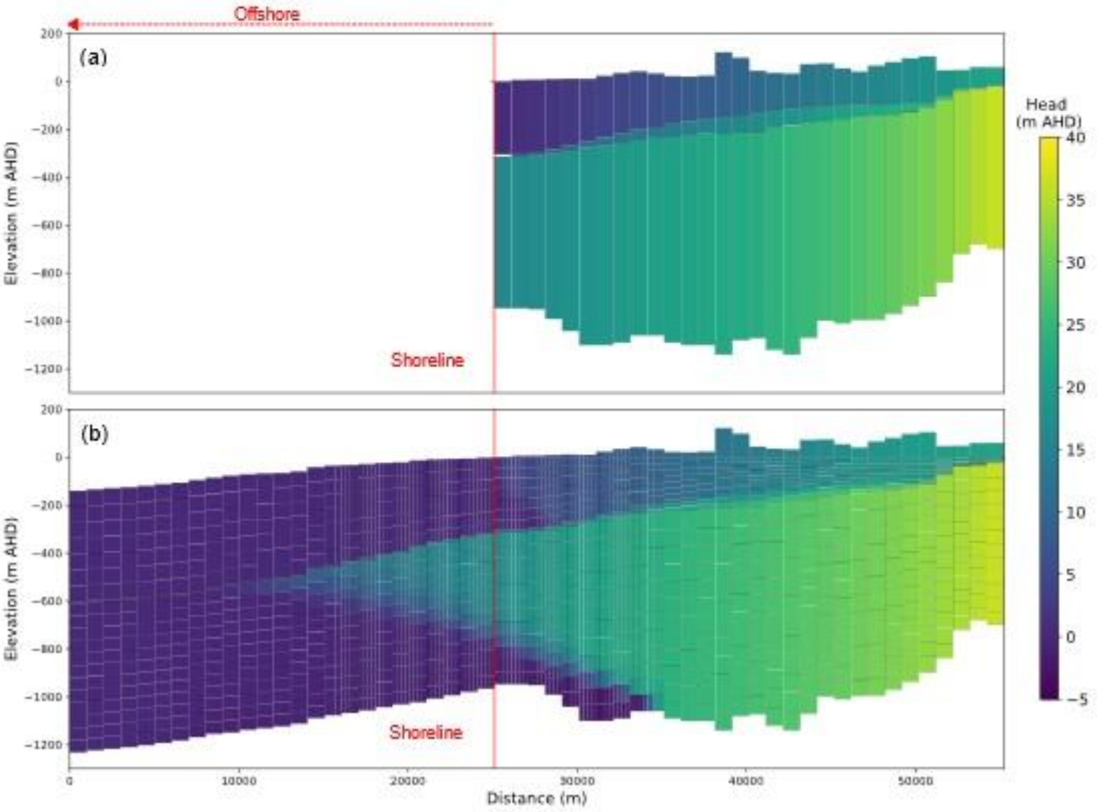

**Figure I1.** Comparison of heads between: (a) the parent model of Morgan et al. (2015), and (b) cross section A (CSA) (density-dependent, steady-state, pre-development simulation of freshwater-seawater interactions). The white cell in (a), located near the shoreline, belongs to Layer 2 (aquitard), and represents an inactive cell at the shoreline in the regional model.

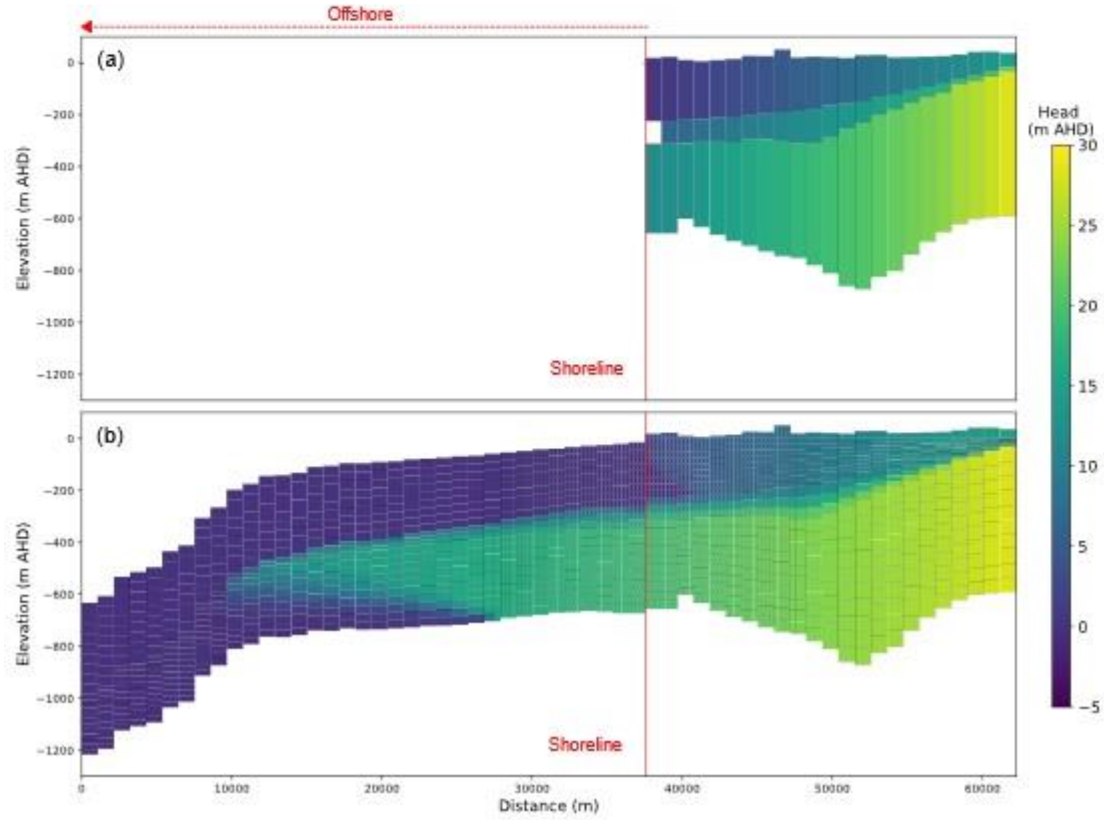

**Figure I2.** Comparison of heads between: (a) the parent model of Morgan et al. (2015), and (b) cross section B (CSB) (density-dependent, steady-state, pre-development simulation of freshwater-seawater interactions). The white cell in (a), located near the shoreline, belongs to Layer 2 (aquitard), and represents an inactive cell at the shoreline in the regional model.

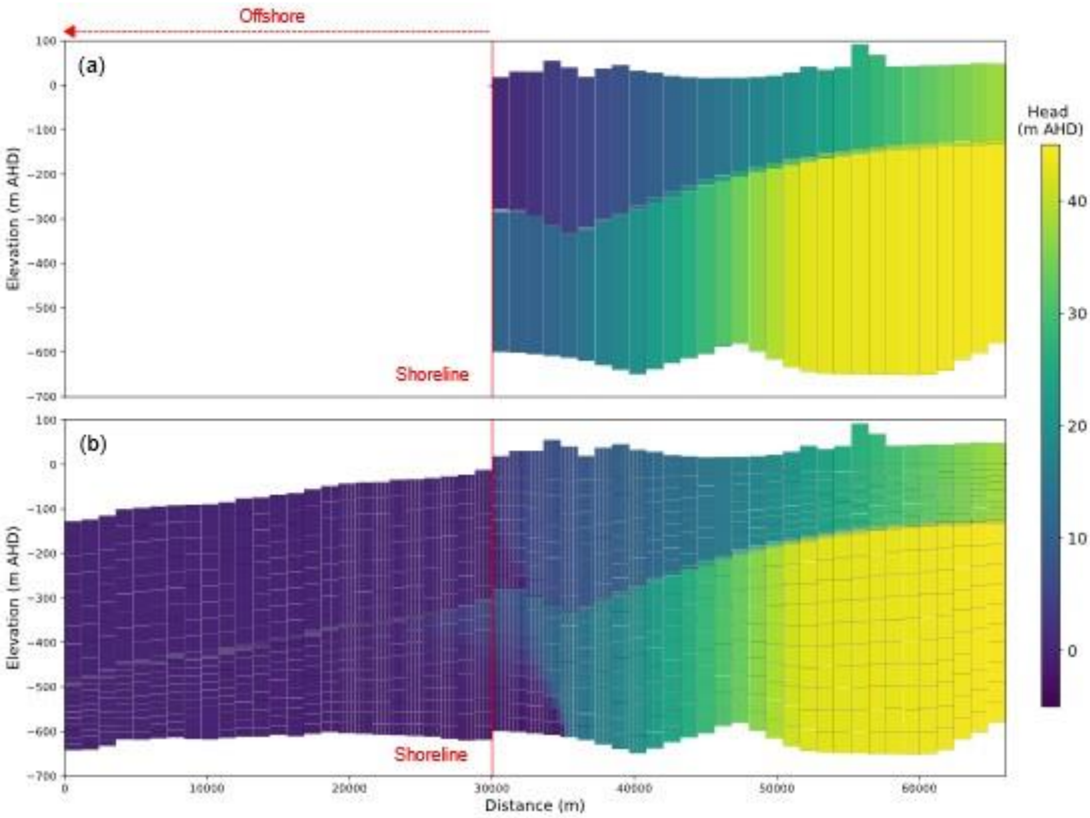

**Figure I3.** Comparison of heads between: (a) the parent model of Morgan et al. (2015), and (b) cross section C (CSC) (density-dependent, steady-state, pre-development simulation of freshwater-seawater interactions). The white cell in (a), located near the shoreline, belongs to Layer 2 (aquitard), and represents an inactive cell at the shoreline in the regional model.

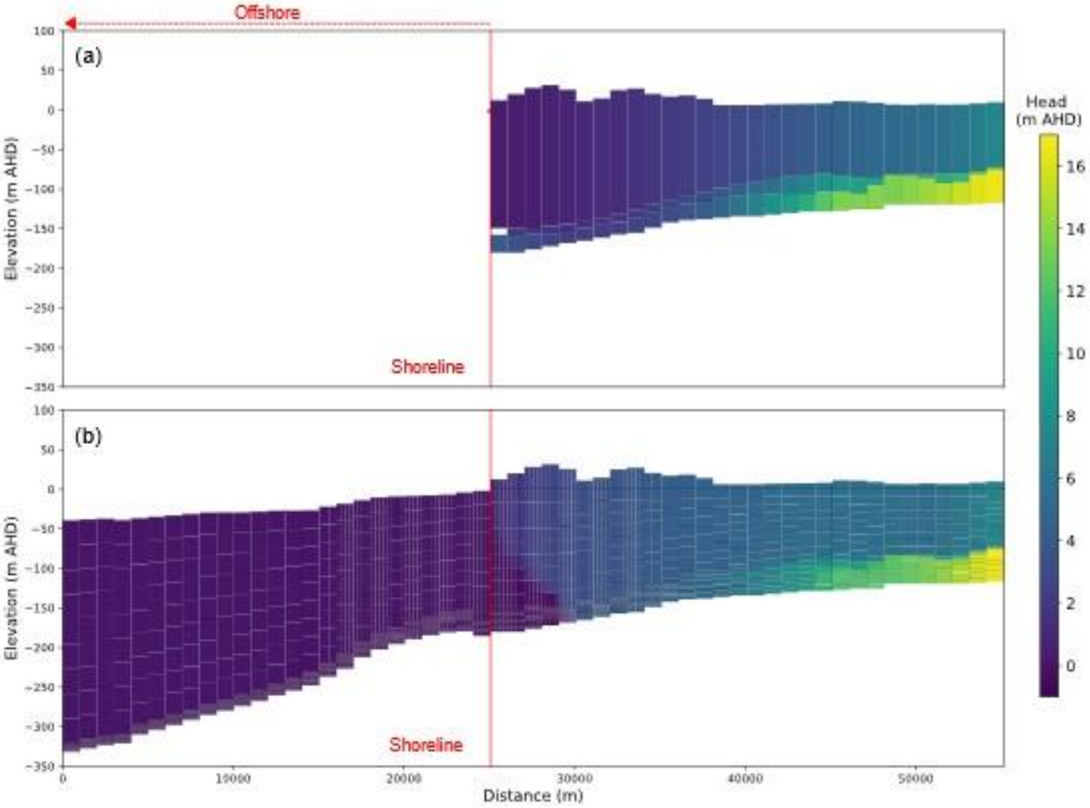

**Figure I4.** Comparison of heads between: (a) the parent model of Morgan et al. (2015), and (b) cross section D (CSD) (density-dependent, steady-state, pre-development simulation of freshwater-seawater interactions). The white cell in (a), located near the shoreline, belongs to Layer 2 (aquitard), and represents an inactive cell at the shoreline in the regional model.

As mentioned above, in the seawater zone, heads are reported by SEAWAT as relative to the salinity of each cell, meaning that a head in a seawater-filled cell leads to a higher pressure than the same head in a freshwater-filled cell due to the greater density of seawater. Therefore, salinity effects must be considered when comparing heads in seawater intrusion models to those in freshwater-only models. Since cells of the onshore aquifer, near the coast, contain seawater in cross sections CSA, CSB, CSC and CSD, this modifies the reported head distribution in a significant number of cells within these cross sections. This is the reason for differences between the heads of the two models in the lower parts of both aquifers near the coast, where the seawater wedge is found. This is apparent from the wedge-shaped zones of darker-coloured (lower) heads near the base of aquifers, where seawater occurs as shown in the previous Appendix.

The match between the cross-sectional model and the parent model is not perfect, but it is sufficiently good to demonstrate that the strategy developed for extracting cross sections from Morgan et al. (2015)—and incorporating solute transport and density effects—was reasonable. The differences between the cross-sectional and parent models may arise from several sources: (1) differences between 2D and 3D representations (i.e., perpendicular flow components are eliminated in the cross-sectional model), (2) averaging of the aquifer properties from the regional model in assigning parameters to cross sections (see Appendix A), (3) replacing the constant-head boundary used in Morgan et al. (2015) with a representation of the offshore aquifer, and (4) the addition of solute transport and density-dependent processes.

## References

Morgan, L.K., Harrington, N., Werner, A.D., Hutson, J.L., Woods, J., and Knowling, M.J., 2015. South East regional water balance project–Phase 2. Development of a regional groundwater flow model. Technical Report Series No. 15/38, 142 p. https://goyderinstitute.org/wp-content/uploads/2023/06/goyder_trs_15-38_south_east_regional_water_balance_phase_2.pdf (Accessed November 04, 2024).

# Appendix J – Transient salinity distribution: Scenario 2

Figures J1 to J4 illustrate the freshwater-seawater distribution at the conclusion of Scenario 2 - the transient simulation (1970–2013) – showing the results for CSA, CSB, CSC and CSD, respectively. The toe locations in CSA, CSB, CSC and CSD (Figures J1 to J4) at the end of the 44-year simulation period can be compared to the pre-development conditions (see Figures H1 to H4) to assess seawater intrusion (SWI) or seawater retreat (the seaward movement of seawater in the aquifer) that was simulated to occur during 1970–2013. For these purposes, the respective to locations are included in Tables 2 and 3 of the main body of the report.

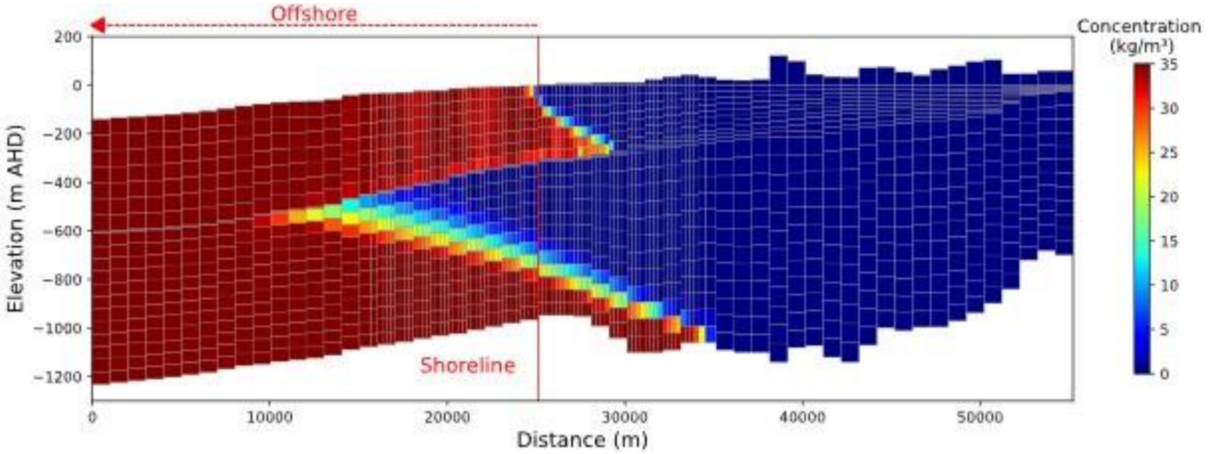

**Figure J1.** Spatial distribution of salinity at cross section A (CSA) at the end of the transient simulation (1970–2013).

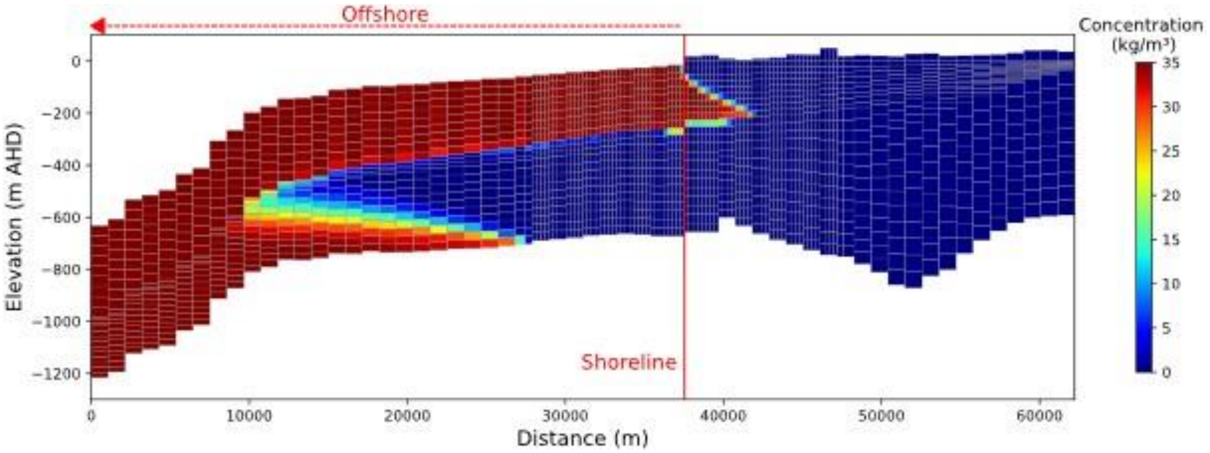

**Figure J2.** Spatial distribution of salinity at cross section B (CSB) at the end of the transient simulation (1970–2013).

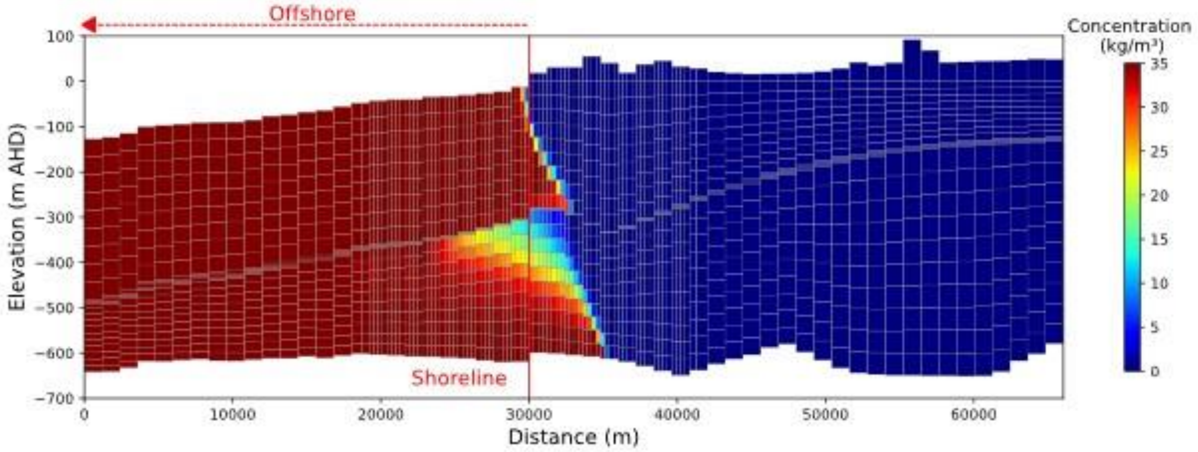

**Figure J3.** Spatial distribution of salinity at cross section C (CSC) at the end of the transient simulation (1970–2013).

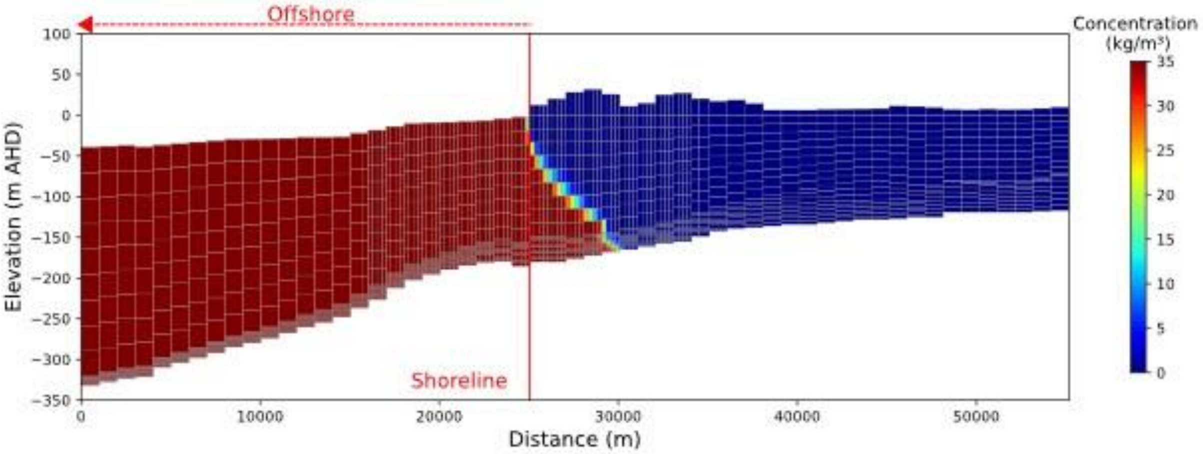

**Figure J4.** Spatial distribution of salinity at cross section D (CSD) at the end of the transient simulation (1970–2013).

The transient simulations allow for an assessment of the movement in the freshwater-seawater interface during the 44-year period of the regional model simulation. Where the heads have declined during 1970–2013, there is expected to be an inland shift in the extent of seawater, although there is commonly a time lag between aquifer water level changes and SWI that is difficult to predict without the modelling undertaken here. For CSA, the model predicts that the seawater toe advanced 855 m inland (movements in the toe are typically considered to be the length scale of SWI) during the simulation period in the upper aquifer (TLA), where it reached 4,036 m inland from the shoreline by 2013. In the lower aquifer (TCSA), SWI was far less extensive, with a landward toe shift of only 15 m, reaching 9,359 m onshore from the shoreline in the lower aquifer. The inland movement of the seawater toe in the TLA of CSA can be attributed to a head drop of approximately 1 m (at 5 km inland from the shoreline) during the transient period (1970–2013) (see Figure K1), combined with the high hydraulic conductivity of the aquifer (approximately 115 m/d near the coast). The much lower hydraulic conductivity of the lower aquifer (around 3 m/d near the coastline) limited the inland movement of the toe in the TCSA of CSA, noting that the head drop was higher in the TCSA than in the TLA (2-m head drop in the TCSA at around 11 km from the shoreline) over the same period (see Figure K1). It follows that the seawater wedge in the TCSA is unlikely to have reached a new equilibrium because the lower hydraulic conductivity causes slower seawater movements in response to head changes.

In CSB, the simulated seawater toe advanced 1,105 m further inland during 1970–2013, reaching 4,281 m onshore from the shoreline in the TLA. The TCSA also experienced SWI but to a much lesser degree, with a landward toe shift of only 13 m, becoming 10,543 m offshore in the TCSA. Again, similar to CSA, the greater inland movement of the toe in the TLA of CSB can be explained by the higher hydraulic conductivity of the TLA (approximately 115 m/d near the coast) versus the lower value (around 3 m/d) in the TCSA. This is despite a small head drop—about 1 m located 5 km inland from the shoreline – in the TLA during the transient period (1970–2013) (see Figure K2), while the TCSA of CSB had a steeper head drop of approximately 2 m at 10 km from the shoreline (see Figure K2).

In CSC, the seawater toe advanced 333 m further inland during the historical period of simulation, reaching 2,734 m onshore in the TLA. The landward movement of the toe in the TCSA was again much lower (around 12 m) in the TCSA, ending up at 5,141 m onshore in the TCSA. The same contrasts in the TLA/TCSA head drop and hydraulic conductivity apply to CSC as they do to CSA and CSB, with a 0.5-m head decline at 5 km inland in the TLA (with hydraulic conductivity 0f 115 m/d), while the TCSA had a head drop of about 1 m at 6 km inland (with hydraulic conductivity of around 3 m/d).

In CSD, the toe advanced 206 m further inland during the modelled period of 1970–2013, reaching 4,171 m onshore in the TLA. The TCSA experienced only a 1 m landward shift during the same period – with similar head and hydraulic conductivity contrasts occurring as described above for CSA-CSC.

# Appendix K – Comparison of head distributions: Pre-development conditions vs end-of-transient simulations (1970–2013)

Figures K1 to K4 show the difference in head values between the pre-development steady-state condition and the end of the transient simulation (1970–2013) for CSA, CSB, CSC and CSD, respectively.

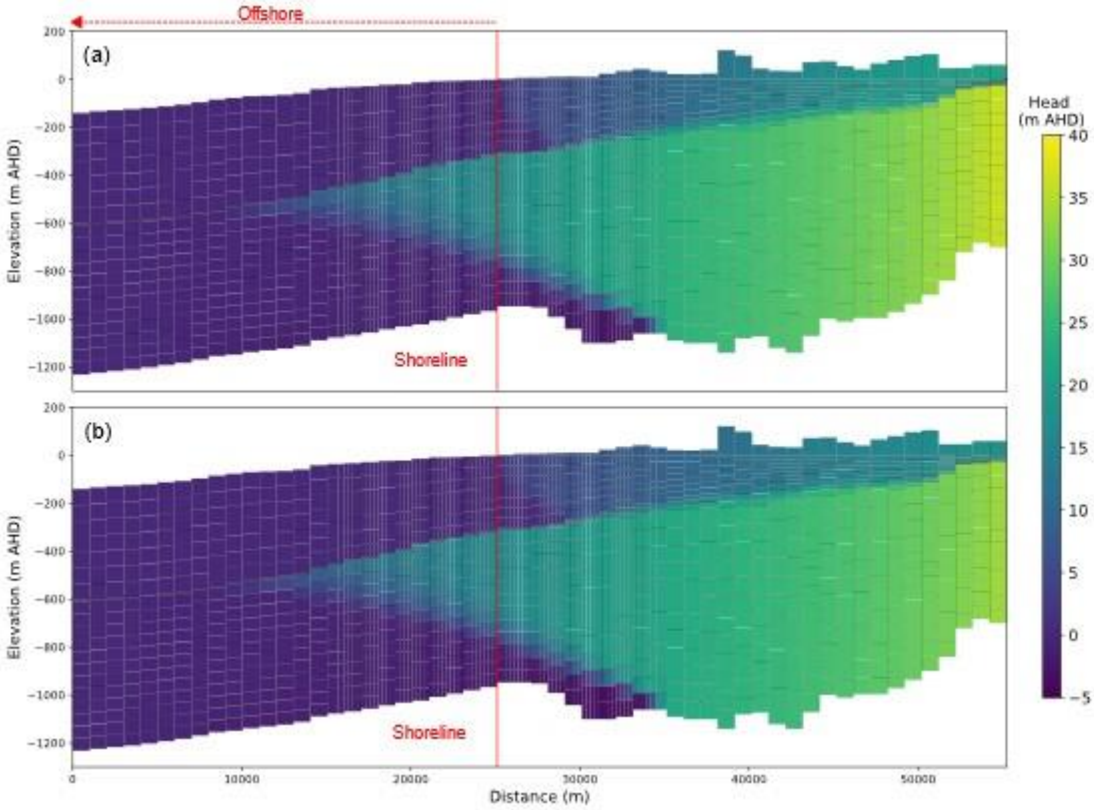

**Figure K1**. Head distributions during the transient simulation period (1970–2013) within cross section A (CSA), showing: (a) head distribution under pre-development conditions, and (b) head distribution at the end of the transient simulation (1970–2013).

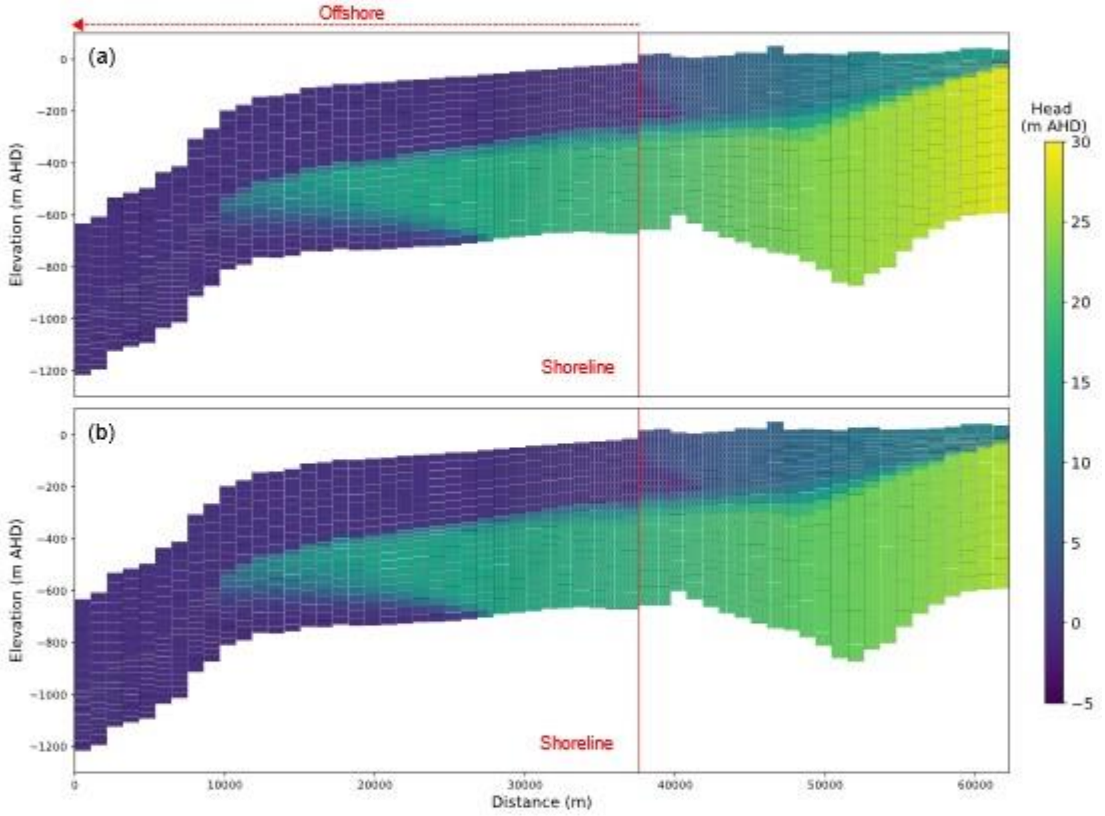

**Figure K2.** Head distributions during the transient simulation period (1970–2013) within cross section B (CSB), showing: (a) head distribution under pre-development conditions, and (b) head distribution at the end of the transient simulation (1970–2013).

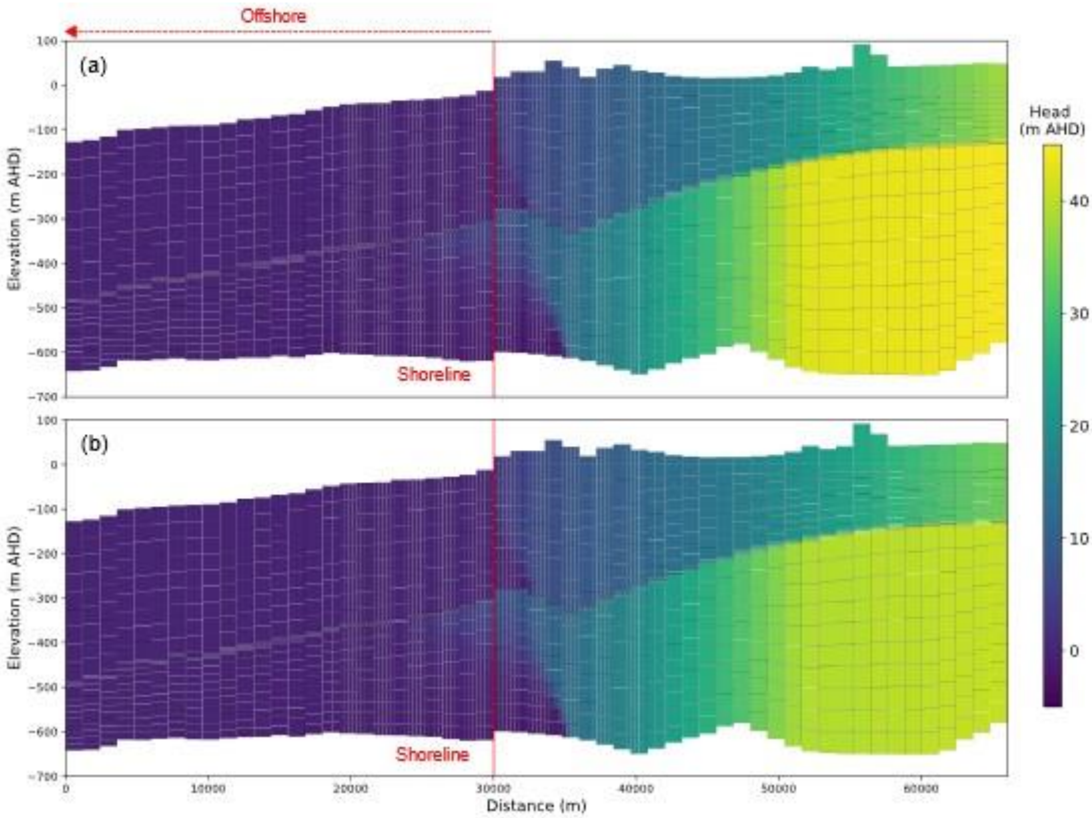

**Figure K3.** Head distributions during the transient simulation period (1970–2013) within cross section C (CSC), showing: (a) head distribution under pre-development conditions, and (b) head distribution at the end of the transient simulation (1970–2013).

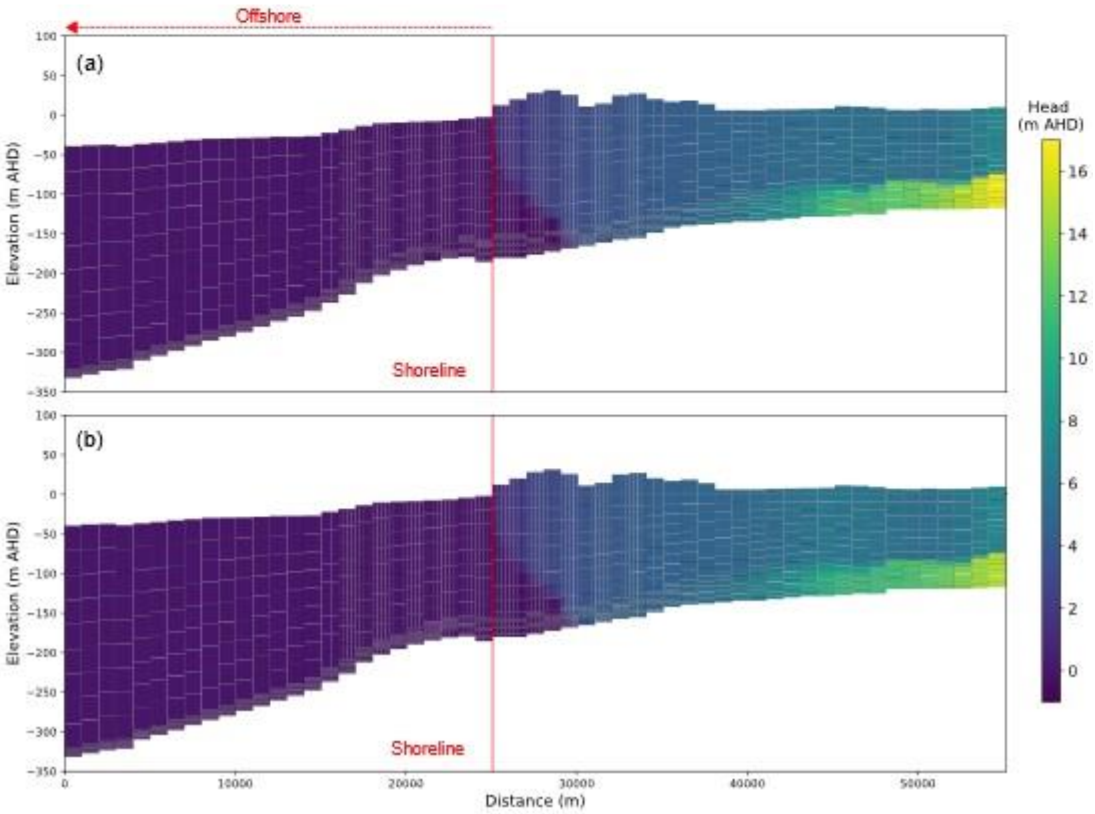

**Figure K4.** Head distributions during the transient simulation period (1970–2013) within cross section D (CSD), showing: (a) head distribution under pre-development conditions, and (b) head distribution at the end of the transient simulation (1970–2013).

The above figures show relatively small differences (compared to the spatial differences) in the head between the pre-development, steady-state conditions and the end of the transient simulation (1970–2013), although the large range of the colour scale makes it challenging to see small variations. Where head changes are apparent, a drop in head occurred, as described in the previous Appendix. As described in Appendix I, the seawater wedge affects the occurrence and reporting of heads, and so, head changes due to shifts in the distribution of seawater were effectively discounted in interpreting the presented results.

# Appendix L – Field salinities

As discussed in Section 3.2.3 of the main report, field observations of groundwater salinity are the primary indicator of seawater intrusion (SWI) in coastal aquifers, and are an important check on the predictions of SWI models, i.e., to assess whether models are producing reasonable predictions of the seawater extent in coastal aquifers. Werner and Gallagher (2006) describe the first attempt at modelling regional-scale SWI in an Australian context (the Pioneer Valley, Queensland), along with comparisons to field measurements. In the Pioneer Valley, a dedicated SWI monitoring network had been installed following the salinization of groundwater wells in the previous decades. We attempt here to explore well salinities in the study area, at least insomuch as reporting groundwater salinities from available monitoring records. The current evaluation of measured salinities from wells in the Limestone Coast is complementary to the airborne electromagnetic survey that was undertaken concurrently with the modelling described herein. Figures L1 to L3 display the distributions of wells for which electrical conductivity (EC) data are available, near CSA, CSB, CSC and CSD.

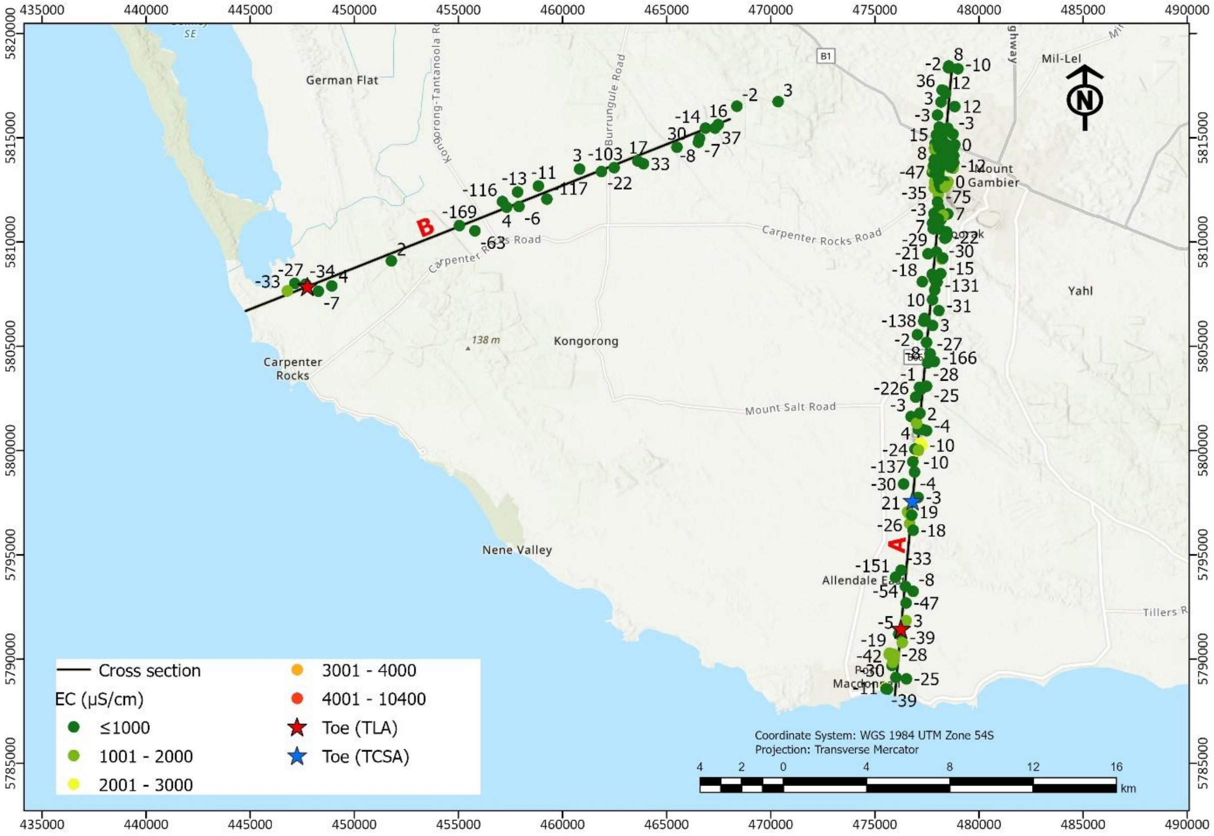

**Figure L1.** Location of wells with salinity data proximal to CSA and CSB for the TLA (upper) aquifer. The numbers next to wells indicate the elevation of the bottom of the wells, rounded to the nearest integer, in m AHD, where 0 m AHD is sea level. The tip of the seawater wedge in the TLA is approximately at the shoreline. The toe locations for both the TLA and TCSA are shown by the red and blue stars, although the TCSA toe at CSB is omitted because it is offshore. Toe locations were taken from pre-development conditions (see Figures H1 and H2).

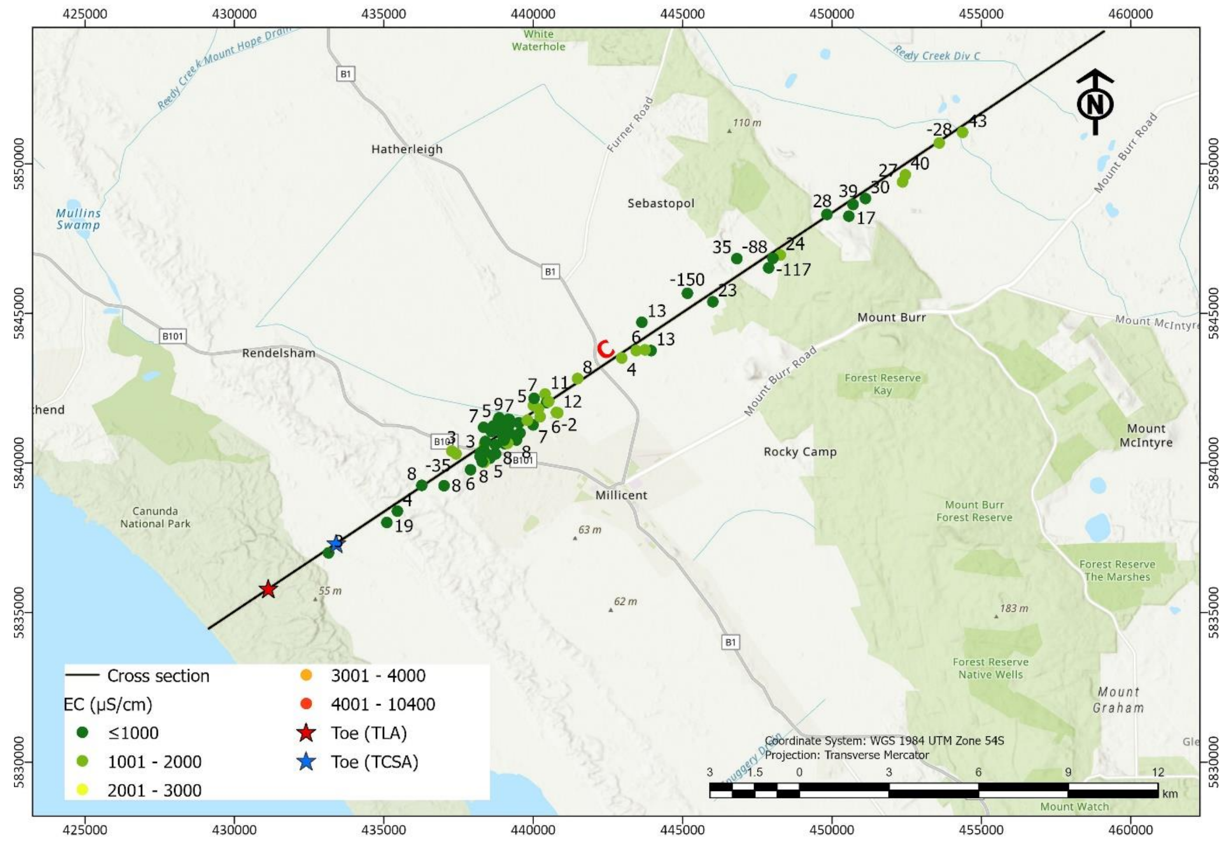

**Figure L2.** Location of wells with salinity data proximal to CSC for the TLA (upper) aquifer. The numbers next to wells indicate the elevation of the bottom of the wells, rounded to the nearest integer, in m AHD, where 0 m AHD is sea level. The tip of the seawater wedge in the TLA is approximately at the shoreline. The toe locations for both the TLA and TCSA are shown by the red and blue stars. Toe locations were taken from pre-development conditions (see Figure H3).

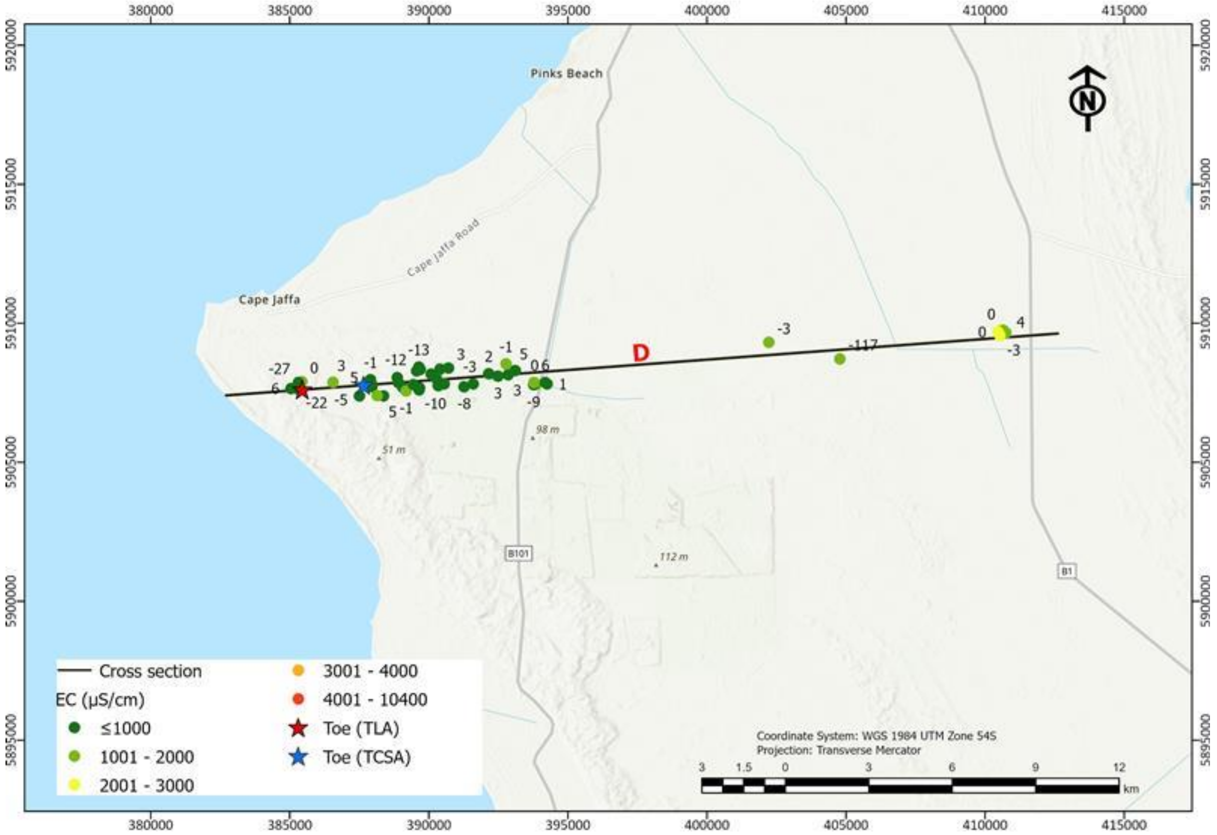

**Figure L3.** Location of wells with salinity data proximal to CSD for the TLA (upper) aquifer. The numbers next to wells indicate the elevation of the bottom of the wells, rounded to the nearest integer, in m AHD, where 0 m AHD is sea level. The tip of the seawater wedge in the TLA is approximately at the shoreline. The toe locations for both the TLA and TCSA are shown by the red and blue stars. Toe locations were taken from pre-development conditions (see Figure H4).

Only EC data for the upper aquifer (TLA) are available at the locations of CSA, CSB, CSC and CSD, likely because the vast majority of pumping wells in the Limestone Coast draw from the TLA. The simulated toe location (from the pre-development, steady-state model) is shown in Figures L1 to L3 for both the upper and lower aquifers at CSA, CSC and CSD. For CSB, however, only the toe location for the TLA is shown, as the toe of the lower aquifer (TCSA) (from the pre-development, steady-state model) is located in the offshore part of this cross section (Figure L1). Appendix H shows the salinity distributions leading to the tip and toe locations given in Figures L1-L3. The tip and toe positions in each cross section at the end of the transient simulation (1970–2013) and under future steady-state conditions are presented in Appendices M, N, O and P.

Although some wells in this area are deep enough (i.e., with the well bottom located below mean sea level) to potentially provide insight into the extent of seawater in the aquifer, none of the wells reach the base of the TLA in regions where seawater is predicted to occur according to cross-sectional modelling results. Thus, field measurements of salinity provide minimal guidance on the extent of seawater in the aquifer, at least at the modelling sites. Wells that reach the aquifer base would be required to observe the seawater extent in the aquifer and any shifts in the freshwater-seawater interface, from which extrapolation of movements of the seawater toe could be inferred (and compared to the results of the current modelling analysis). The well salinity data along CSA, CSB, CSC and CSD that are available indicate relatively fresh groundwater (in the upper part of the aquifer), with EC values below 2,000 µS/cm (Figures L1 to L3). As such, we consider that Figures L1 to L3 show salinities that do not conflict with modelling results; although, there is insufficient deep-well measurements to make assertions as to the accuracy of the cross-sectional SWI models from salinity measurements in the vicinity of CSA, CSB, CSC and CSD.

## References

Werner, A.D., and Gallagher, M.R. 2006. Characterisation of sea-water intrusion in the Pioneer Valley, Australia using hydrochemistry and three-dimensional numerical modelling. Hydrogeology Journal, 14, 1452-1469. https://doi.org/10.1007/s10040-006-0059-7

# Appendix M – Prediction of long-term seawater intrusion caused by the continuation of 2013 pumping rates (Scenario 3a)

Figures M1 to M4 show salinity distributions resulting from the steady-state simulation of "future conditions" at CSA, CSB, CSC and CSD (respectively). Here, "future conditions" refer to steady-state conditions obtained from long-term simulations using average recharge and evapotranspiration over the 2004–2013 period, with pumping applied as a constant value representative of average rates for 2013. The intent of this scenario is to assess the future landward extent of seawater should the pumping of 2013 and the average climate stresses of 2004–2013 be continued indefinitely. Steady-state conditions are achieved in SEAWAT by time-marching, whereby transient models (with simulation periods of 30,000 years) were continued until the seawater wedge reached a new, stable condition, and therefore, we refer to this and the scenarios that follow as "long-term seawater intrusion". We have not explored the time-scales for future seawater intrusion (SWI) to occur here, and rather, this scenario offers the "final future condition" for the seawater extent under 2013 stresses. The stresses of 2013 were because these represent the most up-to-date regional-scale, model-ready dataset that was accessible for cross-sectional SWI modelling at the time of this study. This scenario also serves as the baseline for evaluating the impacts of sea-level rise (Scenario 3b; Appendix N), changes in recharge (Scenario 3c; Appendix O), and increased groundwater pumping (Scenario 3d; Appendix P).

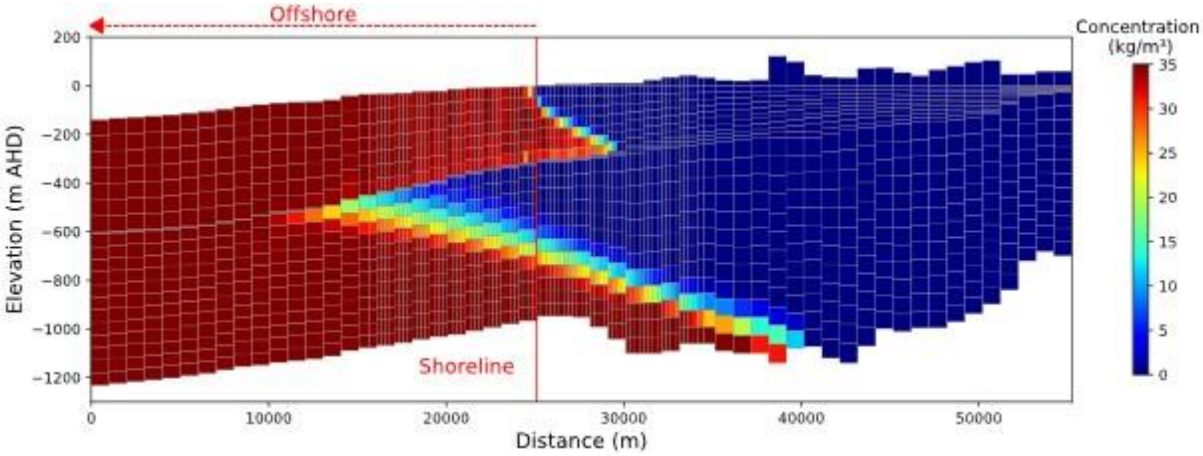

**Figure M1.** The salinity distribution arising from the steady-state simulation of future conditions at CSA, arising when pumping stresses in 2013 and the average recharge of 2004–2013 are applied for a prolonged (future) period of time.

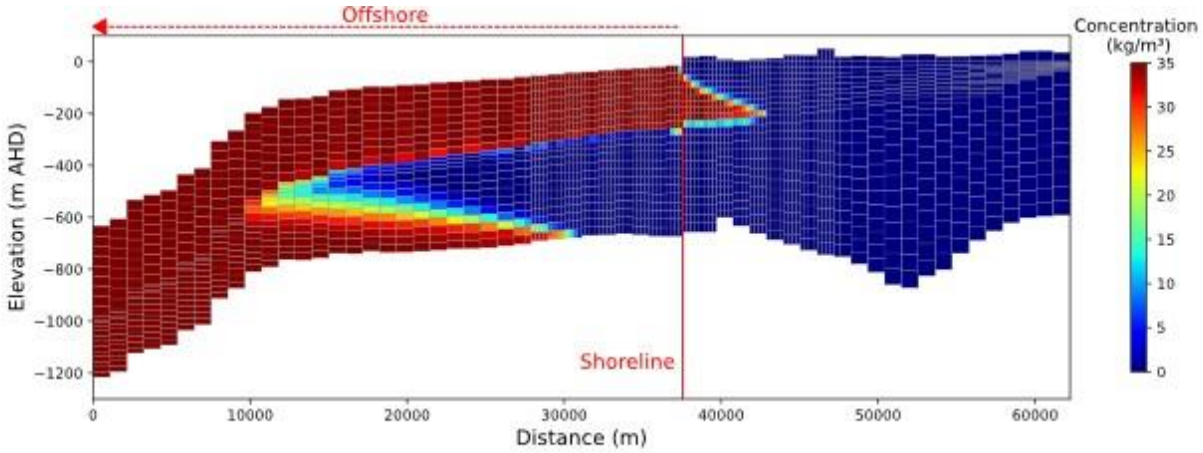

**Figure M2.** The salinity distribution arising from the steady-state simulation of future conditions at CSB, arising when pumping stresses in 2013 and the average recharge of 2004–2013 are applied for a prolonged (future) period of time.

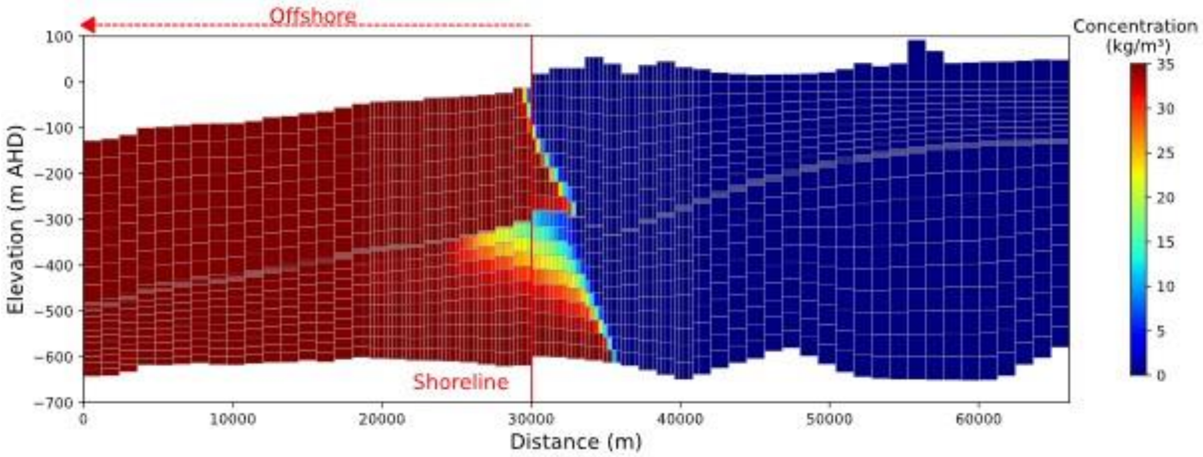

**Figure M3.** The salinity distribution arising from the steady-state simulation of future conditions at CSC, arising when pumping stresses in 2013 and the average recharge of 2004–2013 are applied for a prolonged (future) period of time.

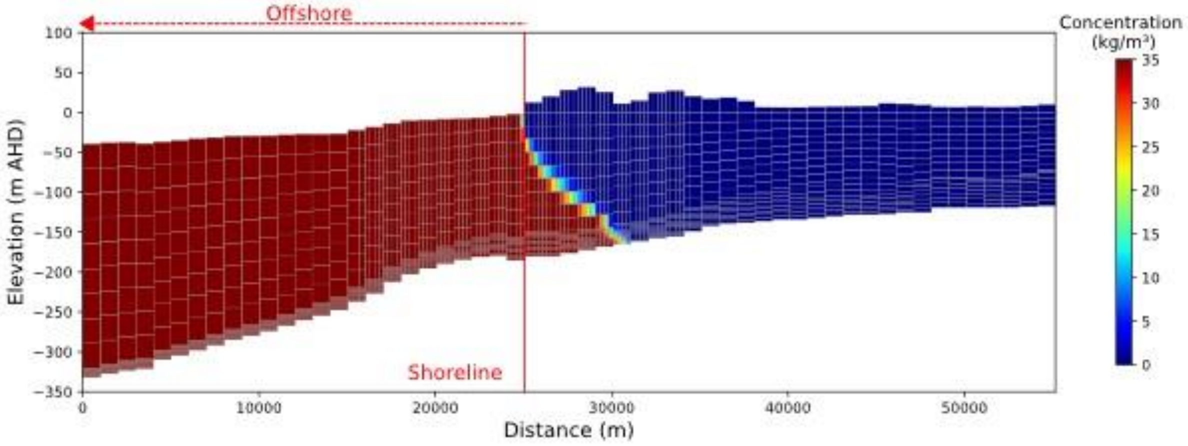

**Figure M4.** The salinity distribution arising from the steady-state simulation of future conditions at CSD, arising when pumping stresses in 2013 and the average recharge of 2004–2013 are applied for a prolonged (future) period of time.

Figure M1 demonstrates that, at CSA, the seawater toe occurs 4,207 m onshore (landward of the shoreline) in the upper aquifer (TLA) and 14,250 m onshore in the lower aquifer (TCSA) once the new steady-state condition is reached. The simulated results also indicate that, compared to the end of the transient simulation (1970–2013), the seawater toe moved 171 m further inland in the TLA and 4,891 m further inland in the TCSA at CSA, once the coastal aquifer transitioned to the new steady-state conditions. This compares to the 855 m landward shift in the toe in the TLA and 15 m in the TCSA that occurring during 1970–2013. That is, a much smaller movement of the toe is expected to occur in the TLA subsequent to 2013, relative to the predicted extent of SWI over the 44 years prior to 2013. The opposite occurs in the TCSA, in which considerable SWI is anticipated post-2013. This result is attributable to the difference in the TLA and TCSA hydraulic conductivity values, whereby the TLA is closer to a new steady-state condition at the end of the 1970–2013 simulation due to the higher hydraulic conductivity (approximately 115 m/d near the coast), whereas the TCSA requires considerable additional time to transition to a new steady-state because the hydraulic conductivity is relatively low (about 3 m/d near the coast). The landward movement of the seawater wedge toe of almost 5 km in the TCSA highlights the unstable conditions of the lower aquifer and the propensity for its future salinization, albeit this may take centuries to develop. A more rigorous assessment of the time-variance of SWI in the lower aquifer is warranted in future analyses.

Figure M2 shows that, at CSB, the seawater toe occurs 5,242 m onshore in the TLA, while the toe in TCSA is located 7,339 m offshore (seaward of the shoreline) in the steady-state results (representing future conditions under 2013 pumping rates). In CSB, the simulated results show that the toe moved 961 m further inland in the TLA and 3,204 m landward in the TCSA between the end of the transient simulation (1970–2013) and the new steady-state condition, due to the future continuation of 2013 pumping. These values compare to the 1,105 m landward shift of the toe in the TLA and the 13 m shift in the TCSA during 1970–2013, such that a slightly smaller toe movement is expected in the TLA after 2013, while a much greater movement is anticipated in the TCSA. This is roughly consistent with the general trend of observed toe movements at CSA, although future SWI in the TLA is likely to be much greater at CSB than at CSA.

Figure M3 illustrates that, at CSC, the seawater toe occurs 2,802 m onshore in the TLA and 5,473 m onshore in the TCSA in the steady-state case representing the continuation of 2013 pumping. In CSC, the seawater toe moved 68 m further inland in the TLA and 332 m further inland in the TCSA due to the long-term effects of 2013 rates of pumping. Following the 333 m landward shift of the toe in the TLA and the 12 m shift in the TCSA between 1970 and 2013, the TLA is expected to experience only minor toe movement after 2013, whereas a significantly greater shift is anticipated in the TCSA, similar to the above-mentioned cross sections.

Figure M4 indicates that, at CSD, the seawater toe occurs 4,607 m onshore in the TLA and 5,702 m onshore in the TCSA in the steady-state case described here. In CSD, the seawater toe shifted 436 m further inland in the TLA and 737 m further inland in the TCSA following 2013 and once a new steady state was reached. In contrast to the 206 m landward toe shift in the TLA and the 1 m shift in the TCSA observed between 1970 and 2013, both the TLA and TCSA are projected to undergo greater toe movements after 2013, which differs to the situation for the above-mentioned cross sections.

It appears that the largest predicted movements in the toe within the TLA, arising from the continuation of conditions in 2013, occurred in CSB, while the smallest TLA toe movement was simulated to occur at CSE. This can be attributed to several factors. For example, pumping rates from 2013 differ significantly in space. In some places, pumping in 2013 differs to pumping that occurred over the 1970–2013 period. That is, in some cross sections, 2013 pumping was much higher than previous years, while in others, it remained comparable. For cases where 2013 pumping was higher, SWI is expected to be greater after 2013 relative to the prior period (1970–2013). Similarly, the average heads from 2004–2013 used to define the inland boundary condition differ from the longer-term head trends (1970–2013), and these differences vary between cross sections. Additionally, variations in the geometry, hydraulic conductivity and configuration (e.g., the alignment of the cross section relative to the regional head distributions) of the cross sections influence how each responds to head declines and saltwater intrusion processes. Another contributing factor is the variation in average recharge (2004–2013) across the cross sections. Each cross section exhibited a distinct recharge trend over the broader 1970–2013 period. In some locations, recharge during the 2004–2013 period was relatively high compared to earlier years. In contrast, other cross sections experienced declining recharge during this time. When the recharge of 2004–2013 was used to find a new steady-state condition, it affected the long-term toe location.

For the TCSA, the largest toe movement was predicted at CSA, while the smallest was simulated at CSE. This can be attributed to two main factors: (a) the average heads from 2004–2013 used to define the inland boundary condition differ from the longer-term head trends observed between 1970 and 2013, with these differences varying between cross sections; (b) the geometry, hydraulic conductivity and configuration of the cross sections themselves influence how each responds to head declines and the progression of SWI.

# Appendix N – Prediction of long-term seawater intrusion caused by sea-level rise of 300 mm (Scenario 3b)

Scenario 3b involves a rise in the sea level of 0.3 m that occurs instantaneously in 2013, leading to seawater intrusion (SWI) in a protracted period (i.e., until a new steady-state condition is reached) thereafter. There is no land inundation accompanying sea-level rise and the aquifer recharge assumes the average value of 2004–2013 from the regional model of Morgan et al. (2015). Pumping is taken as the average values of 2013, as adopted in Scenario 3a (Appendix M). Section 2.5 of the main report provides a more detailed explanation of this scenario. Figures N1 to N4 show the steady-state distribution of salinity for CSA, CSB, CSC and CSD (respectively) following sea-level rise.

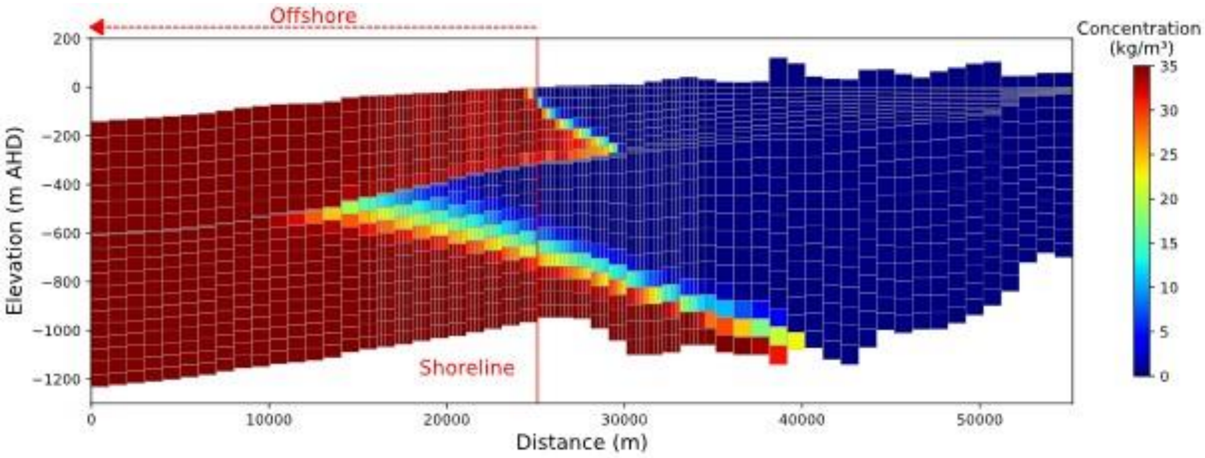

**Figure N1.** Steady-state distribution of salinity at CSA following sea-level rise of 300 mm occurring instantaneously in 2013.

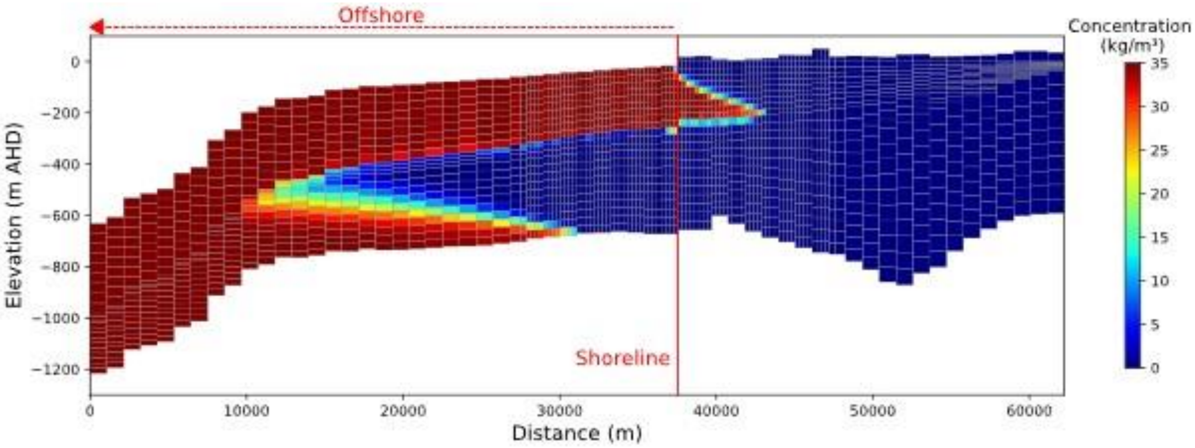

**Figure N2.** Steady-state distribution of salinity at CSB following sea-level rise of 300 mm occurring instantaneously in 2013.

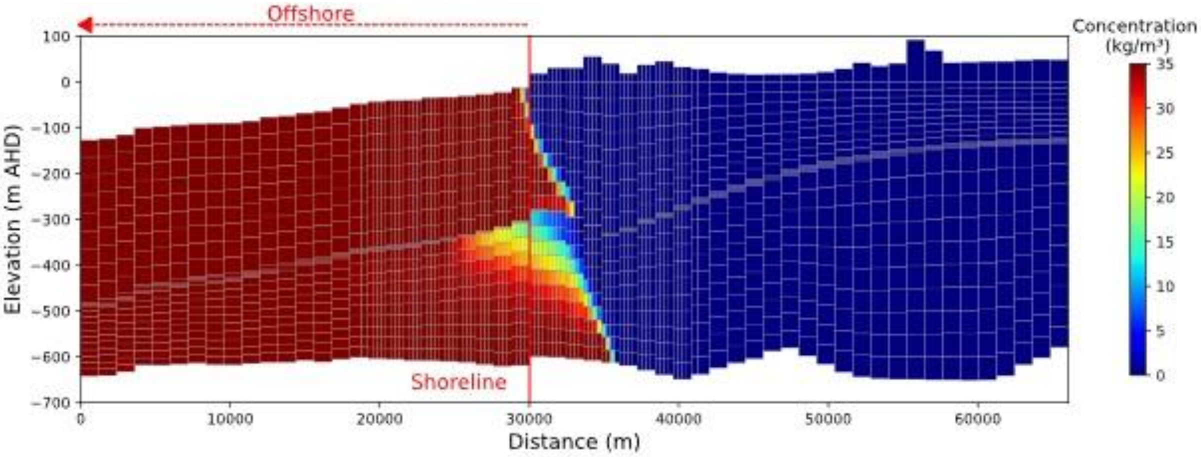

**Figure N3.** Steady-state distribution of salinity at CSC following sea-level rise of 300 mm occurring instantaneously in 2013.

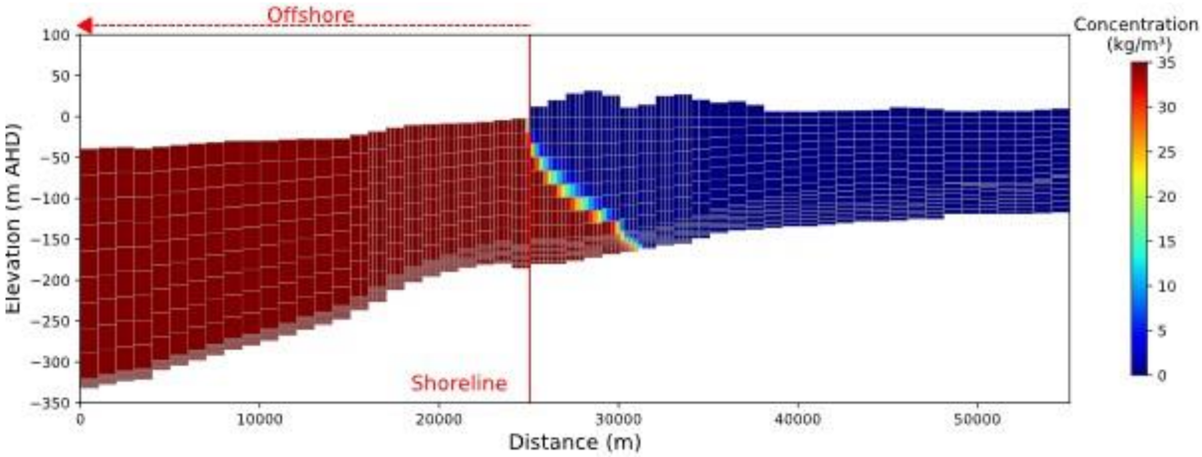

**Figure N4.** Steady-state distribution of salinity at CSD following sea-level rise of 300 mm occurring instantaneously in 2013.

The seawater extent in Figure N1 was compared to that of Figure M1 to assess the net effect of sea-level rise at CSA. Compared to the steady-state simulation of Scenario 3a, the seawater toe advances 86 m further inland (i.e., due to sea-level rise), reaching 4,293 m onshore from the shoreline in the upper aquifer (TLA), and shifts 535 m further inland (i.e., from sea-level rise), reaching 14,785 m onshore from the shoreline in the lower aquifer (TCSA) at CSA.

Figure N2 shows that, the toe advances 164 m further inland (due to sea-level rise) at CSB, reaching 5,406 m onshore from the shoreline in the TLA, and moves 469 m landward (attributable to sea-level rise) in the TCSA where it reaches 6,870 m offshore.

Figure N3 illustrates that, at CSC, sea-level rise causes the toe to advance 124 m further inland, reaching 2,926 m onshore from the shoreline in the TLA, while the toe advances 52 m further inland in the TCSA, reaching an inland distance of 5,525 m.

In Figure N4, at CSD, the toe shifts 391 m further inland from sea-level rise, reaching 4,998 m onshore in the TLA, and shifts 390 m further inland in the TCSA (from sea-level rise), extending to 6,092 m onshore.

A sea-level rise of 0.3 m resulted in increases in the groundwater head across all cross sections, as expected. In CSA, the head increased by 0.25 m at 5 km from the shoreline in the TLA and by 0.14 m at 10 km inland in the TCSA. For CSB, the head increases were 0.21 m at 5 km in the TLA and 0.08 m at 10 km in the TCSA. In CSC, the head rose by 0.21 m at 5 km in the TLA and 0.16 m at 10 km in the TCSA. In CSD, the head increased by 0.21 m at 5 km in the TLA and 0.11 m at 10 km in the TCSA. The rise in the groundwater head inland from the coast is less than sea-level rise because groundwater-level rise, driven by the increase in the head of the sea, is buffered by increasing evapotranspiration and outflows to surface water bodies as the watertable shifts closer to the land surface. This is inherent in the equations that control groundwater-surface water interactions and groundwater evapotranspiration in MODFLOW. The closer the groundwater level rise is to the sea-level rise (0.3 m), the less SWI is expected to occur at that location, because if the groundwater head rises commensurate with sea-level rise, the head gradient is effectively unchanged and the head opposing the penetration of seawater is higher than it would otherwise be in cases where the groundwater level rise is less than sea-level rise. Indeed, the difference between 0.3 m (sea-level rise) and the increase in head in the TLA or TCSA aquifers is something akin to a drawdown in the aquifer due to sea-level rise. For example, if the ocean rises by 0.3 m, and the groundwater head rises by only 0.2 m in response, the groundwater head is effectively 0.1 m lower relative to sea-level than it was before sea-level rise occurred.

Comparison between the five cross sections shows that the lowest and highest seawater wedge movements in the TLA, due to sea-level rise, occurred in CSE and CSD, respectively, while in the TCSA, the lowest and highest movements in the toe were predicted to occur in CSC and CSA, respectively. It is curious that CSA produced both the lowest SWI in the TLA and the highest SWI in the TCSA (i.e., caused by sea-level rise) of the cases described here. Further investigation is needed to identify the exact cause of this. Overall, the 0.3 m sea-level rise has a greater impact on the TCSA than on the TLA, leading to greater landward movements of the seawater toe in the TCSA than in the TLA across four of the five cross sections (CSA, CSB, CSD, and CSE) that were evaluated.

## References

Morgan, L.K., Harrington, N., Werner, A.D., Hutson, J.L., Woods, J., and Knowling, M.J., 2015. South East regional water balance project–Phase 2. Development of a regional groundwater flow model. Technical Report Series No. 15/38, 142 p. https://goyderinstitute.org/wp-content/uploads/2023/06/goyder_trs_15-38_south_east_regional_water_balance_phase_2.pdf (Accessed November 04, 2024).

# Appendix O – Prediction of long-term seawater intrusion caused by an 18% decline in recharge (Scenario 3c)

Figures O1 to O4 show the steady-state distribution of salinity for CSA, CSB, CSC and CSD (respectively) following a decline of 18% in the distributed recharge. Pumping rates were assumed to continue at 2013 levels, and therefore, the seawater intrusion (SWI) during this case was obtained by comparing the results given below to those of Scenario 3a. Scenario 3c is described in more detail in Section 2.5 of the main report. As discussed in the main report, in this case, the inland boundary head decreases relative to Scenario 3a because the recharge decline was applied to the regional model before extracting the stresses for the different cross sections in this scenario. Consequently, the effects of the recharge reduction occur in two different ways: a decrease in the inland head and a reduction in the recharge (i.e., 18% lower than the average recharge of 2004–2013) applied to the top layer of each cross section.

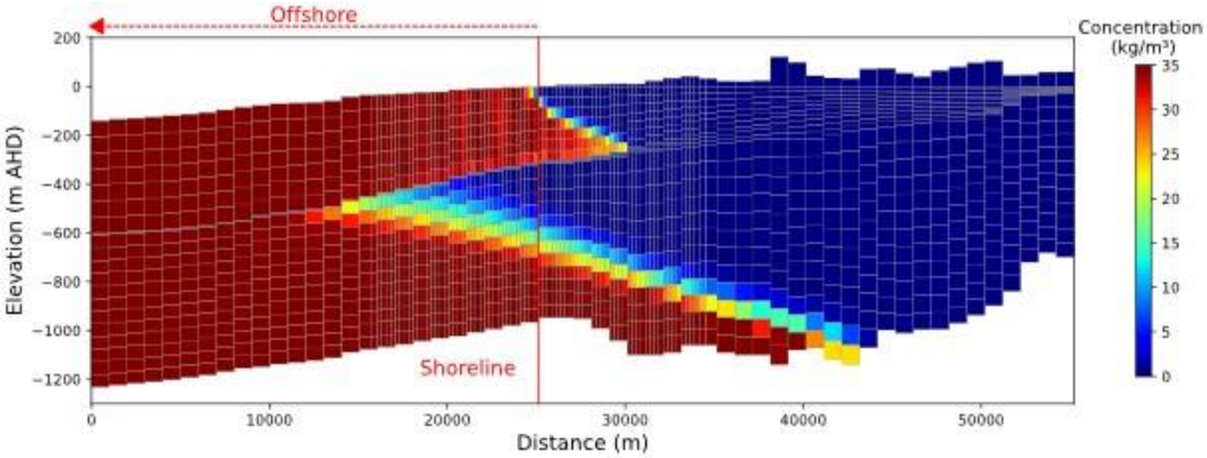

**Figure O1.** Steady-state distribution of salinity at CSA caused by a decline of 18% (relative to 2004–2013) in recharge.

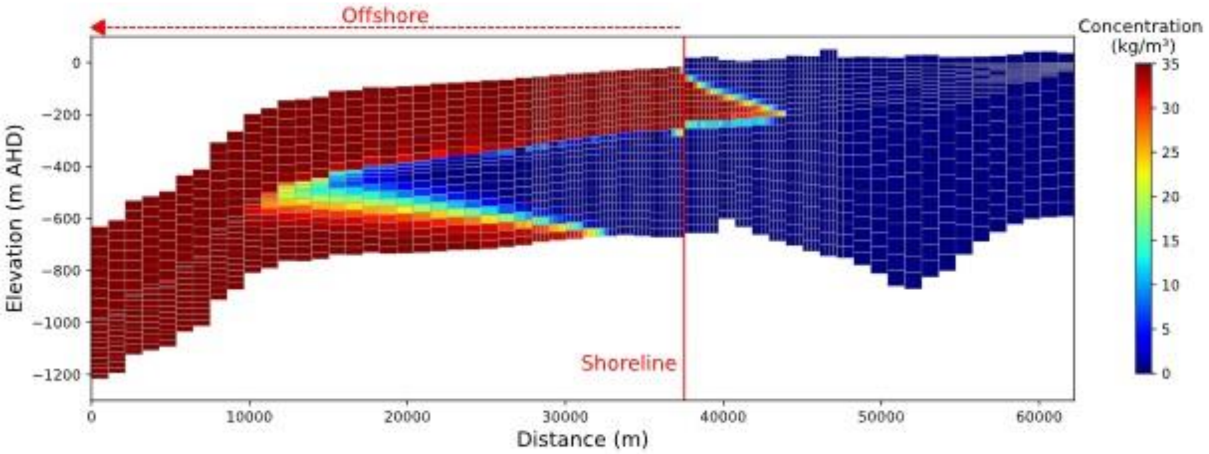

**Figure O2.** Steady-state distribution of salinity at CSB caused by a decline of 18% (relative to 2004–2013) in recharge.

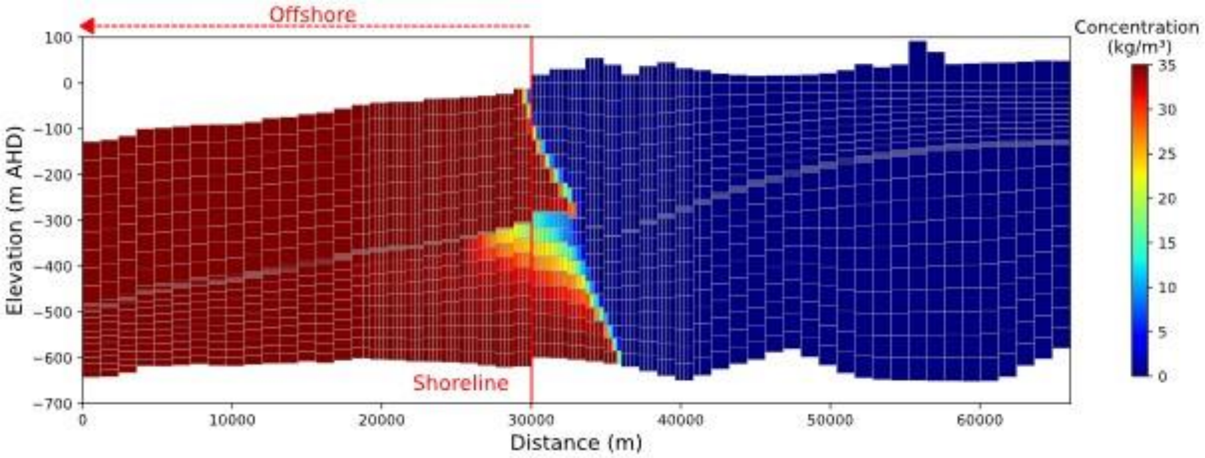

**Figure O3.** Steady-state distribution of salinity at CSC caused by a decline of 18% (relative to 2004–2013) in recharge.

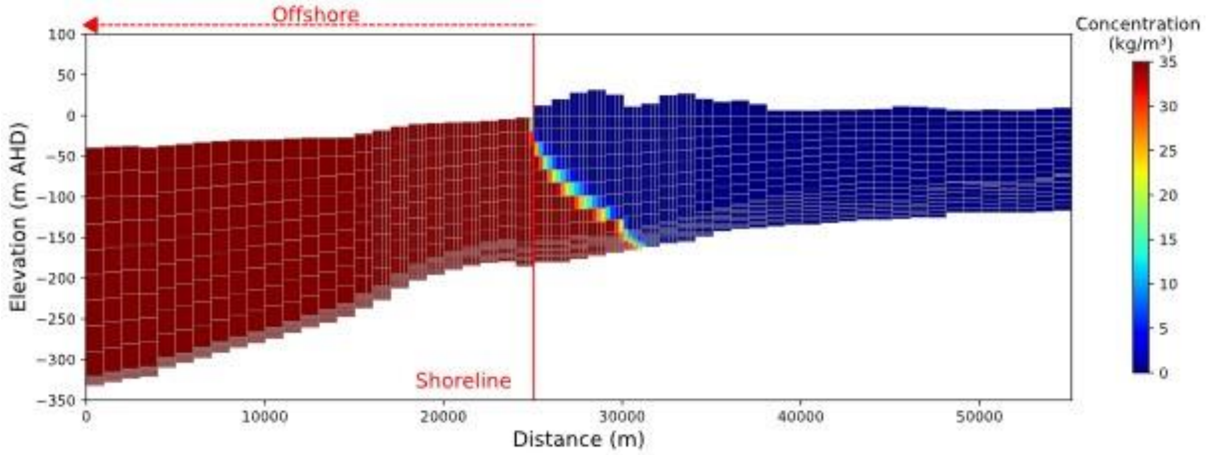

**Figure O4.** Steady-state distribution of salinity at CSD caused by a decline of 18% (relative to 2004–2013) in recharge.

In Figure O1, compared to Scenario 3a, the seawater toe shifted 752 m further inland in the TLA of CSA (due to lower recharge), reaching 4,959 m inland from the shoreline. In the TCSA, the toe moved 3,591 m further inland (caused by the recharge decline), reaching 17,841 m onshore. The drop in recharge caused a head fall of 0.50 m in the TLA at 5 km from the coast, and a decline of 1.27 m in the TCSA at 10 km inland. These drawdowns are considerably larger than the "relative drawdown" arising from sea-level rise (Appendix N), where the "relative drawdown" is the difference between the sea-level rise of 0.3 m and the head rise in the aquifer. Thus, the recharge decline of 18% appears to cause much greater SWI in both the TLA and TCSA relative to the 0.3-m sea-level rise, at least at CSA.

Figure O2 shows that, compared to the steady-state simulation of future conditions (Scenario 3a) at CSB, the seawater toe ends up 1,096 m further inland, reaching 6,338 m onshore in the TLA. The toe shifts 1,899 m landward in the TCSA due to the recharge decline, reaching 5,440 m offshore from the shoreline. These landward toe shifts resulted from head reductions of 0.46 m at 5 km inland in the TLA and 1.18 m at 10 km inland in the TCSA. In CSB, SWI resulting from an 18% decline in recharge is more severe in both the TLA and TCSA compared to the effects of sea-level rise in Scenario 3b.

Figure O3 illustrates that, at CSC, the recharge decline caused the seawater toe to shift 190 m further inland, reaching 2,992 m onshore in the TLA, and the toe in the TCSA advanced 371 m inland, extending to 5,844 m onshore. This was associated with head drops of 0.19 m and 0.79 m at 5 km and 10 km inland from the coast in the TLA and TCSA, respectively. Again, the recharge decline caused worse SWI than that resulting from sea-level rise.

In Figure O4, at CSD, the seawater toe moved 362 m further inland because of the 18% recharge decline, reaching 4,969 m onshore in the TLA, while the toe in the TCSA advanced 296 m further inland from the recharge reduction, extending to 5,998 m onshore. This is attributable to a decline in head of 0.09 m in the TLA at 5 km inland and a 0.11 m head drop in the TCSA at 10 km inland. In CSD, the predicted SWI caused by the 18% decline in recharge is less severe than that resulting from sea-level rise of 0.3 m (Scenario 3b) in both the TLA and TCSA.

The results show that a recharge reduction of the scale assessed here is likely to have the greatest impact in CSB in terms of SWI in the TLA, while the worst SWI in the TCSA occurred in CSA. Overall, the recharge reduction of 18% had a larger impact on the TCSA, leading to greater landward seawater toe movements (relative to those in the TLA) across most of the cross sections (CSA, CSB, CSC, and CSE) that were modelled in this study.

# Appendix P – Prediction of long-term seawater intrusion caused by a 71% increase in pumping (Scenario 3d)

Figures P1 to P4 show the steady-state salinity distributions for CSA, CSB, CSC and CSD, respectively, following a 71% increase in pumping (Scenario 3d). This scenario is described in more detail in Section 2.5 of the main report. As noted in the main report, the inland boundary head in this scenario is lower than in Scenario 3a, because the pumping increase was applied to the regional model before the stresses were extracted for the individual cross sections. As a result, the impact of the increased pumping is reflected in two ways: a reduction in the inland boundary head and an increase in pumping (where cross sections intercept pumping wells) within each cross section.

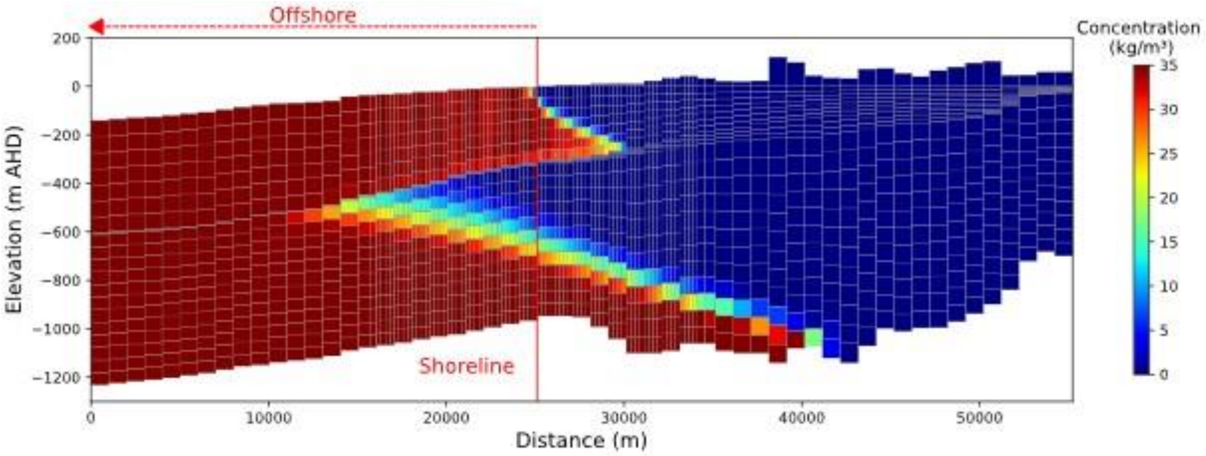

**Figure P1.** Steady-state distribution of salinity at CSA where the average pumping rate of 2013 was increased by 71%.

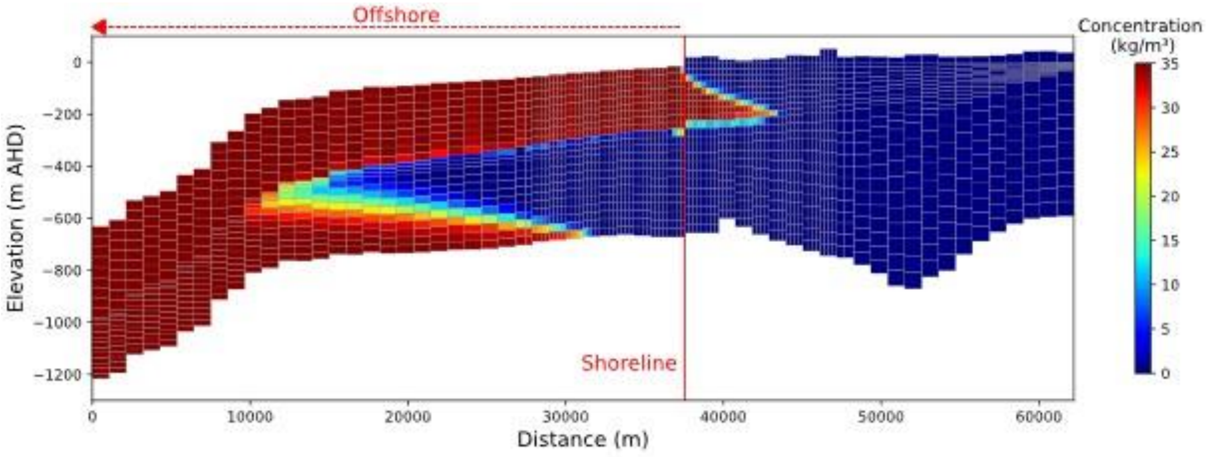

**Figure P2.** Steady-state distribution of salinity at CSB where the average pumping rate of 2013 was increased by 71%.

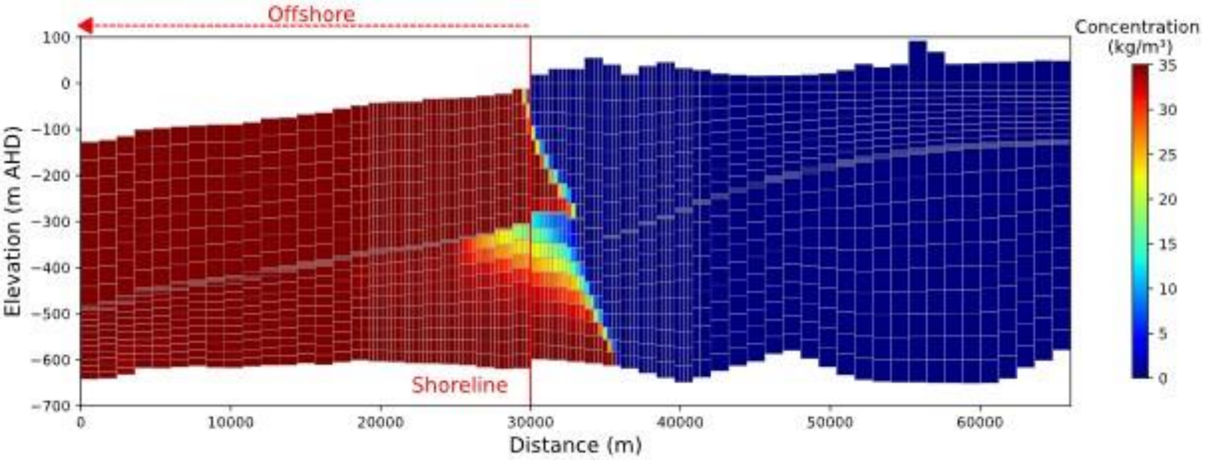

**Figure P3.** Steady-state distribution of salinity at CSC where the average pumping rate of 2013 was increased by 71%.

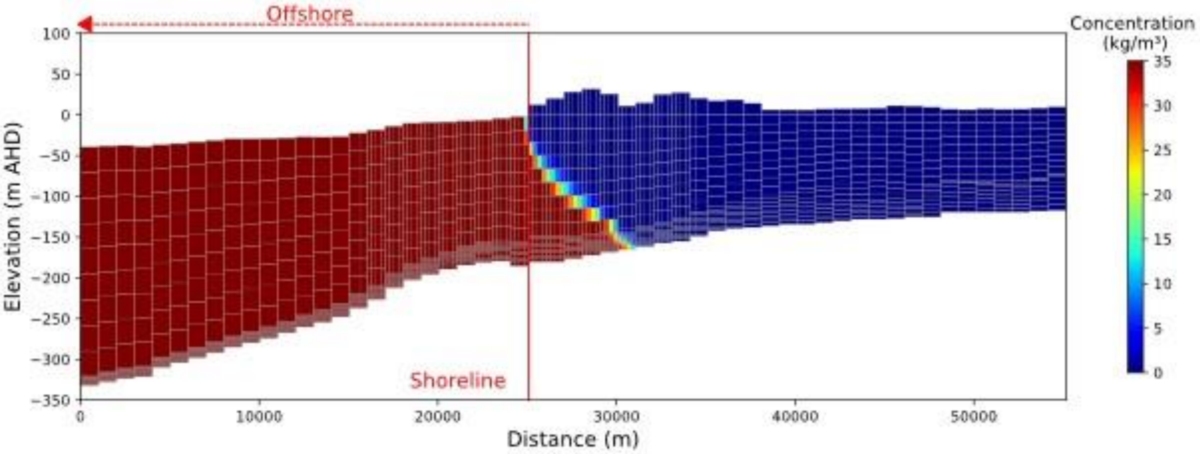

**Figure P4.** Steady-state distribution of salinity at CSD where the average pumping rate of 2013 was increased by 71%.

In Figure P1, compared to Scenario 3a (continuation of 2013 pumping rates), the seawater toe advanced 460 m further inland in the TLA (in CSA) due to the increased pumping (relative to 2013), reaching 4,667 m onshore, while the toe in the TCSA shifted 1,312 m further inland, reaching 15,562 m onshore in CSA. The modelled SWI was accompanied by a 0.29 m head decrease at 5 km inland in the TLA and a 0.57 m head decrease at 10 km inland in the TCSA. Seawater intrusion (SWI) in CSA caused by a 71% increase in pumping is predicted to be worse than that caused by a 0.3 m sea-level rise (in both the TLA and TCSA), but not as severe (in both the TLA and TCSA) as the SWI caused by the 18% decline in recharge.

Figure P2 shows the distribution of salinity at CSB following the 71% pumping increase. Compared to the steady-state simulation of future conditions (Scenario 3a) at CSB, the seawater toe was 472 m further inland, reaching 5,714 m onshore from the shoreline in the TLA, while the toe was 911 m landward, reaching 6,428 m offshore from the shoreline in the TCSA. Head drops of 0.24 m in the TLA (at 5 km inland) and 0.58 m in the TCSA (at 10 km inland) accompany the SWI in CSB. In CSB, the SWI caused by a 71% increase in pumping is more severe than in Scenario 3b (sea-level rise of 0.3 m) for both the TLA and TCSA, but less severe than in Scenario 3c (an 18% decline in recharge).

Figure P3 illustrates the salinity distribution at CSC following a 71% increase in pumping rates. Compared to Scenario 3a at CSC, the seawater toe was 74 m further inland, reaching 2,876 m onshore in the TLA, while the toe in the TCSA was 240 m further inland, extending to 5,713 m onshore. The higher pumping rate caused a head decline of 0.03 m at 5 km inland and 0.23 m at 10 km inland in the TLA and TCSA, respectively. In CSC, SWI due to a 71% increase in pumping is less severe than that observed in Scenario 3b (sea-level rise of 0.3 m) and Scenario 3c (an 18% decline in recharge) for the TLA. In the TCSA, Scenario 3d produced more extensive SWI than in Scenario 3b (sea-level rise), but was less severe than the SWI of Scenario 3c (recharge decline).

Figure P4 presents the salinity distribution at CSD due to a 71% increase in the pumping rate. Compared to Scenario 3a at CSD, the seawater toe shifted 122 m further inland, reaching 4,729 m onshore in the TLA, and advanced 133 m further inland in the TCSA, extending to 5,835 m onshore. Reductions in head from the increased pumping were 0.02 m at 5 km inland in the TLA and 0.04 m at 10 km inland in the TCSA. In CSD, SWI due to a 71% increase in pumping is less severe than that observed in Scenario 3b (sea-level rise of 0.3 m) and Scenario 3c (an 18% decline in recharge) for both the TLA and TCSA.

The Scenario 3d modelling results from the five cross sections reveal that in the TLA, the least SWI occurred in CSE, while the most SWI was predicted to occur in CSB. In the TCSA, CSE showed the least SWI, while CSA showed the most extensive SWI. Overall, the 71% increase in pumping rate affects the TCSA more than the TLA, causing greater landward shifts of the seawater toe across all five modelled cross sections.

Studies that compare the effects of sea-level rise and pumping on SWI have produced mixed results—showing that either stress may dominate depending on the specific conditions (e.g., Ferguson and Gleeson, 2012; Lu et al., 2013).

## References

Ferguson, G., and Gleeson, T., 2012. Vulnerability of coastal aquifers to groundwater use and climate change. Nature climate change, 2(5), 342-345. https://doi.org/10.1038/nclimate1413

Lu, C., Werner, A.D., and Simmons, C.T., 2013. Threats to coastal aquifers. Nature Climate Change, 3(7), 605-605. https://doi.org/10.1038/nclimate1901

# Appendix Q – Comparison of numerical model and airborne electromagnetic (AEM) results

The airborne electromagnetic (AEM) flight lines 300121 and 100011 align best with the axes of modelling cross sections CSA and CSB. The other cross sections do not have nearby AEM flight lines and were therefore omitted from the AEM-numerical model comparison that follows. Model salinity distributions, clipped to align with AEM outputs, are given in Figures Q1 and Q2 for CSA and CSB, respectively. These results are a zoom-in of salinity distributions obtained from Scenario 2 (Appendix J), as these modelling outcomes are considered to most likely reflect contemporary salinity distributions reflecting the current seawater extent in the Limestone Coast aquifers.

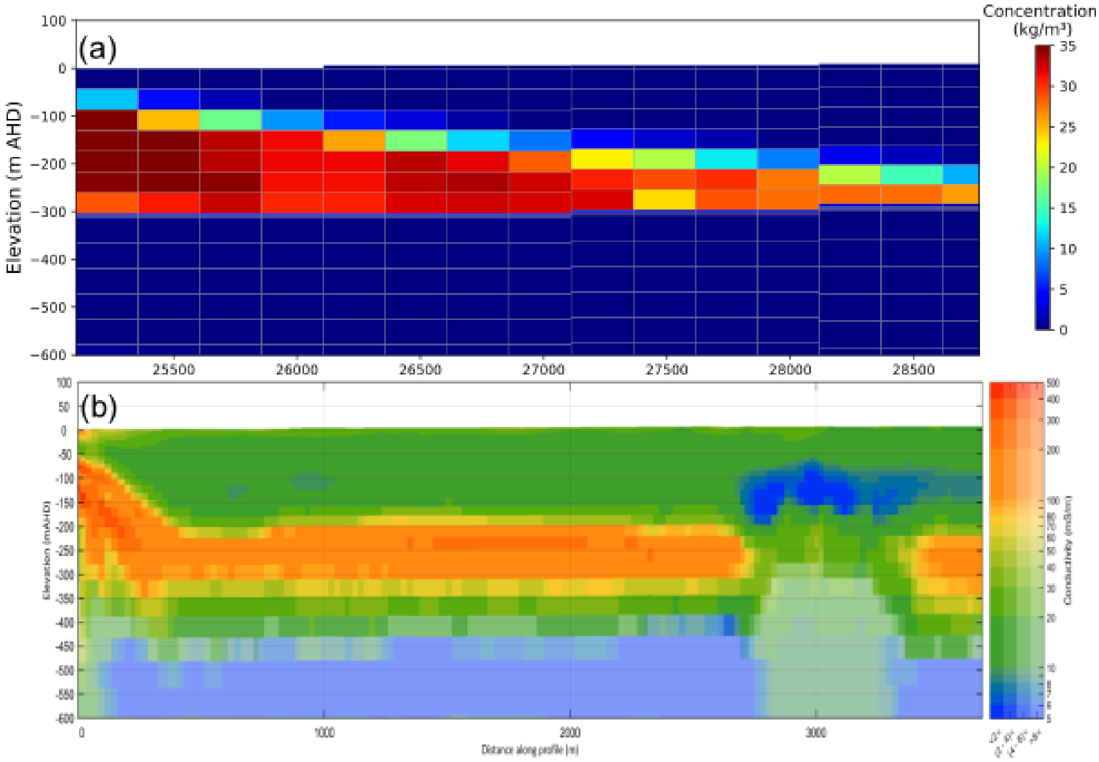

**Figure Q1.** Comparison of numerical model and AEM (flight line 300121) results for cross section CSA. (a) Numerical model results derived from the salinity distribution at the end of the transient simulation (Figure J1); (b) interpretation of AEM survey derived from Davis et al. (2025a, 2025b).

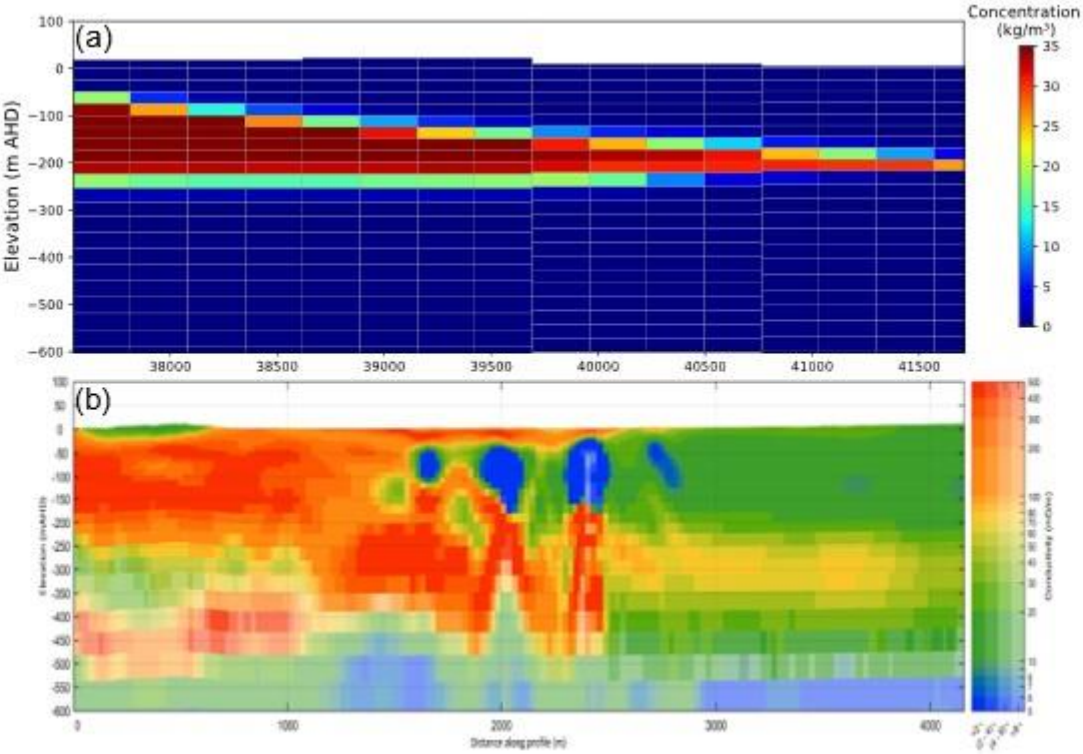

**Figure Q2.** Comparison of numerical model and AEM (flight line 100011) results for cross section CSB. (a) Numerical model results derived from the salinity distribution at the end of the transient simulation (Figure J2); (b) interpretation of AEM survey derived from Munday et al. (2025a, 2025b).

The results of Figure Q1 show a rather remarkable similarity between the model and the AEM interpretation, with the exception of the interruption to the higher-conductive region in the AEM results around $x$ = 3,000 m. There is a steeper saltwater wedge in the AEM results than observed in the model. This may arise from the relatively coarse model discretisation near the coast apparent in Figure Q1a. A finer discretisation may improve the match, but it is nevertheless encouraging to see this degree of similarity between the two independent techniques for assessing the seawater extent in the aquifer.

The match between the model and the AEM results at CSB is weaker, although the thin wedge of saltwater near the inland boundary (x > 3,000 m) occurs in both models. The AEM results have less reliability with depth, as indicated by the lighter shading of the colours within the lower aquifer. It is likely that only the salinities in the TLA are interpretable at CSA and CSB and salinities in the TCSA are not observable from the AEM survey at these sites.

## References

Davis, A., Munday, T.J., and Ibrahimi, T., 2025a. Adaptation of the South-Eastern drainage system under a changing climate - Limestone Coast Airborne Electromagnetic Survey: Acquisition, Processing and Modelling. Goyder Institute for Water Research Technical Report Series No. 25/5.1.

Davis, A., Munday, T.J., and Ibrahimi, T., 2025b. Adaptation of the South-Eastern drainage system under a changing climate - Limestone Coast Airborne Electromagnetic Survey: Conductivity-Depth Sections. Goyder Institute for Water Research Technical Report Series No. 25/5.2.

GOYDER INSTITUTE
FOR WATER RESEARCH

Government of South Australia
Department for Environment and Water

CSIRO

Flinders University

THE UNIVERSITY of ADELAIDE

University of South Australia

The Goyder Institute for Water Research is a research alliance between the South Australian Government through the Department for Environment and Water, CSIRO, Flinders University, the University of Adelaide and the University of South Australia.